SYNTHESIS AND CHARACTERIZATION OF SILVER NANOPARTICLES FOR PHOTOVOLTAIC APPLICATION

Razia Adam

A thesis submitted in fulfilment of the requirements for the degree of Magister Scientiae in the Department of Physics, University of the Western Cape

Supervisor: Dr. S. Botha, University of the Western Cape

Co-supervisor: Dr. T. Muller, University of the Western Cape

September 2013

To my Mother Mariam Adam, and late father, Noor-Mohammed Adam

ACKNOWLEDGEMENTS

To my Creator and Sustainer, all mighty Allah, for providing me with insight and understanding and without whom all of this would not have been possible.

I am grateful to the following people without whose assistance, advice and guidance the completion of this thesis would not be possible:

Dr. Subelia Botha of the Electron Microscopy Unit (EMU) at the University of the Western Cape (UWC), for her supervision, guidance, motivation, friendship and constant support throughout the course of my masters;

Dr. Theo Muller of the department of physics at UWC who acted as co-supervisor, and for assistance with thin films;

Prof. Christopher Arendse of the department of physics UWC, for constantly providing insight, motivation and guidance throughout this work;

Prof. Basil Julies, Dr. Francious Cummings and Mr. Adrian Josephs of the EMU at UWC for assistance with all microscopy related work;

Dr. Tesfayo Warrior of the department of chemistry of UWC for assistance with UV-VIS measurements;

Dr. Salaam Tintinchi of the department of chemistry of UWC, for allowing me to make use of the equipment in his laboratory;

Dr. Remmy Bucher, of the MRD at iThemba labs for assistance with XRD measurements;

My mother Mariam Adam for the continued support and encouragement throughout my studies;

My loving husband, Abdulghaaliq Adams for consistently motivating, supporting, and providing useful insight;

To my sister, Rashida Adam for her consistent support, love, motivation, and guidance throughout my studies;

My brother, Faizel and his wife Jihaan Adam, for their support;

My mother and father in law, Faiza and Nasief Adams for their continued support;

To Mrs. Angela Adams of the physics department of UWC for always assisting administratively, motivation, support and friendship;

To Mrs. Natasha Kenseley of the EMU of UWC for her motivation, friendship and administrative assistance;

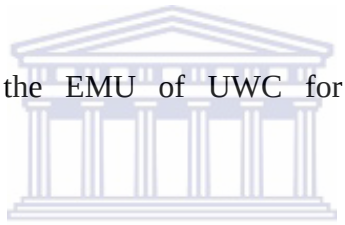

My colleagues, friends and fellow MANUS/MATSCI colleagues at UWC, Nazley Towfie, Natasha Venita Petersen, Valentino van de Heyde, Sulaiman Jacobs, Keegan Pokpas, and Oriel Bayman for their friendship and support;

To my friends Diego Mushfieldt, Taryn Mac Mahon, Robin De Vos, Faika Solomon and Tauriq Samie for their continued support and motivation.

The staff of the physics department of UWC for their hospitality.

DECLARATION

I declare that

"SYNTHESIS AND CHARACTERIZATION OF SILVER NANOPARTICLES FOR PHOTOVOLTAIC APPLICATION"

Is my own work and that all sources used or quoted have been indicated and acknowledged by means of complete references.

Razia Adam September 2013

KEY WORDS

SYNTHESIS AND CHARACTERIZATION OF SILVER NANOPARTICLES FOR PHOTOVOLTAIC APPLICATION

Razia Adam

Silver nanoparticles

Polyol synthesis

Plasmonic solar cells

Thin films

Ethanol

Ethylene Glycol

Optical properties

ABSTRACT

"SYNTHESIS AND CHARACTERIZATION OF SILVER NANOPARTICLES FOR PHOTOVOLTAIC APPLICATION"

Razia Adam

M. Sc thesis, Department of Physics, University of the Western Cape

With an increase in the amount of harmful carbon emissions in the atmosphere as well as a decrease in the availability of fossil fuels, there is a relatively high demand for alternate energy devices. Solar cells have become an alternative option in aid of leading the way for clean energy; however these devices are relatively expensive and have an efficiency that is relatively low in comparison to that of fossil fuelled energy. As a result the cost of the solar cell needs to be reduced by reducing the amount of silicon used in order to compete with fossil fuelled devices; however this decrease would lead to a decrease in efficiency.

In recent years silver nanoparticles have been extensively researched as a result of its extraordinary optical, electrical, catalytic, magnetic and antibacterial properties. As a result of these properties, the nanoparticles may be applied to many research areas such as photovoltaics, catalysis and medical fields. The optical properties of silver nanoparticles may thus be exploited in order to increase absorption and in turn the efficiency of the solar cell devices.

This study focuses on the optimization of the polyol synthesis to possibly obtain uniformly dispersed silver nanoparticles. The silver nanoparticles would then be incorporated onto amorphous silicon thin films, deposited by hot wire chemical vapour deposition, by spraying a suspension of the silver nanoparticles onto the thin films. The silver nanoparticles were

characterized by Ultra Violet Visible Spectroscopy (UV-VIS), High Resolution Transmission Electron Microscopy, X-ray Diffraction, and Thermogravimetric Analysis. The thin films with the incorporated silver nanoparticles were characterized by UV-VIS, and High Resolution Scanning Electron Microscopy. It was shown that silver nanoparticles with various morphologies were produced by the polyol synthesis and may be used to enhance light trapping of thin film photovoltaic devices.

Table of Contents

List of Tables

List of Figures

List of Abbreviations

PVP : Polyvinylpyrrolidone

UV-VIS : Ultra Violet Visible Spectroscopy

HRTEM : High Resolution Transmission Electron Microscopy

EDS : Energy Dispersive Spectroscopy

STEM : Scanning Transmission Electron Microscopy

HRSEM : High Resolution Scanning Electron Microscopy

XRD : X-ray Diffraction

SAED : Selected Area Electron Diffraction

FT-IR : Fourier Transform Infrared Radiation

TGA : Thermogravimetric Analysis

ARC : Anti-reflective coating

LSP : Localized Surface Plasmons

SPP : Surface Plasmon Polaritons

HWCVD : Hot Wire Chemical Vapour Deposition

EM : Electromagnetic

FWHM : Full Width Half Maximum

Ag-NP : Silver Nanoparticles

a-Si:H : Amorphous Silicon

CHAPTER 1

Introduction

Silicon solar cells have received considerable attention in recent years, since they rely on the most abundant source of energy in nature for the generation of electricity. Although they use the sun, the efficiency is relatively poor in comparison to that of fossil fuelled devices. Thus the need to increase the efficiency of the solar cell is of outmost importance such that it can slowly phase out the use of fossil fuelled devices. The cost of these alternate devices are also relatively expensive, thus methods that would decrease the amount of silicon used as well as increase the efficiency need to be applied to allow these devices to compete with fossil fuelled energy devices. Decreasing the amount of silicon used result in an overall decrease in the efficiency of the device. Thin films utilise less silicon, thus causing them to have decreased efficiencies. However, other techniques may be employed to enhance the absorption of the thin film and in turn the efficiency [1.1].

As a result of the outstanding optical properties exhibited by silver nanoparticles, they may offer a solution to enhancing efficiencies of thin film silicon solar cells [1.2]. The performance of the silver on a bulk scale differs substantially from the nano scale since the properties of silver is dramatically enhanced when utilized on the nano scale [1.3]. Thus, by incorporating silver nanoparticles into thin film structure would possibly increase the efficiency of the film.

There are a series of techniques that may be employed for the synthesis of the particles, such as photochemical, microwave irradiation, electrochemical methods, atomic beam sputtering

and chemical reduction [1.4]. However these methods require relatively complex and costly equipment. The method for the synthesis of the particles used for this project is the polyol method (chemical reduction method), and was chosen as a result of its simplicity and use of basic equipment [1.5].

For optimal performance of the silver nanoparticles, the nanoparticles are required to have a uniform size distribution as well as a uniform shape. Therefore, it is of essence to find the most suitable reaction parameters that would yield nanoparticles of even size distribution and shape for optimum performance in their application.

1.1 Thesis Outline

Chapter 1 provides an introduction to the study, as well as a motivation for the present study.

Chapter 2 provides an overview of the various synthesis techniques for obtaining silver metal nanoparticles, the growth mechanisms, and stabilization processes. This chapter also provides a literature review of the properties of silver as well as an overview of the application of the nanoparticles i.e. solar cells. A conclusion of the literature overview is provided at the end of the chapter, as well as the aims and objectives of the research.

Chapter 3 provides description of the methods and material used in the course of the study, as well as an overview of the characterization techniques employed to analyse the thin films and silver nanostructures. The characterization techniques include Ultra-Violet Visible Spectroscopy, High Resolution Electron Microscopy, High Resolution Scanning Electron Microscopy, X-Ray Diffraction, and Thermogravimetric Analysis. Chapter 4 discusses the results obtained from the synthesis of the silver nanoparticles, and Chapter 5 discusses the results of the thin films produced. Chapter 6 provides a summary of the results obtained and future work.

1.2 References

[1.1] Catchpole, KR and Polman. A, *Appl. Phys. Let.*,**93**, p 191113 (2012)

[1.2] Atwater, H and Polman. A, *Nat. Mater*., **9**, p 205 (2010).

[1.3] Evanoff. D, and Chumanov. G, *ChemPhysChem*, **6**, p 1221 (2005)

[1.4] Zhao. T, Sun. R, Yu. S, Zhang. Z, Zhou. L, Huang. H, and Du. R, *Colloids Surf., A*, **366**, p 197 (2010).

[1.5] Jiang. H, Moon. K, Zhang. Z, Pothukuchi. S, and Wong. CP, *J. Nanopart. Res.*, **8**, p 117 (2006)

CHAPTER 2

Literature Overview

2.1 Solar Cells – An Introduction

In recent years, there have been increased concerns about the environmental issues as a result of increased use of fossil fuels, due to an increased demand of energy. Thus it is incumbent on researchers to find an alternative energy solution that will decrease the consumption of fossil fuels and in turn reduce the harmful effects that they contribute to the environment. Such an energy solution comes in the form of a solar cell [2.1].

Solar cells make direct use of sunlight to generate energy. This is relatively useful since the sun is the most abundant form of energy and is readily available [2.1].The amount of energy consumed by the world's population in one year is less than the energy produced by the sun in one hour [2.1].The energy provided by the sun comes in the form of electromagnetic radiation, composed of a large range of wavelengths.

2.1.1 Basic Operation

The most basic solar cell consists of a semiconducting material such as silicon and gallium. These are materials that have a small band gap with a discrete energy between the valence and conduction bands [2.2, 2.3]. Metals cannot be used for this device since their conduction and valence bands overlap, thus resulting in the continuous transferral of electrons to and from the valence and conduction bands. Insulators are materials that have one completely filled band and one empty band. These materials also have relatively large band gaps, such

that they require a significant amount of energy to excite electrons from the valence, to the conduction band [2.3].

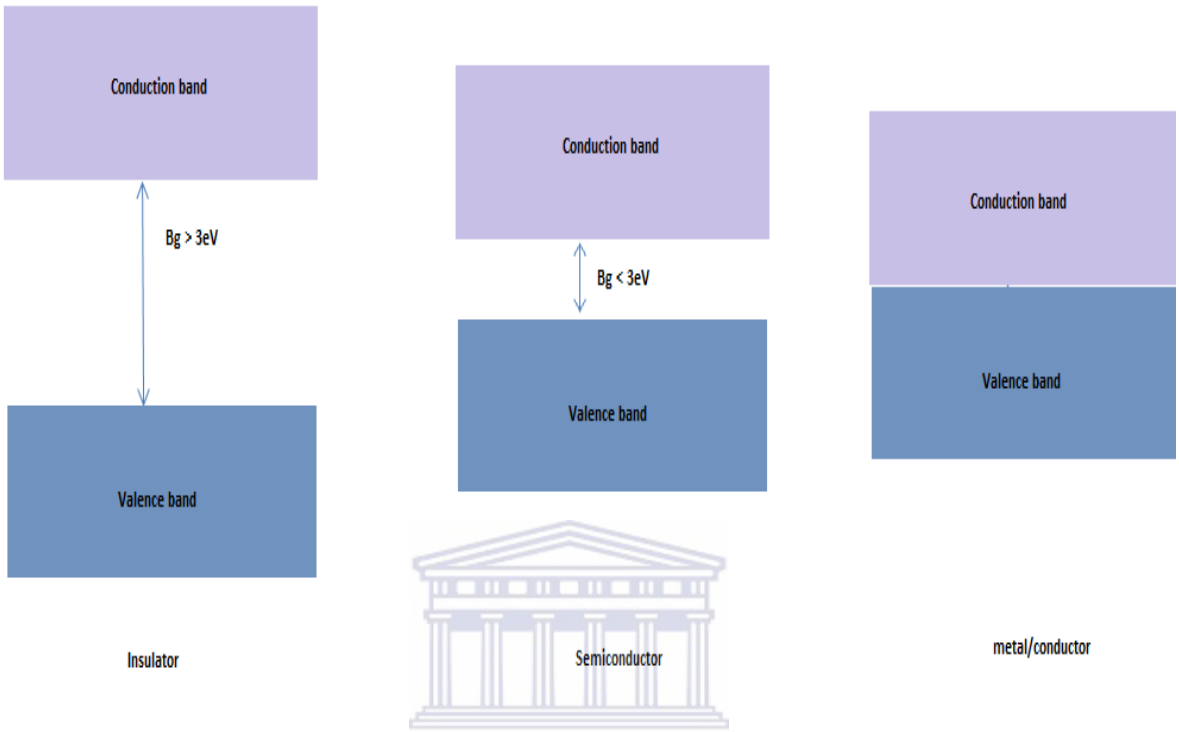

Figure 2.1: Schematic diagram of the difference between insulators, semiconductors and metals.

Figure 2.1 shows the distinct difference in the band gap between insulators, semiconductors and metals. Insulators have band gaps larger than 3 eV; semiconductors have band gaps less than 3 eV and therefore only require a minimal amount of energy to excite electrons from the valence to the conduction band. Metals do not have band gaps, thus the electrons flow freely between the bands [2.3, 2.4, 2.5].

The conduction band is the highest occupied energy state whereas the valence band corresponds to the lowest unoccupied state. Incident photons from the sun excite electrons from the valence band to the conduction band, given that the energy of the photon exceeds that of the band gap of the semiconducting material. This creates an electron-hole pair, (hole in the valence band, electron in the conduction band) that may move freely, thus generating electricity as a result of moving charges [2.4, 2.5].

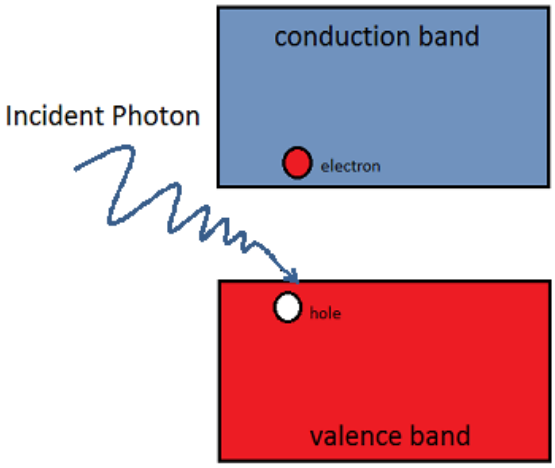

Figure 2.2: Schematic diagram of the generation of electron-hole pairs from incident photons.

Figure 2.2 shows the mechanism, by which an incident photon of sufficient energy excites electrons from the valence to the conduction band, which is used to create the flow of charge.

The electron-hole pairs may recombine after a relatively short period. It is of utmost importance that this process is prevented, such that an electrical current may be continually produced. This is obtained by creating an electrical current that will keep the electron-hole pair separated, resulting in a potential difference between them [2.3, 2.5].

2.1.2 p-n Junctions

p-n Junctions are relatively important in solar cell technologies since they provide extra electrons and holes to the semiconductor, which in turn provides extra energy levels in the band gap. These p-n junctions are generated by introducing n-type and p-type impurities into the semiconducting material [2.5].

An n-type impurity is an atom that contains an excess of electrons, thus donating electrons to the semiconductor, whilst a p-type impurity is an atom consisting of a deficiency of electrons, thus creating a hole to the semiconductor. These impurities are introduced into the semiconducting crystal lattice [2.5].

In the silicon semiconductor, the n-type impurity may come in the form of a pentavalent phosphorous (P) atom, and a p-type impurity as a trivalent boron (B) atom (figure 2.3) [2.1].

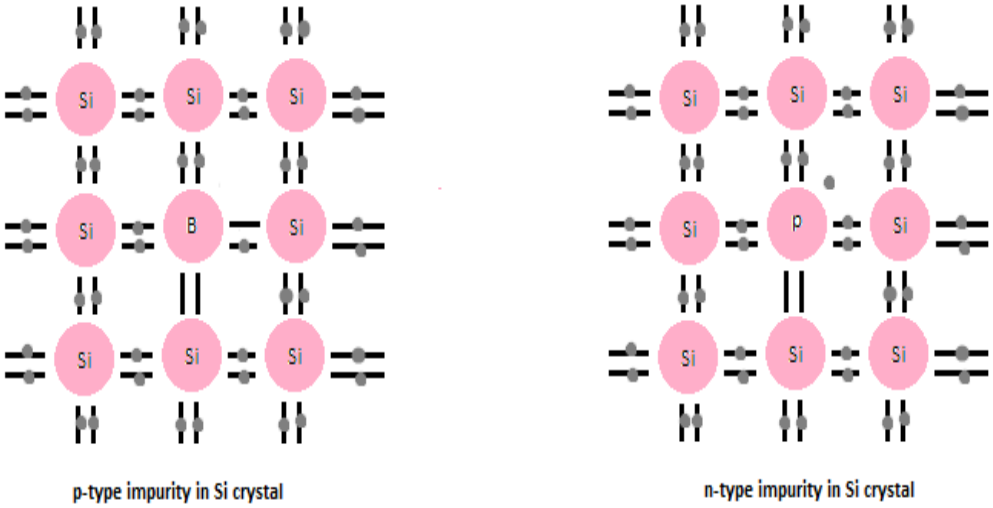

Figure 2.3: Schematic diagram of n-type and p-type impurities present in Si crystal.

When the n and p regions are brought into contact, a p-n junction is formed, resulting in an electric field between the two regions. Electrons from the n-region travel towards the p-region, which would result in a positive layer. Similarly the holes from the p-region move across towards the n-region leaving behind a negative layer. The positive and negative layers result in a depletion region (figure. 2.4) [2.5, 2.6].

The electric field created by the two regions, thus sweeps away all incoming electrons, resulting in an electric current across the devices [2.6].

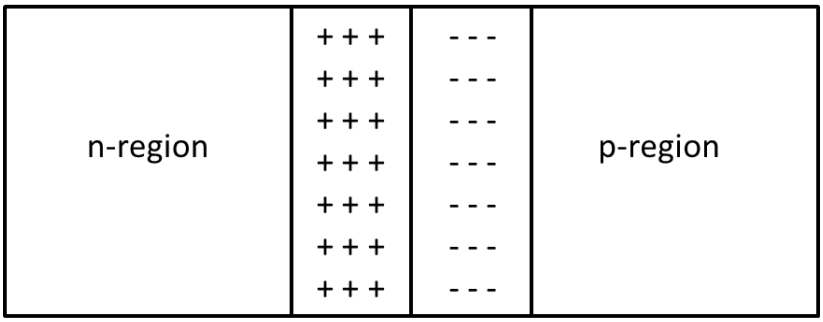

Figure 2.4: Schematic diagram of the p-n junction.

2.1.3 Loss mechanism in solar cells

During the process of absorption not all the photons incident on the solar cell is utilised. This is due to various processes such as thermalization losses, band gap limitations and recombination occurring within the solar cell which lead to optical losses [2.5].

2.1.3.1 Thermalization losses

This process occurs when the incident photons contains energies $E_{photon} > E_{g.}$ The electrons from the valence band are then excited towards the conduction band and all the excess energy of the photon is then dissipated as heat into the solar cell [2.5].

2.1.3.2 Band gap limitation

Photons which contain energies $E_{photon} < E_g$ are not able to excite electrons from the valence band to the conduction band due to insufficient energy of the photon. The energy of the photons are then imparted to other electrons in the material or simply transmitted through the solar cell [2.5].

2.1.3.3 Recombination

This is the process whereby electrons in the conduction band recombine with holes in the valence band, after the excitation process. Recombination processes vary according to the region of the cell in which it occurs [2.1].

2.1.3.3.1 Radiative Recombination

The process involves the recombination of an electron and hole in the conduction band, resulting in the emission of a photon with an energy equivalent to that of the band gap of the material [2.1].

2.1.3.3.2 Shockley-Read Hall Recombination's

A series of electron hole recombination processes occur within intermediate energy levels, which are either introduced deliberately or formed unintentionally. Energy levels are then found in the forbidden band gap, allowing electrons to be stored in the energy level, until it recombines with holes in the valence band [2.4].

2.1.3.3.3 Auger Recombination

This recombination process is a two-step, three particle interaction, whereby the excess energy from the recombination of an electron-hole pair is transferred to another electron or hole in the semiconducting material [2.1, 2.4].

2.1.4 Light Trapping Techniques in Solar Cells

Although silicon is a relatively good semiconducting material attributed to a band gap E_g = 1.12eV, the absorption is relatively poor. Thus, light trapping techniques are required to be incorporated such that more of the incident radiation is absorbed by the silicon. An overall enhancement in thickness of the semiconducting material could significantly increase the absorption, however this process may be relatively costly and other techniques are employed to produce an overall increase in absorption [2.4].

These techniques involve the process of increasing the path length of the solar cells active layer. This technique is relatively advantages since it decreases the overall use of semiconducting material whilst simultaneously reducing the minority/majority carrier recombinations [2.4].

Decreasing the reflectivity of the semiconducting material will result in a significant increase in the absorption. This can be achieved by allowing the incident radiation to be deflected such that it comes into contact with the semiconducting device more than once [2.5].

For a photon in a medium with refractive index n_1, incident on a material (substrate) with a refractive index n_2, the reflection coefficient R is given by:

$$R = \left|\frac{n_1 - n_2}{n_1 + n_2}\right|^2 \tag{2.1}$$

The reflection coefficient describes the intensity of the reflected wave incident on a material [2.7]. The various kinds of light trapping techniques utilized in solar cells are presented in the section to follow.

2.1.4.1Texturing

A decreased reflectivity can be achieved by etching the surface of the semiconducting material with pyramidal shaped features [2.4].

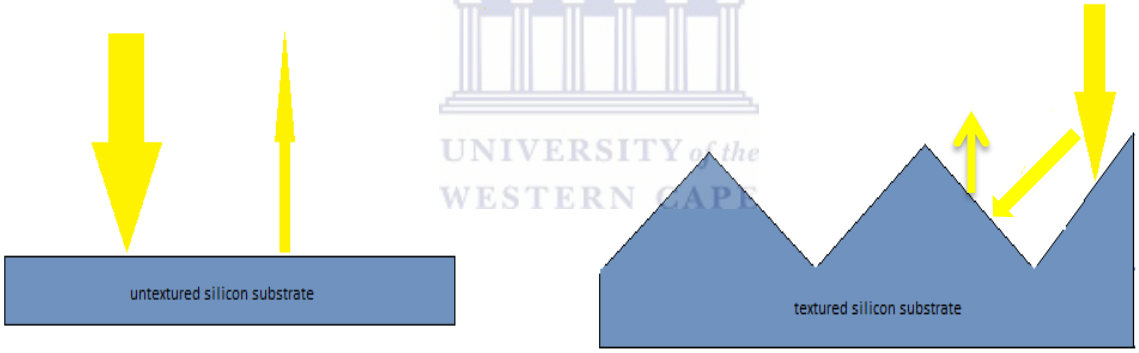

Figure 2.5: Schematic diagram showing how texturing enhances the absorption.

From the figure above (figure 2.5) it is evident that texturing the surface of the cell allows the incident light to be re-reflected numerous amounts of time, which contribute significantly to an enhancement in the overall performance of the device. It also indicates the relatively large amounts of semiconducting material that needs to be textured, in order to re-reflect the light.

Although texturing enhances the absorption by decreasing the overall reflectivity, it utilizes an average thickness of approximately 10μm of the semiconducting material, which is greater than the thickness of thin-film technologies [2.9].

2.1.4.2 Anti-reflective coatings

Another method of reducing the reflectivity is by introducing an anti-reflective coating to the semiconducting material. The anti-reflective coating (ARC) is a relatively thin film with a selected refractive index at the surface of the active-layer of the semiconducting material such that none of the incident radiation is reflected i.e. no reflection at the surface [2.4].

The most suitable refractive index for the anti-reflective layer should be$\sqrt{n_2}$. There are a series of materials used for anti-reflective coatings; these materials usually come in the form of oxides and nitrides. The materials used most widely is that of Si_3N_4 , due to its passivation effects on the surface of the substrate [2.10].

The thickness of the anti-reflective coating layer is given by:

$$n_1 d_1 = \frac{\lambda_0}{4}, \tag{2.2}$$

where n_1 is the refractive index of the ARC, $d_1$the thickness of the ARC film, and λ_0 the wavelength of the incident light. The optimal thickness of the ARC is one that would allow the reflected waves of the surface of the ARC to interfere destructively with the waves of the light that are reflected from the top of the surface of the semiconducting material [2.9].

2.1.4.3 Rear Reflectors

To ensure efficient light trapping, the optical path length needs to be enhanced; this is achieved by employing rear reflectors [2.8].

The rear reflectors usually occur in the form of aluminium or gold metal reflectors to allow the incident radiation to be reflected off the metal back reflectors to allow it to pass through the cell multiple times [2.8].

ARC and rear reflectors may be incorporated as light trapping techniques in thin films since the thickness of these films are suitable for these techniques. Texturing however, may not be incorporated as it utilizes and average thickness of approximately 2-3 μm of the film, which is the entire thickness of the thin film. Thus, other techniques should be incorporated to enhance the path length of the thin film, and in turn the overall efficiency of the thin film.

2.1.5 Efficiency of a solar cell

The net current density of a solar cell is given by:

$$J = J_s - J_{dark} = J_{sc} - J_0(e^{\frac{qV}{k_B}} - 1)\,, \tag{2.3}$$

where J_s is the short circuit current, k_B the Boltzmann constant, T the temperature in Kelvin, V the applied voltage and q, the charge of the electron. J_{dark} is given by the current flowing under no illumination [2.4, 2.5].

For an ideal diode the open circuit voltage V_0, is described by:

$$V_0 = \frac{kT}{q}\ln\left(\frac{J_{sc}}{J_0} + 1\right) \tag{2.4}$$

This relationship shows that the V_0 increases logarithmically with light intensity.For voltage ranges between 0 and V_{0C}, power is generated. At $V < 0$, power is consumed by the cell such that a photocurrent is generated [2.5, 2.6].Solar cells operate in the voltages ranging from 0-V_{0C}, in which power is delivered by the cell:

$$P = JV\,, \tag{2.5}$$

The maximum power generated by the cell occurs at a maximum voltage V_M with a corresponding current density J_M. The maximum resistance experienced by the cell is then given by [2.4, 2.5]:

$$R_M = \frac{V_M}{J_M} \tag{2.6}$$

The fill factor (FF) is described as the ratio of the maximum power obtained by the cell, to the product of the open circuit voltage V_{0C} and the short circuit current density J_{SC} [2.5].

$$FF = \frac{P_M}{J_{SC}V_{0C}} = \frac{J_M V_M}{J_{SC}V_{0C}} \tag{2.7}$$

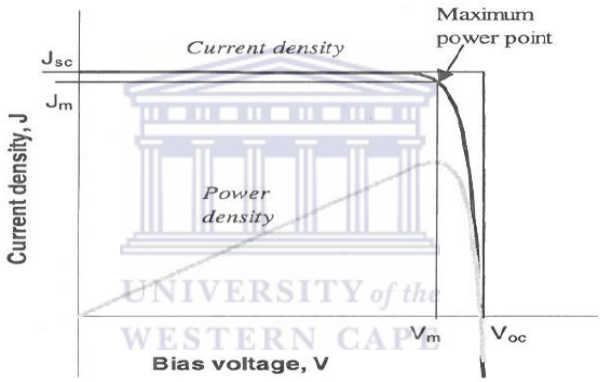

Figure 2.6: Current voltage and power- voltage characteristics of an ideal cell. At $\boldsymbol{V_M}$ the power density is at a maximum. The area of the inner rectangle gives the maximum power density, and the area of the outer rectangle is given by JscxVoc [2.5].

The FF is also an indication of how "square" the curve (figure 2.6) is. The efficiency η of the cell is described as the ratio of the maximum power delivered by the cell to the power input from the sun, denoted by P_S [2.5].

$$\eta = \frac{P_M}{P_S} = \frac{J_M V_M}{P_S} \tag{2.8}$$

Thus the efficiency of the cell is related to the fill factor by [2.33, 2.34]:

$$\eta = \frac{J_{SC}V_{0C}FF}{P_S} \tag{2.9}$$

The measurement of the efficiency of a solar cell is a vital aspect, for the determination of device quality. However, these measurements and construction of a complete solar cell is beyond the scope of this thesis.

Thin films consist of a relatively thin layer of semiconducting material, in the range of a few microns. Thus, surface texturing may not be employed as a light trapping technique, resulting in significant decrease in the absorption of light in the semiconducting material. Noble metal nanoparticles exhibit extraordinary optical properties that may be incorporated into a solar cell, such that the efficiency of the cell is enhanced [2.6].

2.2 Optical Properties of metal nanoparticles.

The optical properties of metal nanoparticles vary greatly from the bulk metal material as a result of the interaction between light and the conduction electrons of the nanostructure. This phenomenon has been observed for centuries dating back to the fourth century AD in which the Roman Lycurgus cup was discovered [2.11].

Figure 2.7: The Roman Lycurgus cup in reflected and transmitted light [2.12].

Figure 2.7 shows the Roman Lycurgus cup, the first evidence of the unique properties of noble metal nanoparticles. In reflected light the cup appears green, however in transmitted light the colour of the cup differs significantly [2.12].

The British museum has reported that the glass contains 0.5% manganese, whilst additional trace elements of silver, gold and other metals contribute 1%. Further analysis of the cup showed that it contained silver and gold nanoparticles in the range of 15-100 nm with a ratio of 7:3 (silver: gold) [2.12].

The properties may be attributed to the plasmon resonance of the noble metal nanoparticles. Plasmon resonance may be described as the collective oscillations of the conduction electrons of the noble metal. This mainly occurs in metals such as Au, Ag and Cu due to the presence of free conduction electrons [2.13]. When electromagnetic radiation is incident on the metal nanoparticles, the process whereby the conduction electrons oscillate is known as surface plasmons [2.13].

2.2.1 Surface Plasmons

When the particles are exposed to electromagnetic radiation, the conduction electrons are moved from their equilibrium positions, such that they are polarized. This results in a restoring force that causes the free electrons to oscillate at a characteristic frequency known as the Surface Plasmon Polariton frequency [2.13].

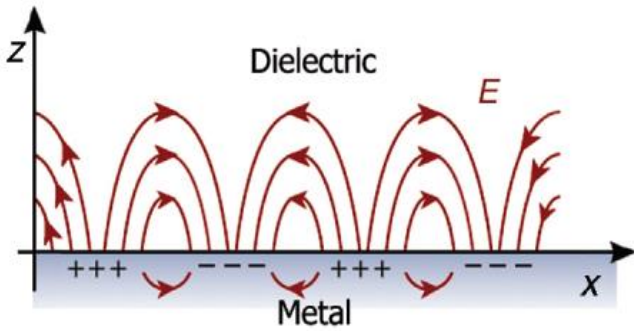

Figure 2.8: Schematic diagram of the interaction of an electromagnetic wave with a surface. (Surface Plasmon) [2.14].

When the surface of the material is exposed to incident electromagnetic radiation (figure 2.8), a polarizing effect is observed at the surface of the material. This highlights the process whereby surface plasmons interact.

When the conduction electrons of a confined volume is excited by an electric field (figure 2.9), it is known as Localised Surface Plasmons. The conduction electrons of a spherical particle oscillate coherently as the incident electromagnetic radiation excites them [2.14].

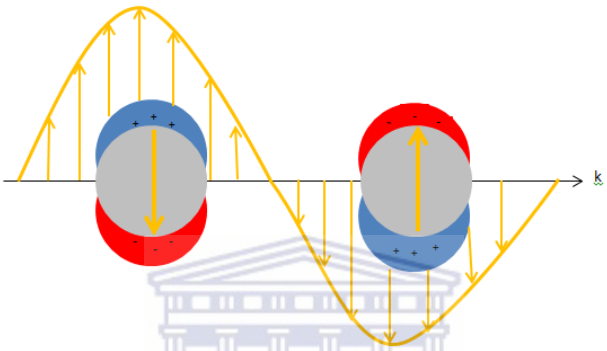

Figure 2.9: Schematic diagram of the interaction between electromagnetic radiation and spherical metal nanoparticles. The incident electromagnetic wave excites the conduction electrons such that they are displaced from their equilibrium position, creating a polarized particle.

The optical property of the particles is highly dependent on the frequency at which the particle resonates which in turn depends on the size, shape and dielectric medium of the particles (figure 2.10) [2.14].

Figure 2.10: Solutions of metal nanoparticles with various shapes and sizes [2.15].

The colour observed when the solutions are illuminated by white light is largely dependent on the plasmon resonance of the nanoparticles present in solution [2.14].

2.2.2 Light scattering by metal nanoparticles

At wavelengths near the plasmon resonance, metal nanoparticles scatter light relatively intensely. When the particles have diameters that are large fractions smaller than the wavelength of incident light, the absorption and scattering of the particle may be described by a point dipole [2.25].The absorption and scattering cross sections are given by [2.16, 2.17]:

$$C_{abs} = \frac{2\pi}{\lambda} Im[\alpha] , \tag{2.10}$$

and

$$C_{scat} = \frac{1}{6\pi}\left(\frac{2\pi}{\lambda}\right)^4 |\alpha|^2 , \tag{2.11}$$

α is the polarizability and is given by [2.16, 2.17]:

$$\alpha = 3V \left[\frac{\left(\frac{\varepsilon_p}{\varepsilon_m} - 1\right)}{\left(\frac{\varepsilon_p}{\varepsilon_m} + 2\right)}\right] \tag{2.12}$$

V is the volume of the particle, ε_p is the dielectric function of the particle and ε_m the dielectric function of the medium in which the particles are embedded [2.17].

The surface plasmon resonance will occur when $\varepsilon_p = -2\varepsilon_m$, at this point the polarazibility will increase significantly and the scattering cross section of the particle is much greater than the geometrical cross section [2.16, 2.17]. For smaller particles with diameters less than 50nm, absorption dominates. However, for particles with sizes of around 100nm, scattering dominates. For particles greater than 100nm the scattering efficiency will decrease [2.17].

The scattering efficiency Q_{scat} is given by [2.17]:

$$Q_{scat} = \frac{C_{scat}}{(C_{scat}+C_{abs})} \tag{2.13}$$

From equations 2.15 and 2.16 it is evident that the performance of the nanoparticles is dictated by the scattering and absorption, which in turn is greatly affected by the dielectric medium of the particle, the size and shape of the nanoparticles, since these parameters affect the volume, V. For light trapping it is of great importance that the metal nanoparticles have larger scattering cross sections rather than absorption scattering cross sections, such that the incident radiation can be scattered into the semiconductor [2.17].

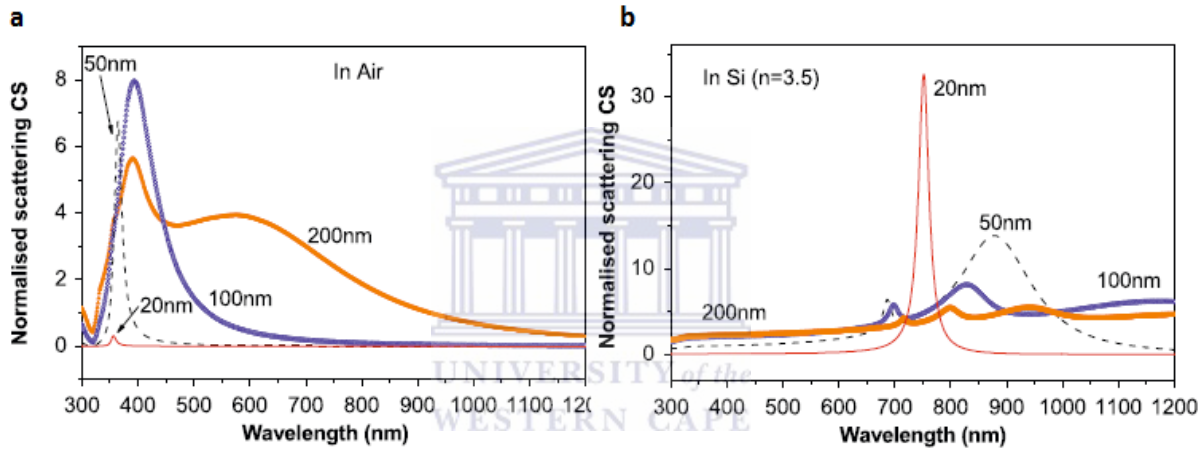

Figure 2.11: Normalised scattering cross sections of spherical particles with different size in different dielectric media a) In air, b) In silicon [2.16]

From figure 2.11 (a) and (b) it is evident that the scattering cross section is greatly dependant on the size of the nanoparticles. Figure 2.11 (a) shows how the scattering cross sections vary with spherical particles of different sizes in a medium of air. The optimum size for which scattering takes place is at a 100nm, whereas smaller particles would absorb more light. Figure 2.11 (b) shows the scattering cross sections of the same spherical particles in a medium of silicon. Resonance peaks shift to longer wavelengths as the size of the particles increase as well as when they are under the influence of a substrate that contains a relatively high refractive index. This is evident in figure 2.11 (b) as all the resonant peaks are red shifted to greater wavelengths [2.17].

2.2.3 Shape of nanoparticles

When the shape of the particles is altered, the resonant frequency varies greatly since the curvature of the particles is proportional to the restoring force produced by the nanoparticles. Particles with sharper corners have a greater degree of charge separation, since charges tend to concentrate at sharp corners [2.18]. The enhanced charge separation result in an overall decrease in the Coulombic restoring force which in turn increases the time each oscillation takes resulting in a decreased frequency. The symmetry of the nanoparticles also play a major role since the charge separation would be more pronounced [2.18].

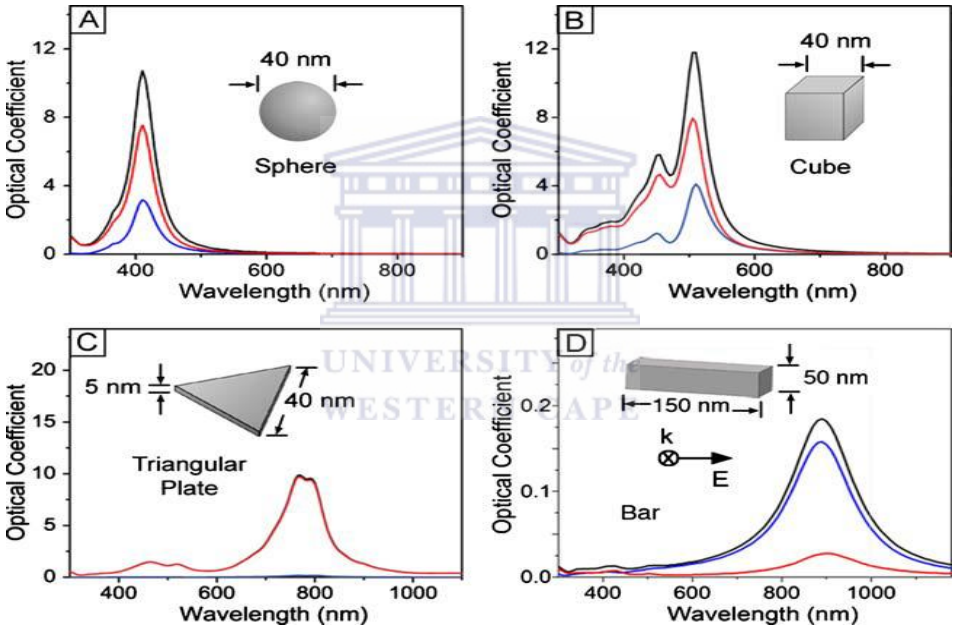

Figure 2.12: UV-VIS spectra of silver nanoparticles of various shapes. Red indicates the absorption spectra; blue indicates scattering and black indicates the extinction spectra [2.18].

Figure 2.12 shows how the UV-VIS spectra of nanoparticles vary with particles of various shapes. When the incident radiation hits the spherical particles, the particles polarize, forming a dipole. The electrons on the one side of the particles will be drawn back as a result of Coulombic attraction, however when the sign of the induced electric field changes a dipole is brought about in the opposite direction. This phenomenon causes the electrons to oscillate at the same frequency as that of the incident electromagnetic radiation, hence giving rise to a

resonance peak at 410nm as shown in figure 2.12 (a). The smaller shoulder observed in figure 2.12 (a) is a quadrupole resonance peak and may be attributed to the interaction of non-uniform electromagnetic radiation across the spherical particle [2.27]. Figure 2.12 (b) shows the UV-VIS spectra of a cubed nanoparticle similar sized as the spherical particle exhibited in figure 2.12 (a). Although these particles are similar sized, the resonance peak of the cube is significantly shifted to longer wavelengths. The red-shift is due to a greater degree of charge separation in particles with sharp corners. The Coulombic restoring force is significantly decreased as a result of the enhanced degree of charge separation, thus causing the time needed for each oscillation to increase, which in turn results in a decreased frequency. The additional peak in the spectra of the cubed structure may be attributed to the degree of symmetry of the particle, this is an indication of the various ways in which the electron density of the particles may be arranged [2.18].

Decreasing the symmetry of the particle even further, by producing triangular particles as shown in figure 2.12 (c) will result in even greater degrees of charge separation, resulting in a significant red-shifted resonance peak. Silver nano-bars have even greater red-shifted resonance peaks as compared to the previously mentioned structures. The long axis of the nanobar causes a greater charge separation across the length of the nano-bar, if the interaction of the light is randomized, two dipole resonance peaks should be observed due to the longitudinal and transverse axis of the bar. Since the charge separation in the transverse direction would be relatively small, in comparison to the longitudinal direction, a resonance peak will be observed at shorter wavelengths for the transverse direction, whilst the longitudinal direction will give rise to a red-shifted resonance peak [2.18].

From figure 2.12 it is thus evident that the number of resonant peaks present in the UV-VIS spectra of a solution of nanoparticles, is an indication of the shapes of the particles formed, as well as the various kinds of ways whereby the electron density can be polarized [2.18].

2.2.4 Dielectric Medium

From equation 2.14, it is evident that the scattering cross section of the nanoparticles is greatly dependant on the dielectric medium.

The coupling of the radiation modes of the nanoparticles are therefore dependant on the dielectric layer above and below the nanoparticles. When silver particles are surrounded by a dielectric medium, the resonance peak shifts to regions of larger wavelengths (redshift). The redshift is owed to the depolarising interaction between the electrons and the embedding medium, since the electrons sense the presence of the boundary [2.19].

As a result of the enhanced optical properties of metal nanoparticles, they may be incorporated into a thin film, such that it may enhance the efficiency of solar cells. The mechanisms whereby the metal nanoparticles are incorporated are of great importance, to obtain optimal performance of the nanoparticles.

2.3 Metal nanoparticles as a light trapping mechanism in solar cells.

For efficient light trapping in solar cells, the absorber of the solar cell should be relatively "optically thick" such that it will allow complete light absorption and photo carrier current collection. In order to obtain enhanced efficiencies, the solar cells require thicknesses that are several times smaller than the minority carrier diffusion lengths [2.8].

The incorporation of the metal structures in thin film solar cells can offer at least three ways to enhance the overall solar cell efficiency; light trapping by scattering from metal nanoparticles at the surface of the solar cell, by the excitation of localized surface plasmons, and by the excitation of surface plasmons.

2.3.1 Light trapping by scattering from metal nanoparticles at the surface of the solar cell

When light is scattered from metal nanoparticles that are placed in a homogenous medium, the light is scattered in a symmetrical manner, in both the forward and reverse directions [2.8]. However when the particles are placed in a non-homogenous medium, i.e. interface between two mediums with varying dielectrics, the light will tend to scatter in the direction of the material with a larger permittivity. Given that the incident radiation is scattered at an angle beyond the critical angle for reflection, the incident radiation will remain trapped in the cell. This effect can further be enhanced with the help of metal back reflectors since the light reflected by the back contacts towards the surface of the cell will be re-radiated. Thus causing the incident light to pass through the cell numerous amount of times resulting in an overall enhancement in the optical path length of the cell [2.8].

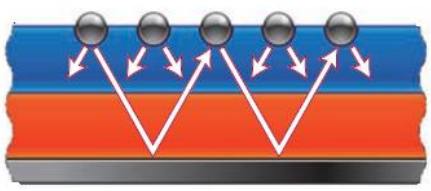

Figure 2.13: Schematic diagram of light trapping by placing metal nanostructures on the surface of the solar cell [2.8].

Figure 2.13 shows how the incident light is scattered by the nanoparticles, forcing the light to go into the semiconducting device. The metal back contact assists in trapping by scattering the light in the direction of the metal nanoparticle, such that it can be scattered several times.

2.3.2 Light trapping by the excitation of localized surface plasmons.

Another effective way in which light can be trapped in a thin film solar cell is by the means of excitation of localized surface plasmons (LSP). The incident radiation is stored by the metal nanostructures in a LSP mode. The excitation of the localized surface plasmons allow the creation of electron-hole pairs attributed to the near field coupling of the nanoparticles [2.8].

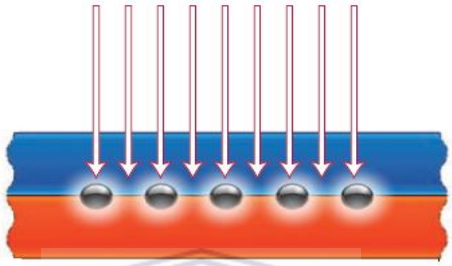

Figure 2.14: Schematic diagram of the incorporation of nanoparticles inside the active layer of the solar cell to allow the creation of electron-hole pairs by the excitation of LSP's [2.8].

Figure 2.14 illustrates how the metal nanostructures store the incident radiation in the semiconducting material, as a result of the excitation of LSP's.

2.3.3 Light trapping by the excitation of surface plasmons.

Light trapping may also be achieved by converting the incident light to surface plasmon polaritons (SPP's). These are electromagnetic waves that travel along an interface between a metal back contact and the absorber layer of the semiconductor. The incident light can be guided and trapped relatively effectively in the semiconducting layer since the light incident on the particle will be absorbed laterally in the semiconducting material [2.36].

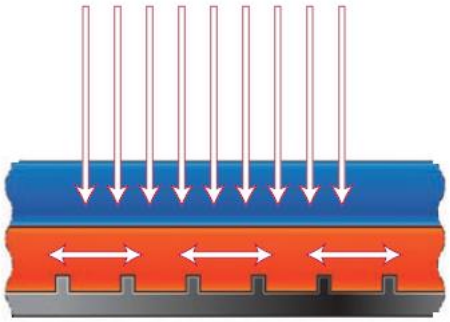

Figure 2.15: Schematic diagram of the process whereby the light is converted to SPP modes as a result of the interface between the semiconductor and the metal [2.36].

Figure 2.15 shows how the incident radiation is converted into SPP modes at the metal/semiconductor interface. The ridges of the metal allow the light to be rotated at a 90° angle such that the light is stored laterally in the plane of the semiconducting layer [2.36].

Silver nanoparticles exhibits, the highest plasmon excitation efficiency among the three metals (silver, copper and gold) that display plasmon resonance [2.20]. This is attributed to their size confinement to dimensions well below the mean free path and an increased density of conduction electrons. The interaction of light of one silver nanoparticle is more proficient than any other particles consisting of the same dimension [2.20]. The primary reason distinguishing silver from any other nanoparticle is the ability to tune the plasmon resonance to any wavelength in the visible spectrum [2.11]. These properties are mainly dependant on the size, shape and dielectric medium of the nanoparticles.

The size and shape of the nanoparticles is mainly dependant on the synthesis procedure employed to obtain silver nanoparticles.

2.4 Synthesis of silver metal nanoparticles.

There are a series of techniques that may be employed for the synthesis of silver nanoparticles, such as photochemical, microwave irradiation, electrochemical methods, and chemical reduction [2.21].

2.4.1 Photochemical Reduction

Photochemical reduction is a process whereby a silver salt is reduced in the presence of a suitable reducing agent and of a surfactant under UV-light. This method is relatively simple as well as reproducible; however the method produces a relatively broad particle size distribution and requires a UV lamp which could be costly [2.22].

2.4.2 Microwave Irradiation

In the process of microwave irradiation a silver solution is heated up by means of dielectric losses. This means that energy lost by the solution heats up a dielectric material present in a varying electric field. Thermal energy is thus obtained by the conversion of radiated energy. This method of synthesis yields various sizes and shapes due to non-homogenous nucleation processes during the process of formation. Since this method relies on increasing temperatures, the temperature acts as a catalyst such that the reaction occurs at a faster rate. Although the reaction occurs relatively fast, the particles are relatively non-homogenous in size. The process also requires expensive equipment that may also be complex since the temperature of the solution need to be monitored constantly whilst the solution is in the chamber [2.23].

2.4.3 Electrochemical Synthesis

Electrochemical methods of producing metal nanoparticles are among the simplest methods for the production of silver nanoparticles. Two electrodes are placed a certain distance away, such that the anode and cathode exist at opposite ends as to create a potential difference. The electrodes consist of silver in its bulk form. The silver electrodes are then placed into an electrochemical cell, containing distilled water. The positively charged Ag ions formed by the oxidation are then attracted to the cathode at the opposite end, thus resulting in the formation of a neutralized Ag atom. The metal nanoparticles are then formed by interaction of Van Der

Waal's forces among the neutral silver atoms [2.24, 2.25]. Although electrochemical synthesis has been reported to produce nanoparticles that are relatively uniformly sized at a large scale, the noble metal ions tend to coat the cathode electrode relatively easily when produced in aqueous phase [2.24, 2.25].

2.4.4 The Chemical Reduction Method

The chemical reduction synthesis is a technique employed by most scientists for the preparation of silver nanoparticles. The method involves the controlled reduction of silver salt in a solution, with the aid of a suitable reducing agent. The nanoparticles are formed from the ions of the metal in the aqueous phase, via nucleation and growth processes. The chemical reduction synthesis can control the particle characteristics by varying experimental conditions such as the concentrations of reactant, temperature, pH of the solution as well the stabilizers and reducing agents. The polyol method is a relatively simple chemical reduction method used for the production of silver metal nanoparticles [2.26].

2.4.4.1 The Polyol Method

The polyol process has been described as a relatively suitable method for producing nanostructures from easily reduced metals. During the process, a metal salt is reduced by dissolving into a suitable solvent, which is often a polyol, an alcohol consisting of several hydroxyl groups. While the metal salt is dissolved in the solvent, heat and stirring may be supplied to the solution to act as a catalyst during the reaction process [2.27].

To produce silver nanoparticles, silver nitrate is used as the salt to provide the silver ions:

$$Ag^{+} + e^{-} \rightarrow Ag \tag{2.14}$$

During the reaction process the reduction does not take place via the solid phase, instead it does this by utilising the solution, hence allowing nucleation and growth processes to govern

the formation of the nanoparticles. As a result of the high dielectric media of the polyol, it acts as a solvent for the initial inorganic material present in solution [2.27].

In order to obtain mono-sized metal nanoparticles, the nucleation and growth processes should occur separately [2.27].

The concentration of the metal species is increased until it reaches its saturation limit, thus allowing nucleation of the species. When this occurs a series of nuclei are produced in relatively short bursts, allowing them to grow relatively fast. The concentration of the metal species is high enough such that particle growth can proceed at a rate that will consume all the metal species produced in the solution [2.27].

The supply of temperature and stirring allow the particles to be characterized by Brownian motions which lead to enhanced surface mobility of the particles. Sintering would therefore result in increased probabilities of collision, agglomeration and coalescence. Stabilizers (surfactants) prevent sintering of the particles by inhibiting the formation of metal-metal bonds. The presence of the stabilizer produces an increased rate of spontaneous nucleation thus producing more nuclei during the nucleation process which in turn contributes to an overall increase in the number of particles, with a small particle size distribution [2.27].

The sizes of the nanoparticles are also controlled by the strength of the reducing agent. It has been shown that stronger reducing agents produce smaller particles. Since most of the particles are formed during the initial stages of the synthesis, a decrease in the time of the growth process is required to inhibit the growth of larger particles [2.27, 2.28].

2.5 Particle Growth of nanoparticles.

The growth process of nanoparticles takes place in 2 stages, namely:

(1) Nucleation and

(2) Subsequent growth of nuclei.

2.5.1 Nucleation

The nucleation process of the growth of the nanoparticles may be described by the classical nucleation theory, discovered by Volmer and Weber in 1926, which was further developed by Becker and Doring in 1935 [2.29]. It begins with the formation of the nucleus; this can be described by using the Gibb's free energy:

$$\Delta G = \Delta\mu_v + \Delta\mu_S = \left(\frac{4}{3}\right)\pi r^3 \Delta G_v + 4\pi r^2 \gamma\,, \tag{2.15}$$

where, ΔG is the Gibb's free energy of nucleation, $\Delta\mu_v$ the volume energy, $\Delta\mu_S$ the surface energy, r the radius of the nucleus formed, ΔG_v the change in the Gibb's free energy per unit volume of solid phase and γ the surface energy per unit area [2.29].

New stable nuclei progresses to form and grow larger until the radius of the spherical particles eventually exceed the critical size r^* as a result of a greater stability. When the radius of the nuclei is less than that of the critical size, the nucleus will dissolve in the medium (solution), resulting in an overall decreased total energy. However when the radius of the nucleus increases such that $r = r^*$ then $\frac{d\Delta G}{dr} = 0$ and r^*, the critical radius is defined by [2.29]:

$$r^* = \frac{-2\gamma}{\Delta G_v} \tag{2.16}$$

The corresponding critical energy is then given by:

$$\Delta G^* = \frac{16\pi\gamma}{3(\Delta G_v)^2} \tag{2.17}$$

ΔG^* and r^* is the energy that the process must overcome and the barrier radius, respectively.

The nucleation process occurs in the metastable state in which $\Delta G^* > kT$. The rate at which nucleation occurs is given by:

$$R_N = nPT = \left\{\frac{C_0 kT}{3\pi\lambda^3\eta}\right\} e^{\left(\frac{-\Delta G^*}{kT}\right)} \quad , \tag{2.18}$$

where R_N is the rate of nucleation per unit volume, P the probability, n the number of growth species per unit volume, T the successful jump frequency of growth species, and C_o the solubility, λ the diameter of the growth species and η the viscosity of the solution [2.29].

The rate of nucleation is thus enhanced when the initial concentration of solute is relatively high and when the viscosity as well as the critical energy barrier is relatively low [2.29].

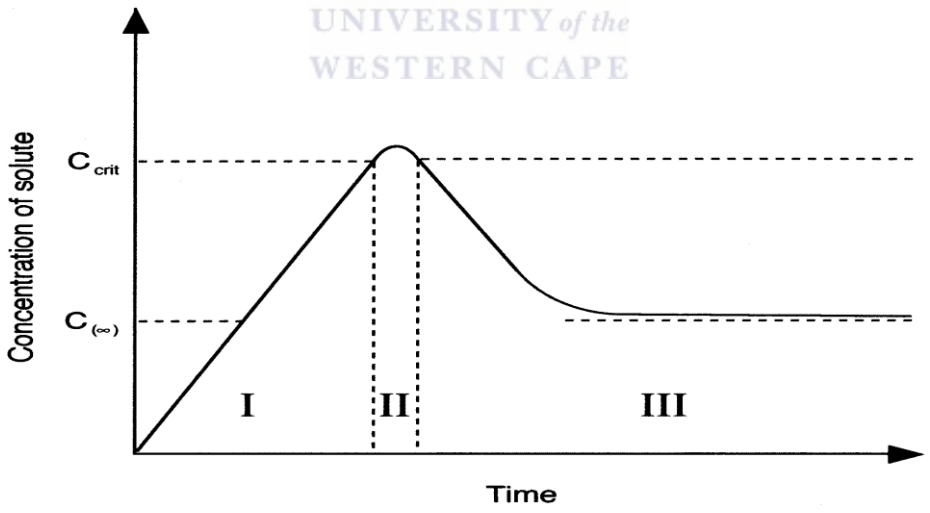

Figure 2.16: Schematic diagram of the growth process of the nanoparticles [2.30].

Figure 2.16 shows that as the concentration of the solute increases, nucleation does not occur until it reaches a saturation point at which it exceeds a critical solubility allowing the

nucleation process to begin. The pre-nucleation, nucleation and growth stage of the nanoparticles are represented by regions I, II and III, respectively [2.30].

After the primary nucleation phase, an overall decrease is observed in the concentration of the solute, which in turn causes an overall decrease in the volume Gibb's free energy. The nucleation process comes to a halt, such that the growth phase of the process will proceed.

Particles of uniform size distributions are obtained if all nuclei formed in the solution occur simultaneously, and if they have the same dimensions. Thus all conditions during the formation should be relatively similar [2.29, 2.30].

2.5.2 Subsequent Growth of nuclei

This process is used to determine the size of the particles present in the solution. The growth process consists of a series of steps that will yield the desired nanoparticles, namely:

I. Formation of growth species
II. The dispersion of the bulk growth species onto the growth surface.
III. Adsorption of the growth species onto the growth surface
IV. Surface growth through irreversible incorporation of growth species onto the solid surface.

The above mentioned steps may be further categorized into two stages, the growth controlled diffusion and growth controlled by a surface process [2.29].

2.5.2.1 Growth controlled by diffusion.

The growth of the nanoparticles will continue once nucleation process comes to a halt. This will occur when the amount of growth species present in the solution reduces well below the threshold concentration for nucleation. Given that the process is controlled by diffusion, the growth rate may then be defined by:

$$r^2 = k_D t + r_0^2, \tag{2.19}$$

where r is the radius of the nucleus, $k_D = 2D(C - C_s)V_m$ where D is the diffusion coefficient, C the bulk concentration of growth species, C_s the growth species concentration present on the surface of the particles, V_m the molar volume of nuclei and r_0 the initial radius of the nuclei [2.29].

As the particles in the solution continue to increase in size, the radial difference δr decreases for an initial change in the radius δr_0:

$$\delta r = \frac{r_0 \delta r_0}{r} \tag{2.20}$$

Combining equation (2.19) and (2.20) yields:

$$\delta r = \frac{r_0 \delta r_0}{(k_D t + r_0^2)^{\frac{1}{2}}} \tag{2.21}$$

Thus proving that uniform particle size is governed by diffusion growth process since the radial difference increases as the nuclear radius is increased. It also shows that an increase in the time t will yield smaller radial differences which in turn lead to an overall decrease in the radial difference of all the particles [2.29].

2.5.2.2 Growth controlled by a surface process.

Surface processed growth occurs when the growth by diffusion is relatively rapid. There are two underlying processes governing the surface process, namely mononuclear and poly-nuclear growth.

Mononuclear growth occurs when the growth species area is formed by consecutive layers. The following layer will only begin to form once the previous layer of growth species is

completed. This process thus allows the growth species with enough time to diffuse onto the surface. As a result the growth rate and surface area is directly related by:

$$\frac{1}{r} = \frac{1}{r_0} - k_m t, \tag{2.22}$$

where k_m is a concentration dependant constant. Replacing r the radial difference equation yields [2.29]:

$$\delta r = \frac{\delta r_0}{(1 - k_m r_o t)^2}, \tag{2.23}$$

where $k_m r_o t < 1$. This therefore shows that that the radial difference is increased with an increase in time.

In poly-nuclear growth, the growth species do not form layer by layer, instead the next layer will form before the first layer of growth is completed. The size and time of reaction do not affect the growth rate. Since the growth rate of the particles is a constant, the process will occur linearly:

$$r = k_p t + r_0 \ , \tag{2.24}$$

where k_p is a temperature dependant constant. As a result, the radial difference will remain a constant [2.29].

Growth processes are dominated by mononuclear processes when the nuclei formed are relatively small. However for larger nuclei the poly-nuclear growth dominates. When relatively large particles are grown the process is dominated by diffusion, however these processes may vary according to the various reaction conditions [2.29].

Diffusion limited growth processes will ensure formation of particles with an even size distribution. This can be achieved by limiting the concentration of the growth species to a

minimum, which would result in an increased diffusion distance, hence limiting the diffusion. The viscosity of the solution may thus also be employed in order to limit the diffusion process, as well as the manipulation of reaction rates during the synthesis procedure [2.29].

2.6 Stabilization of nanoparticles

Nanoparticles are relatively unstable due to the attractive forces between them. These forces cause the nanoparticles to agglomerate and form a bulk material, which is undesired. The particles interact via their Van der Waal forces, which is highly dependent on the separation distance between the two particles [2.31].

In order to prevent this, the particles require an opposite force; this opposing force is obtained by employing electrostatic and steric stabilization mechanisms [2.31].

2.6.1 Electrostatic stabilization

Stability of particles may be enhanced as a result of electric charges present on the surface of the particles. Ions are adsorbed onto the surface of the charged metal particle by the surfactant, causing the formation of an electric double layer around the metal nanoparticle. The double layer thus gives rise to Coulombic repulsion forces between the nanoparticles and is exponentially dependant on the distance between the particles present in the solution [2.31].

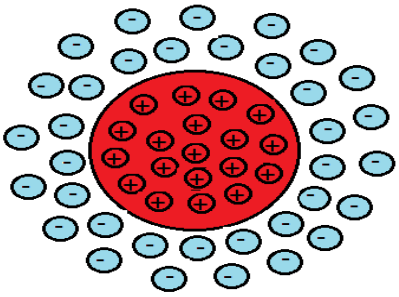

Figure 2.17: Schematic diagram of the electrostatic stabilization process.

Figure 2.17 shows that the stabilizing compound interacts with the nanoparticles by means of electrostatic attractive forces, thus "binding" the nanoparticles to the stabilizer such that it prevents any further agglomeration of the nanoparticles.

2.6.2 Steric Stabilization

During the process of steric stabilization large molecules are adsorbed onto the surface of the nanoparticles creating a barrier between the particles. The barrier thus inhibits the process of agglomeration between the nanoparticles [2.31, 2.32].

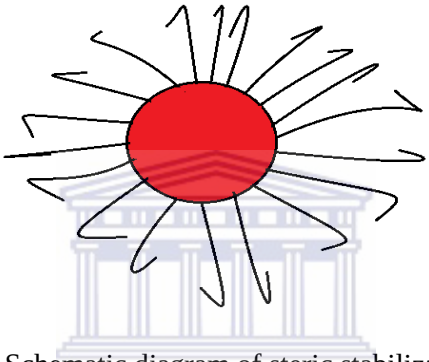

Figure 2.18: Schematic diagram of steric stabilization process.

Figure 2.18 illustrates how the stabilizing agent is adsorbed onto the nanoparticle; the adsorbed stabilizing agent then prevents the agglomeration of the nanostructures.

The nature of the surfactants or stabilizers will determine the mechanism by which it will interact with the metal particle [2.32].

2.6.3 Classification of surfactants

There are anionic surfactants, cationic surfactants, non-ionic surfactants and amphoteric surfactants [2.32]. Surfactants are molecules that consist of both polar and non-polar groups at opposite ends of a molecule [2.33].

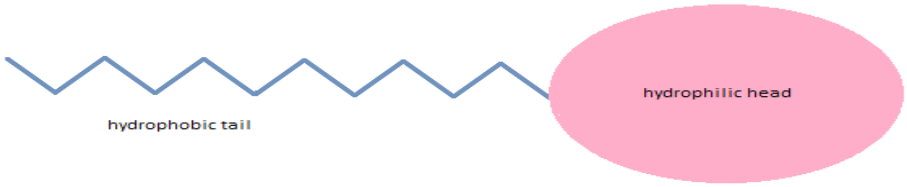

Figure 2.19: Schematic diagram of the basic structure of a surfactant molecule.

The polar head of the molecule is hydrophilic (water loving), whilst the non-polar tail exhibit hydrophobic properties (water hating) (figure 2.19). The hydrophilic ends of the molecules are usually ionic or non-ionic as a result of its polarity. Surfactant molecules prevent particles from interacting by decreasing the surface tension of the particles [2.33].

The class of the surfactant is defined by the nature of the polar group:

Anionic surfactants

These type of surfactants have negatively charged hydrophilic groups, such as carboxyl ($RCOO^-M^+$), sulfonate ($RSO_3^-M^+$) or sulfate ($ROSO_3^-M^+$) [2.32, 2.33, 2.34].

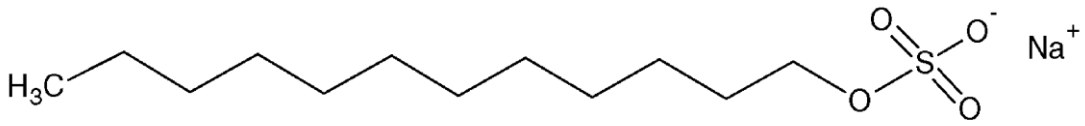

Figure 2.20: Structure of an anionic surfactant, sodium dodecyl sulfate [2.34].

Cationic surfactants

Cationic surfactants have hydrophilic groups that are positively charged, such as ammonium halides ($R_4N^+Cl^-$) and chitosan (figure. 2.6) [2.32, 2.33, and 2.35].

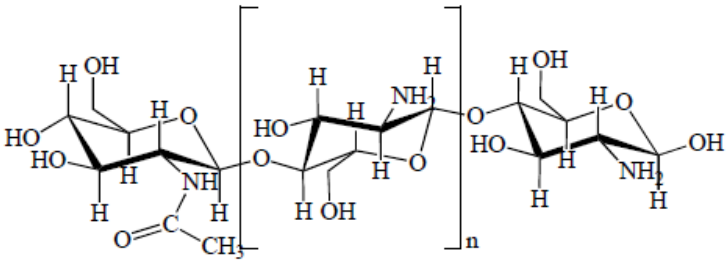

Figure 2.21: The structure of chitosan, a cationic surfactant [2.35].

Non-ionic surfactants

These surfactants consist of a neutral hydrophilic group, such as Polyvinylpyrrolidine (PVP), brij or any other polyol groups [2.32, 2.33, 2.36].

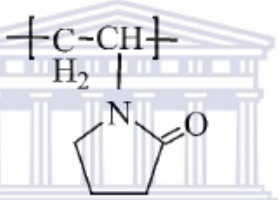

Figure 2.22: The structure of the non-ionic surfactant, PVP [2.36].

Amphoteric surfactants

In amphoteric surfactant compounds the charge of the hydrophilic group is greatly dependant on the pH of the medium, thus it can either be positive, negative or both. An example of these types of surfactants is $RN^{+}(CH_3)_2CH_2CH_2SO_3^{-}$ and 3[(3Cholamidopropyl)dimethylammonio]-1-propanesulfonate [2.31,2.33, 2.37].

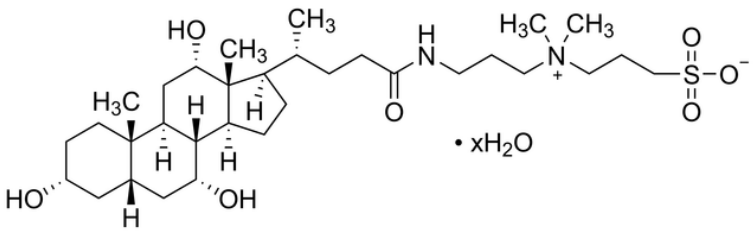

Figure 2.23: The structure of 3-[(3-Cholamidopropyl)dimethylammonio]-1-propanesulfonate [2.37].

The effect of the surfactants, particle growth and synthesis of the silver nanoparticles may be investigated by making use of a set of characterization techniques, hence the section to follow will discuss the characterization techniques used to analyse silver nanoparticles and thin films.

2.7 Conclusions

The literature review shows that the use of silver nanoparticles may be employed to enhance efficiencies of solar cells due to their interaction with electromagnetic radiation. Lithographic and thermal evaporation techniques seem to be the most widely used techniques to deposit the silver nanoparticles onto thin film solar semiconductors, however these methods are relatively expensive and complex, thus simple cost effective techniques such as spin coating, spraying and drop coating appear to be more attractive method to deposit silver nanoparticles onto thin films. The silver nanoparticles deposited onto the thin film require certain specifications that would allow for optimal optical performance of the nanostructures. Thus a controlled synthesis should be employed to obtain these nanoparticles. There are many techniques that may be used to synthesise nanoparticles, however most of these techniques have the limitation that they are expensive and complex. The polyol synthesis process is a relatively simple inexpensive technique to produce nanoparticles; however this technique yields nanoparticles that are poorly dispersed. Parameters such as stabilizers, reducing agents and temperature should be adapted such that the synthesis may be controlled.

As a result of the limitations presented by the silver nanoparticle synthesis and the deposition on thin films, scientific research on parameters that would yield a controlled synthesis of silver nanoparticles with optimal performance should be employed. Once this is obtained, these nanostructures may be incorporated into thin films such that they may provide and efficient thin film device at relatively low cost.

2.8 Aims and Objectives

The main research goals of this study is to synthesize silver nanoparticles using the polyol method and to vary experimental parameters in order to gain further insight into some of the factors that affect the formation of silver nanoparticles. The synthesized silver nanoparticles will then be incorporated into the thin films to determine whether the nanoparticles may be used as scatterers to guide the incident electromagnetic radiation into the active layer of the thin film.

These aims will be obtained by following a set procedure:

1. Synthesis of silver nanoparticles
    - 1.1 Prepare silver nanoparticles at room temperature using the polyol method and structurally characterize the nanoparticles.
    - 1.2 Investigate the effect of temperature.
    - 1.3 Study the effect of reaction time.
    - 1.4 Study the effect of using a different solvent.
    - 1.5 Investigate the effect of surfactant concentration on silver nanoparticle formation
    - 1.6 Investigate the probability of using chitosan, a biodegradable polymer, as a surfactant to stabilize silver nanoparticles.

2 Preparation of thin films
    - 2.1 Incorporate silver nanoparticles into thin films by using a spray technique to deposit the silver nanoparticles onto bare corning glass and a-Si deposited thin films.
    - 2.2 Measure the optical properties of the prepared thin films, in terms of reflectance and transmission.

2.3 Structurally characterize the thin films to determine if the deposition technique used allowed for an even distribution of the silver nanoparticles on the thin films.

By investigating all the parameters described above, it could help solve the main objectives of this work.

2.9 References

[2.1] Wurfel. P, "Physics of Solar Cells: From Principles to New Concepts", *Wiley VCH,* (2005)

[2.2] Singh. J, "Semiconductor Devices: Basic Principles", *John-Wiley,* (2001)

[2.3] Serway. R, "Physics for Scientists and Engineers with Modern Physics", *CBS college publishing,* (1986)

[2.4] Mishra. K, and Singh. J, "Semiconductor Device Physics and Design", *Netherlands: Springer,* p 60-64 (2008)

[2.5] Nelson. J, "The Physics of Solar Cells", *London: Imperial College Press,* (2003)

[2.6] Shah. A, "Thin-Film Silicon Solar Cells", *EPFL Press,* (2010)

[2.7] Kittel. C, "Introduction to Solid State Physics", *John-Wiley & Sons,* (2005)

[2.8] Atwater. H. and Polman. A,. *Nature materials*, **9,** p 205 (2010)

[2.9] Naumann. R, "Introduction to the Physics and Chemistry of Materials", *Taylor and Francis Group,* (2009)

[2.10] Poortmans. J, and Arkhipov. V, "Thin Film Solar Cells: Fabrication, Characterization and Applications", *John Wiley & Sons,* (2006)

[2.11] Evanoff. D, and Chumanov. G, *Chemphyschem*, **6**, p 1221 (2005)

[2.12] Freestone. I, Meeks. N, Sax. M, and Higgitt. C, *Gold Bulletin,* **40**, p 270 (2007)

[2.13] Liz-marzan. L, *Mater. Today*, **7**, p 26 (2004)

[2.14] Xia. Y, and Halas. N,*MRS Bull*., **30**, p 338 (2005)

[2.15] Nanobiotechnology, accessed 01 August 2013, [Online]

http://www.nanobiotech.uni-mainz.de/157_ENG_HTML.php

[2.16] Pillai. S, and Green. M, *Sol. Energy Mater. Sol. Cells*, **94**, p 1481 (2010)

[2.17] Catchpole. K, and Polman. A, *Opt. Express*, **16**, p 21793(2008)

[2.18] Cobley. C, and Skrabalak. S, *Plamonics*, **4**, p 171 (2009)

[2.19] Pillai. S. Surface Plasmons for enhanced thin-film silicon solar cells and light emitting diodes. *University of New South Wales*, (2007).

[2.20] Evanoff. D, Chumanov. G, *J.Phys.Chem B*, **108**, p 13957 (2004)

[2.21] Zhao. T, Sun. R, Yu. S, Zhang. Z, Zhou. L, Huang H, and Du. R, *Colloids Surf., A*, **366**, p 197 (2010)

[2.22] Sau. T, Pal. A, Jana. N, Wang. Z, and Pal. T, *J. Nanopart. Res.*, **3**, p 257 (2001)

[2.23] Jiang. L, Wang. A, Zhao. Y, Zhang. J, and Zhu. J, *Inorg. Chem. Commun.*, **7**, p 506 (2004)

[2.24] Yin. B, Ma. H, Wang. S, and Chen. S, *J. Phys. Chem*, **107**, p 8898 (2003)

[2.25] Khaydarov. R, Khaydarov. R, Gapurova. O, Estrin. Y, and Scheper. T, *J. Nanopart. Res.*, **11,** p 1193 (2008)

[2.26] Nair. L, and Laurencin. C, *J. Biomed. Nanotechnol.*, **3**, p 301 (2007)

[2.27] Carotenuto. G, Pepe. G, and Nicolais. L, *Eur. Phys. J. B*, **16**, p 11, (2000)

[2.28] Rycenga. M, Cobley. C, Zeng. J, Li. W, Moran. C, Zhang. Q, Qin. D, Xia. Y, *Chem. Rev.*, **111**, p3669 (2011)

[2.29] Cao. G, "Nanostructures and Manomaterials: Synthesis, Properties and Applications", *London: Imperial College Press,* **3**, p 53 (2004)

[2.30] Sugimoto. T, Shiba. F, Sekiguchi. T and Itoh. H, *Colloids Surf., A,* **164,** p 183 (2000)

[2.31] Rozenberg. B and Tenne. R, *Prog. Polym. Sci*, **33**, p 40 (2008)

[2.32] Myers. D, *VCH publishers,* p 8, 279 (1992)

[2.33] Perkins, S, *ATI*, (1998)

[2.34] Huang. R.Y.M, Moon. G.Y and Pal. R, *J. Membr. Sci.*, **184**, p 1 (2001)

[2.35] Aranaz. I, Mengíbar. M, Harris. R, Paños. I, Mirralles. B, Acosta. N, Galed. G, Heras. Á, *Current Chemical Biology*,**3**, p 203 (2009)

[2.36] Wang. H,Qiao. X, Chena. J, Wang. X, and Ding. S, *Mater. Chem. Phys.*, **94**, p 449 (2005)

[2.37] Sigma-Aldrich [Online] http://www.sigmaaldrich.com/catalog/product/aldrich/226947?lang=en&region=ZA, accesed 21 August 2013

CHAPTER 3

Experimental Techniques

3.1Introduction

This Chapter provides a description on the synthesis employed for the preparation of silver nanoparticles, and can be found in Section 3.2 of this Chapter. It also provides a detailed explanation of the analytical techniques used to acquire information about the properties of the silver nanoparticles, and the thin films. Table 3.1 provides an overview of the analytical techniques employed, as well as the information that each technique provides.

Table 3.1: Analytical techniques used for the analysis of silver nanoparticles and thin films.

Characterization Technique	Information
Ultra Violet Visible Spectroscopy	Optical Properties of silver nanoparticles and thin films
High Resolution Transmission Electron Microscopy	Morphology and Particle size of silver nanoparticles
Scanning Electron Microscopy	Surface Morphology of thin films
X-ray Diffraction	Crystalline Phases, Crystallite Sizes of silver nanoparticles
Thermogravimetric Analysis	Thermal Properties of silver nanoparticles

3.2 Synthesis of silver nanoparticles

All chemicals used for the synthesis of silver nanoparticles was purchased from the supplier and used without any further purification. In a typical experiment, approximately 0.25 g of silver nitrate ($AgNO_3$) was dissolved in a solution mixture of 1.9 g of PVP and 50 g of

ethanol. The solution was stirred with a magnetic stirrer at approximately 750 rpm at room temperature for a period of 1day. Powdered samples of the silver nanoparticles were obtained by means of rotary evaporation [3.1]. All glassware was cleaned with concentrated nitric acid (55%) prior to use.

A list of chemicals used, with their corresponding supplier and purity is provided in Table 3.2.

Table 3.2: Chemicals used to synthesize silver nanoparticles.

Chemicals/Solvents	Purity	Suppliers
Silver nitrate ($AgNO_3$)	99.2 % (AR)	Merck
Ethylene Glycol	99% (AR)	KIMIX
PVP		Calbiochem
Chitosan		Aldrich Chemistry
Ethanol	99 % (AR)	B&M Scientific
Nitric Acid	55 %	B&M Scientific

The formation of the silver nanoparticles in the solution was indicated by a colour change from clear to brown. The effect of reaction time at room temperature, followed by the influence of temperature, and the reaction time at elevated temperature was investigated. The effect of surfactant concentration and effect of a different surfactant and solvent was also investigated in order to obtain the optimal reaction conditions for obtaining uniform particle size and shape distribution.

3.2.1 Effect of reaction time at room temperature

The effect of reaction time at room temperature on the formation of silver nanoparticles was investigated by dissolving 0.2506 g of $AgNO_3$ in a solution of 1.9038 g of PVP and 50.0772 g of ethanol, the solution was stirred at room temperature at a magnetic stirring speed of 750

rpm. Samples of the solution were drawn at time intervals of 1, 3 and 5hours as well as 1, 3 and 6 days. A colour change from clear to brown was observed.

3.2.2 Effect of reaction temperature: room temperature vs. reflux temperature (80^0 C)

Since a period of 6 days was a relatively long time period for the synthesis of the nanoparticles, the effect of temperature during the synthesis of silver nanoparticles was investigated. The synthesis of the sample was performed at 80° C under refluxing conditions. The reaction conditions employed are displayed in Table 3.3. A colour change from clear to brown was observed.

Table 3.3: Synthesis conditions of samples prepared for the investigation of the effect of reaction temperature on the formation of silver nanoparticles.

$AgNO_3$ (g)	PVP (g)	Ethanol (g)	Temperature (^{o} C)
0.2508	1.9144	50.0323	Room Temperature(~17.2° C)
0.2511	1.9056	49.7867	80°C

3.2.3 Effect of Reaction time at reflux temperature (80^0C)

The effect of reaction time at reflux temperature was investigated by dissolving 0.2524 g of $AgNO_3$ in a solution of 1.9096 g of PVP and 49.8653 g of ethanol; the solution was stirred using a magnetic stirrer at 750 rpm, at a reflux temperature of 80° C using a silicone oil bath. Small aliquots of the solution were drawn at consecutive time intervals of 1 hour, ranging from 1 to 6 hours. The sample was then left to cool to room temperature in the silicone oil bath overnight. A colour change from clear to brown was observed.

3.2.4 Effect of PVP concentration at 80^0 C

In order to obtain the optimal surfactant concentration required to produce uniform silver nanoparticles, the effect of the concentration on the formation of silver nanoparticles was investigated. This was obtained by preparing reactions with increasing concentrations of PVP. The solution was stirred using a magnetic stirrer at 750 rpm, at a reflux temperature of 80° C for 6 hours using a silicone oil bath. After the reaction the solution was left to cool in the silicone oil bath. Table 3.4 shows the synthesis conditions used to investigate the effect of PVP concentration. A colour change from clear to brown was observed.

Table 3.4: Concentration of reactants used to investigate the effect of PVP concentration on the formation of silver nanoparticles at 80 ^{0}C.

AgNO (g)	PVP (g)	Ethanol(g)
0.2524	1.9046	49.9986
0.2535	2.4118	50.411
0.2528	5.039	50.0931
0.2504	7.506	50.9291
0.2528	12.5036	50.326

3.2.5 Effect of solvent

The effect of solvent was investigated by dissolving 0.2499g of $AgNO_3$ in a solution of 1.9080g of PVP and 50.2145g of ethylene glycol. The suspension was heated at a reflux temperature of 200°C (close to the boiling point of ethylene glycol) in a silicone oil bath, under magnetic stirring of 750 rpm for 6 hours. The solution was left to cool to room temperature. A colour change from clear to dark green was observed.

3.2.6 Effect of a different surfactant

The effect of a different surfactant in the formation of silver nanoparticles was investigated by employing the use of Chitosan as a surfactant, rather than PVP. The silver nanoparticle

suspension was prepared by reacting 0.2506g of $AgNO_3$ with a solution of 1.9155g Chitosan and 50.3756 g of ethylene glycol. The suspension was heated at a reflux temperature of 200° C, and magnetically stirred at 750 rpm, in an oil bath. The solution was then left to cool to room temperature. A colour change from clear to brown was observed.

3.3 Preparation of the thin films

Thin films were prepared by depositing a layer of silicon on a corning glass substrate by means of hot wire chemical vapour deposition (HWCVD). A film of nanoparticles was then deposited on top of the thin film by spraying an ethanol based silver suspension and an ethylene glycol based suspension onto the substrate several times, and then followed by annealing at 80° C and 200° C respectively, such that the solvent could be evaporated.

3.4 Characterization Techniques

3.4.1 Ultra Violet Visible Spectroscopy (UV-VIS)

3.4.1.1 Introduction

UV-VIS spectroscopy is a technique that utilizes visible, near infrared and near ultraviolet light for analysis. The region absorbed by the material extends from 190-400nmwhich corresponds to the ultra violet (UV) range, whilst ranges from 400-780 nm correspond to the visible range. When this kind of electromagnetic radiation interacts with molecules, the electrons of the molecules undergo transitions. Absorption spectroscopy is the process whereby transition occurs from the ground state, whereas in the case of emission spectra the transition occurs from the excited state to the ground state [3.2].

3.4.1.2 Theory

When a solution is exposed to light, the light may either be absorbed by the solution or transmitted. The ratio of the intensity of the incident light (I_0) and the intensity of the light that has passed through the solution (I_t) is known as the transmittance.

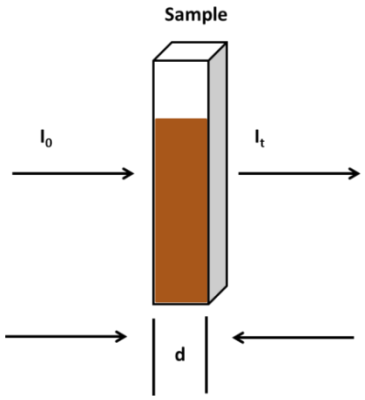

Figure 3.1: An illustration of the Beer-Lambert law.

Figure 3.1shows a light beam I_o striking a solution contained in quartz glass (cell). When the beam has passed through the cell, the incident light beam has a reduced intensity $I_{t,}$ as a result of absorption by the sample, reflection losses caused by interaction with the cell windows and scattering by the particles suspended in the solution. The interaction of the light with the dissolved sample results in absorption losses. The reflection and scattering losses are accounted for by running identical cells, which contain only the solvent [3.2].

The transmittance T, can thus be obtained from:

$$T = \frac{I_t}{I_0} \approx \frac{I_{solution}}{I_{solvent}} \tag{3.1}$$

The absorbance is directly related to the number of absorbing species present in the solution. The absorbance A, is given by:

$$A = -\log T = \log \frac{I_0}{I_t} \tag{3.2}$$

The Beer-Lambert law is the most important principle in absorption analysis, and is given by:

$$A = \varepsilon . c . d \tag{3.3}$$

The Beer-Lambert law states that for any given system, there exists a linear relationship between d, the thickness of the cell; the concentration of the solution c, and a constant ε, the molar absorptivity. At greater concentrations the molar absorptivity may vary, which would result in an overall deviation in the linearity of the working curve.

All of the molecules present in the solution may absorb various wavelengths of radiation, thus there are various light absorbing groups that may be absorbed, and these groups are known as chromophores. The absorption of the UV and visible light are due to excitations of the valence electrons. There are three types of transitions that may occur, namely pi (π), sigma (σ), non-bonding (n) electrons, d and f electrons and transitions which involve the charge transfer of electrons [3.2].

Electrons within molecules are excited from their ground state to a high energy excited state when they absorb electromagnetic radiation. When this occurs the atoms in the molecules rotate and vibrate. The vibration and rotation states have relatively closely packed energy levels as shown in figure 3.2. As a result excitations within these levels require relatively small amounts of energy [3.2].

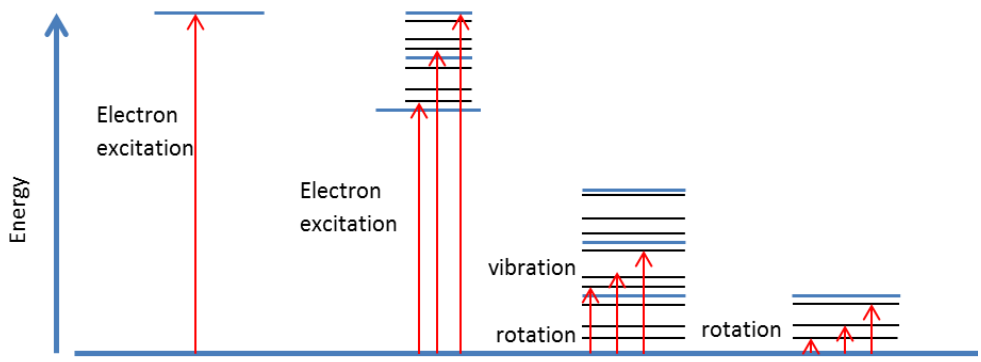

Figure 3.2: Rotational and vibrational electronic levels of molecules.

The light absorbing groups (chromophores) require relatively small amounts of energy to be excited from their ground state. These groups are those which include transitions of the $n \rightarrow \pi^*$, $\pi \rightarrow \pi^*$, within molecular orbitals, charge transfer bonds and d and f electron transitions.

In the normal UV-VIS range $n \rightarrow \sigma^*$, σ bonds and isolated double bonds present in organic complexes are not excited, and will therefore not be taken into account. As a result of the superimposed rotational and vibrational states the electronic states consist of a series of overlapping lines, thus forming a continuous absorption band [3.2].

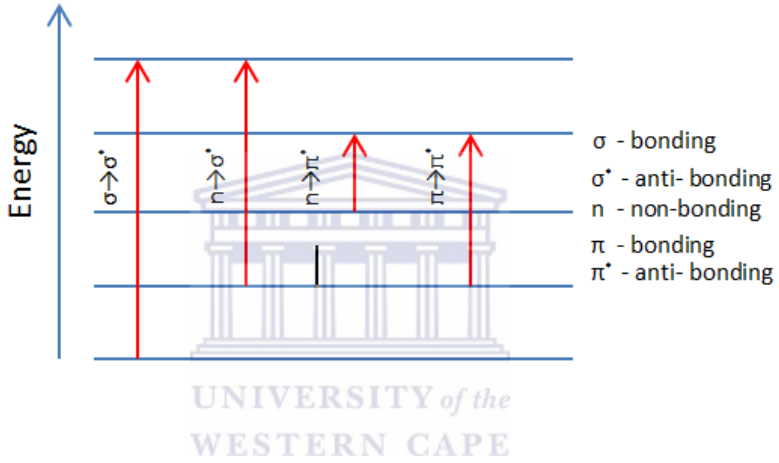

Figure 3.3: Various possible electronic transitions in a molecule.

Figure 3.3 highlights the various transitions that the chromophores may have as a result of the continuous absorption band.

$n \rightarrow \pi^*$ and $\pi \rightarrow \pi^*$ transitions occurs in their near ultraviolet and visible regions. $n \rightarrow \pi^*$ transitions are responsible for relatively high intensity peaks in the absorption spectra, the presence of multiple bonds in the molecule will determine the intensity of these peaks. The number of conjugated bonds present in the molecule is indirectly related to the spacing between the π and π^* levels. Thus an increase in the number of conjugated bonds corresponds to decreased π and π^* level spacing resulting in an increase of the probability of the transition and in turn an increase in the intensity of the peak of the observed spectrum [3.3].

Charge transfer bonds are formed when molecules are excited by near ultraviolet light; these bonds are attributed to the excitation of electrons from a donor molecule to an acceptor molecule. d-d transitions are observed in the near ultraviolet regions and occur as a result of interatomic d-d transitions. These electronic transitions occur in ions of transition metals that have unfilled d orbitals [3.3]

3.4.1.3 Band gap analysis

The band gap of a material is known as the amount of energy required to excite electrons form the valence to the conduction band. Bulk Metals, such as silver, have relatively small to no band gaps (conduction and valence band overlaps), hence making them electrically conductive, whilst insulators have relatively large band gaps with very few electrons present in their conduction bands. Semiconductor materials have intermediate band gaps, thus when sufficient energy is provided, electrons from the valence band may be excited to the conduction band. When considering the band gaps of metal nanoparticles, such as silver, the energy levels vary significantly in comparison to bulk silver. Nanoparticles have larger band gaps, with more discrete energy levels [3.4]. This property may be attributed to the quantum confinement effects of the nanoparticles having sizes of only a few atoms wide. This effect predicts that a band gap will increase as the size of silver nanoparticles decrease, since the energy levels will become more discrete [3.5].

The relationship between the intensity of the transmitted radiation, I_t and incident radiation I_0 is given by:

$$I_t = I_0 \exp(-\alpha L) \tag{3.4}$$

where α and L represent the absorption coefficient and path length, respectively. The absorption coefficient, α is related to the excitation energy by:

$$\alpha = Const.(h\nu - E_g)^{\frac{1}{m}} \tag{3.5}$$

Which may be written in terms of absorbance, A by:

$$\frac{A}{L} = Const.(h\nu - E_g)^{\frac{1}{m}} \tag{3.6}$$

The term $h\nu$ represents the photon energy, whilst E_g represents the band gap of the semiconductor [3.6]. The optical band gap of semiconductors is generally obtained by plotting the absorption coefficient α (ν) as $(\alpha(\nu)h\nu)^{\frac{1}{m}}$ vs.$h\nu$, where m represents the nature of the transition and $h\nu$ the photon energy respectively. The nature of the transition, m may vary such as $\frac{1}{2}, 2, \frac{3}{2}$, or 3 for allowed direct, allowed indirect, forbidden direct and forbidden indirect transitions, respectively. Since silver nanoparticles undergo direct transition, a value of $m = \frac{1}{2}$ was selected in equation 4.6. The linear extrapolation of the plot of A^2 vs. $h\nu$ produces the band gap energy E_g[3.4, 3.7].

3.4.1.4 Reflectance

Reflection from a surface occurs when a fraction of electromagnetic radiation, incident on the surface of a specimen is returned into the same hemisphere, in which the radiation has originated from. The reflection of the radiation may either be specular or diffuse. Specular reflectance refers to a mirror like reflection, whilst diffuse reflectance refers to the scattering of the light into the entire hemisphere [3.8, 3.9]

The reflectance *R*, may be defined as ratio of the reflected radiant flux Φ_r, to the incident radiant flux Φ_i:

$$R = \frac{\Phi_r}{\Phi_i} \tag{3.7}$$

The spectral reflectance, may similarly be defined at specific wavelength λ, as:

$$R(\lambda) = \frac{\Phi_{\lambda r}}{\Phi_{\lambda i}} \tag{3.8}$$

The spectral reflectance factor is the ratio of the spectral flux reflected from a material to the spectral flux, which would ideally be reflected by a perfect diffuse reflector. A single reflectance descriptor may not be sufficient to distinguish between the vast amount of possible geometries [3.8, 3.9].

The geometric descriptor of reflection is therefore the bidirectional reflectance distribution function (BRDF), f_r. The BRDF is defined as the differential component of the reflected radiance, dL_r, per unit differential component of radiant incidence, dE_i, both in a specified direction:

$$f_r(\theta_i, \emptyset_i, \theta_r, \emptyset_r) = \frac{dL_r(\theta_i,\emptyset_i,\theta_r,\emptyset_r,E_i)}{dE_i(\theta_i,\emptyset_i)} \tag{3.9}$$

Where, θ, is defined as the polar angle, and measured from the surface to the normal, $\emptyset$, is the azimuth angle, measured from an arbitrary reference in the plane of the surface (usually the plane which contains the incident beam). The subscripts *i*, and *r*, represent the incident and reflected beams, respectively [3.8].

3.4.1.5 Experimental set-up

UV-VIS spectrophotometers are used to obtain UV-VIS spectrums. The spectrophotometer has two independent radiation sources, namely the UV and visible. Xenon or deuterium lamps supply UV radiation, whilst visible light is provided by tungsten and halogen lamps.

A monochromator that filters the light is used so that a single wavelength of the incident radiation reaches the detector. Cuvettes hold the sample in place and a detector measures the radiation once is has passed through these cuvettes. The detector converts the incident electromagnetic radiation into electrical energy. Photodiodes, photomultipliers, photocells

and photo resistors allow the transformation of the signal to be linear, a condition that should be net by the detector [3.2, 3.3].

There are two types of spectrophotometers that may be used for UV-VIS analysis, a single and double beam spectrophotometer. The single beam spectrophotometer allows all the light to pass through the sample and I_0 is measured when there is no sample present in the detector (figure 3.4). In the double beam spectrophotometer the incident light is split into two beams before it strikes the sample (figure 3.5). The one beam passes through the sample, whilst the other is used as a reference cell (baseline). The two detectors receive the signal, simultaneously, however only one beam is allowed to pass through the ratio one at a time [3.2, 3.3].

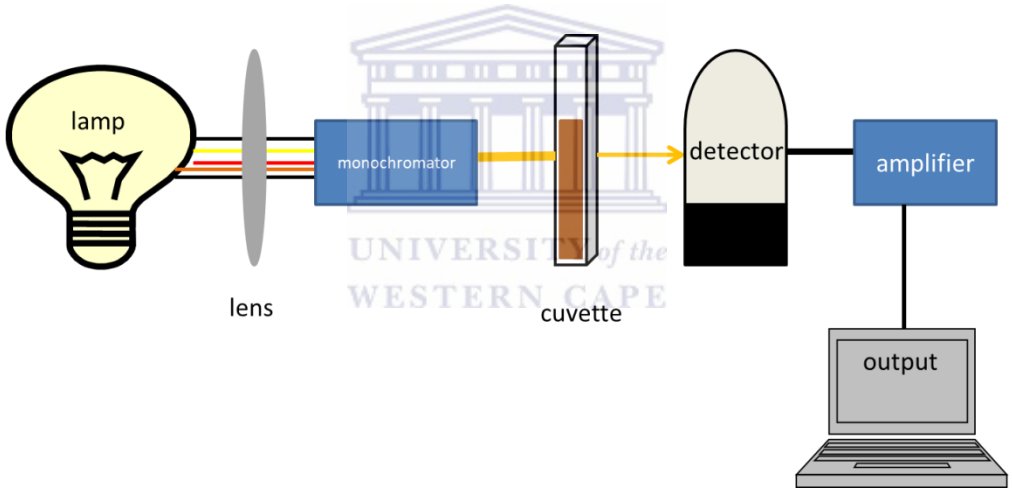

Figure 3.4: Schematic diagram of a single beam photo spectrometer.

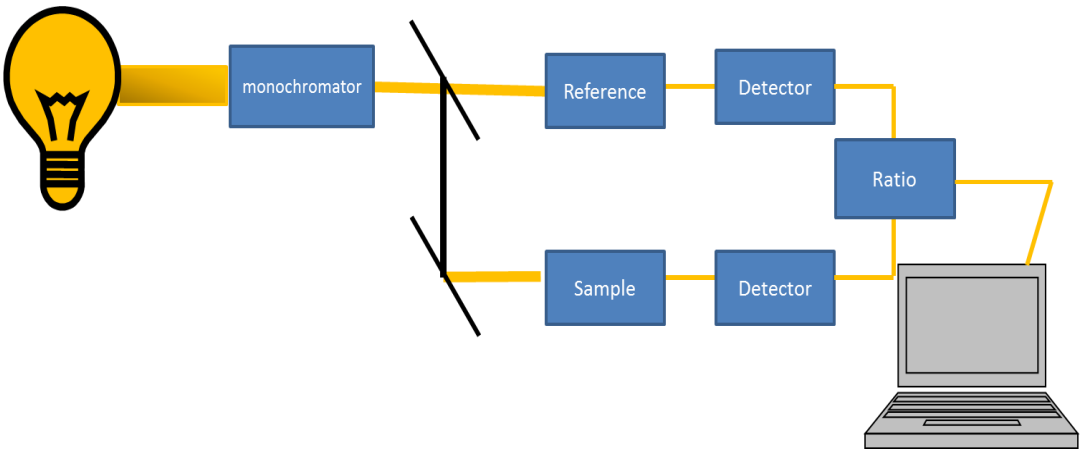

Figure 3.5: Schematic diagram of a double beam photo spectrometer.

The absorbance spectra of silver nanoparticles were recorded using a Thermo Nicolet 100 double beam spectrophotometer, in absorbance mode in the range of 200-700 nm.

The experimental set up of specular and diffuse measurements is illustrated in figure 3.6. For specular reflectance measurements, a monochromatic light is allowed to pass through a beam splitter. The light reflected is deviated by the splitter towards a detector (figure 3.6 (a)). Diffuse reflectance measurements; make use of an integrating sphere to obtain measurements (figure 3.6 (b)). The integrating sphere contains a white coating on the inside, with a diffuse reflectance close to 1. The light that is scattered diffusely by the sample, is reflected a significant amount of times inside the integrating sphere, before reaching the detector.

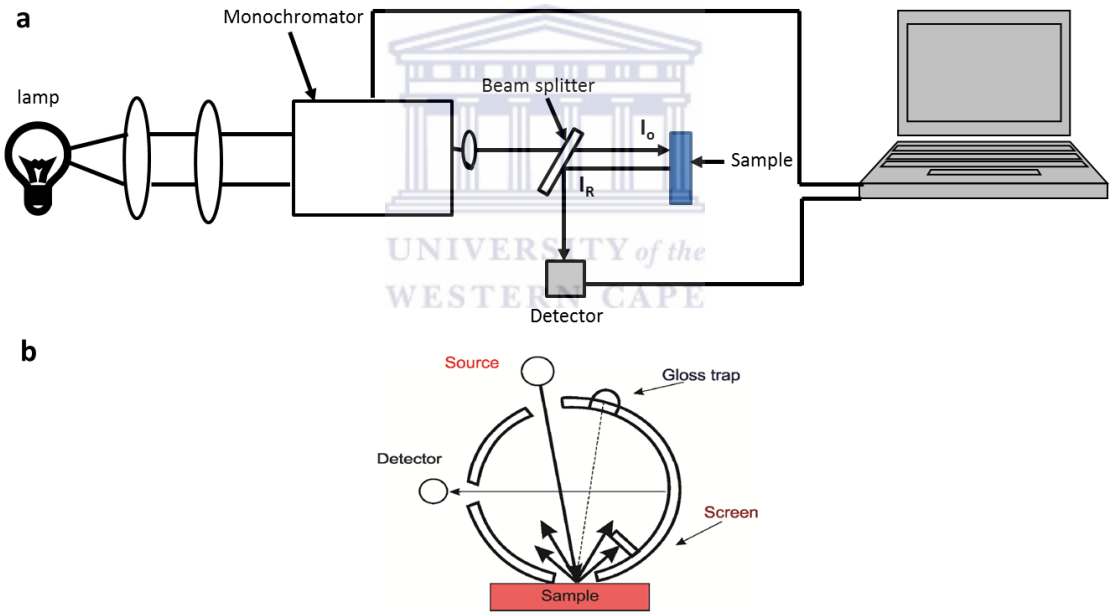

Figure 3.6: Schematic diagram of the experimental set-ups of (a) specular and (b) diffuse reflectance [3.10].

Transmission and diffuse reflectance spectroscopy measurements were performed using a Cary 1 E, in the range of 200-800nm.Specular reflectance measurements were performed with a Semiconsoft inc, Mbrobe Thin-film measurement system, with a resolution of 1 nm, in the range of 200 nm to 800nm.

3.4.2 High Resolution Transmission Electron Microscopy (HRTEM)

HRTEM is a relatively powerful technique used widely by scientists of vast fields in order to obtain information about the shape, size, surface and most importantly, crystallography of a given specimen. The information provided by this technique is based on an image forms by the interaction of the specimen with electrons [3.2, 3.11]

3.4.2.1 Electron beam specimen interaction

When a specimen is exposed to an electron beam, the electrons incident on the specimen holds three possible fates;

I. Transmitted without interaction with the atoms in the specimen.
II. Undergoes elastic scattering (deflected but loses an un detectable amount of energy)
III. Inelastic scattering (deflected and loses a significant amount of energy)

If all these types of electrons are used to form an image; all the regions of the image of the specimen will look exactly the same. This would therefore produce an image with no contrast between areas of various thicknesses and composition. By separating the scattered electrons from the unscaterred electrons, an image with contrast can be produced. This may be obtained by the use of an objective aperture [3.11].

The fate of 100 electrons falling on a model specimen is schematically illustrated by figure 3.7. region (a) consists of amorphous carbon with a thickness of 10 nm. This atom is relatively light, therefore electrons are scattered very poorly, as a result only 9 of the incident 100 electrons are deflected by an angle of approximately 0.5 °. The thickness of region is two times greater than that of region (a), thus scattering more electrons at a greater angle, approximately 17 of the electrons will be deflected relatively strongly. A sample with the same thickness as region (b) but consisting of very heavy amorphous lead will deflect a significant amount of electrons; however the angle of deflection will remain relatively small.

Region (d) consists of the same thickness but consist of crystalline lead. Diffraction can therefore take place and the scattered electrons will be amplified in some regions, but cancelled in others. The scattered electrons will then travel in specific directions at the Bragg angle θ_B to that of the unscattered beam. The thickness and orientation of the specimen will determine the amount of electrons emerging from the diffracted and unscattered beams [3.11].

No difference in the image of regions (a), (b), (c) and (d) will be observed if all 100 of the electrons are able to travel down the column of the microscope, resulting in an image with no contrast.

The use of the objective aperture below the specimen (figure 3.7 (e)) can therefore 'stop' all the electrons which are scattered at angles greater than 0.5°. As a result regions (a)-(d) will look relatively different. The brightness of the image of various regions will depend on the amount of unscattered electrons passing through the aperture [3.11].

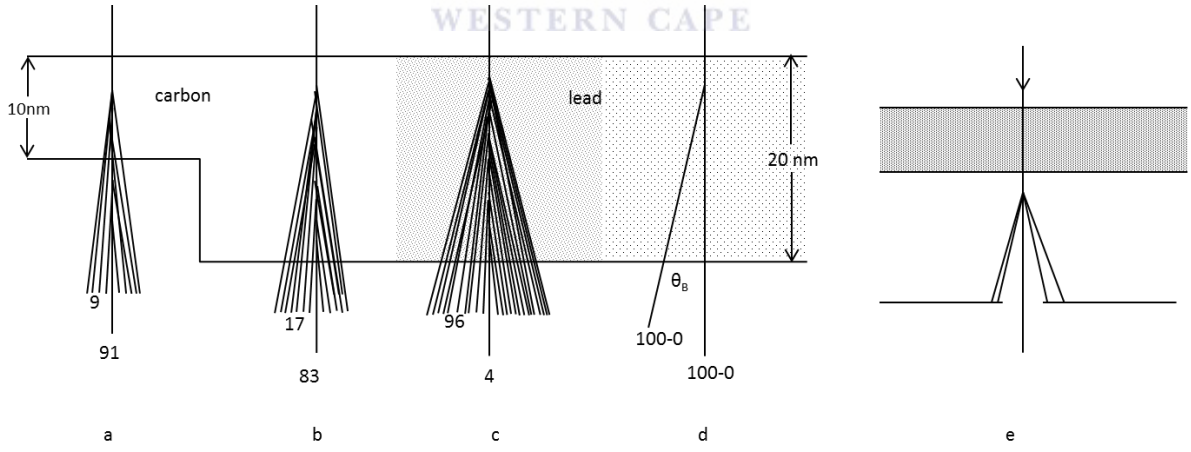

Figure 3.7: The fate of 100 electrons incident on different regions of a model specimen. The numbers show the amount of electrons scattered through an angle greater than 0.5°, as well as those that are unscattered. figure 3.6 (a) amorphous carbon with thickness of 10 nm, figure 3.6 (b) amorphous carbon with thickness of 20nm, figure 3.6 (c) amorphous lead of 20 nm, figure 3.6 (d) crystalline lead

of 20 nm thickness, and figure 3.6 (e) effect of the objective aperture which stops all the electrons scattered through more than an angle of 0.5°

3.4.2.2 Electron diffraction

A transmission electron microscope provides two types of information about a given specimen, a magnified image and a diffraction pattern. The way in which the diffraction pattern arises can be observed by the examination of electron optics of a projection microscope [3.12].

Figure 3.8 shows the electron optics of a two stage projection microscope. Two parallel rays leaves specimen AA' before obtaining the first image at at BB' all the rays that are parallel to the blue rays will pass through point D' and all the rays parallel to the red rays pass through at point D. for each set of parallel rays exiting the specimen there is a correlative point in the plane DD', this plane is known as the back focal plane of the objective lens. If the ray patterns are followed through a second projector lens, a similar set of second points will be formed in the plane EE'.DD' and EE' are the positions at which the diffraction patterns will be observed , and BB' and CC' the positions at which images will be observed [3.12].

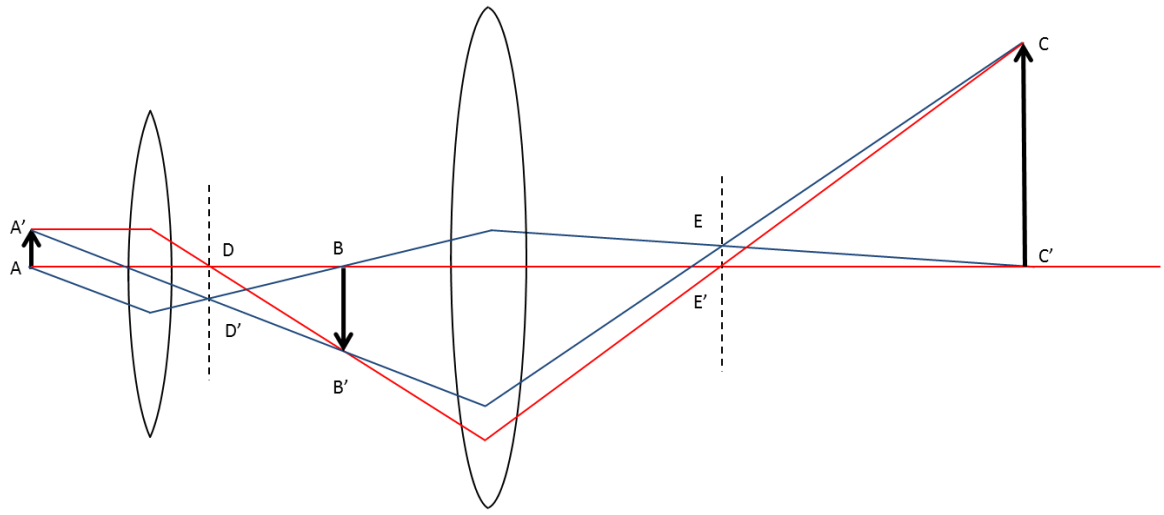

Figure 3.8: The rays diagram of a two stage projection microscope, the positions of the image (BB' and CC') and diffraction patterns (DD' and EE').

The diffraction pattern is obtained upon the interaction of the electron beam with a crystalline material, this results in strong scattering of the electron beam, given by the Bragg Law:

$$2dsin\theta = n\lambda \tag{3.10}$$

Where d is the interplanar spacing, θ the angle of scattering, *n* an integer and λ the wavelength of an electron [3.12].

Braggs law is only satisfied when the crystal is orientated in such that the incident electron beam satisfies the diffraction angle for the specific plane. Given that most of the electrons diffracted are concentrated in the Bragg condition, a crystal grain would thus appear bright if the beam passes through the objective aperture and dark when prevented by the aperture [3.12].

In a given crystal there may be many other planes that could diffract electrons, with their own corresponding interplanar d-spacing, thus an understanding of planes and directions within the crystal is required. Miller index notation may be used to interpret the diffraction patterns obtained. Using the notation for the cubic crystal for the interplanar spacing of planes with indices (hkl) is given by:

$$d_{hkl} = \frac{a}{\sqrt{h^2+k^2+l^2}} \tag{3.11}$$

Where *a* is a lattice constant. The integer *n* in equation (3.10) is the order of diffraction, and occurs when *n* is any integer number. In electron diffraction it is conventional to consider only the 1st order of diffraction, equation (3.10) therefore becomes:

$$\lambda = 2dsin\theta \tag{3.12}$$

Due to the relatively short wavelengths of the electrons used in electron microscopy, the angles of at which these electrons scatter are relatively small, therefore $sin\theta = \theta$, and equation (3.10) further reduces to:

$$\lambda = 2d\theta \tag{3.13}$$

Since θ is relatively small, strong diffraction will only occur from planes of atoms that are almost parallel to the beam.

When an electron beam is incident on a crystalline material, some of the electrons will pass through the material, without any interaction and hit a screen a distance L away from the specimen at point B, whilst other electrons will be diffracted through an angle of 2θ by crystal planes with interplanar spacing d, hitting the film at A, a distance r from O (figure 3.9), thus for diffraction at small angles :

$$\frac{r}{L} = 2\theta \tag{3.14}$$

Combining equations (3.13) and (3.14) yield:

$$rd = \lambda L \tag{3.15}$$

λL is known as the camera constant since the camera length L and the wavelength λ are non-specimen dependant. Therefore the distance of a diffraction spot from that of an un diffracted spot, r, is inversely related to the interplanar d spacing of the diffracted planes [3.12].

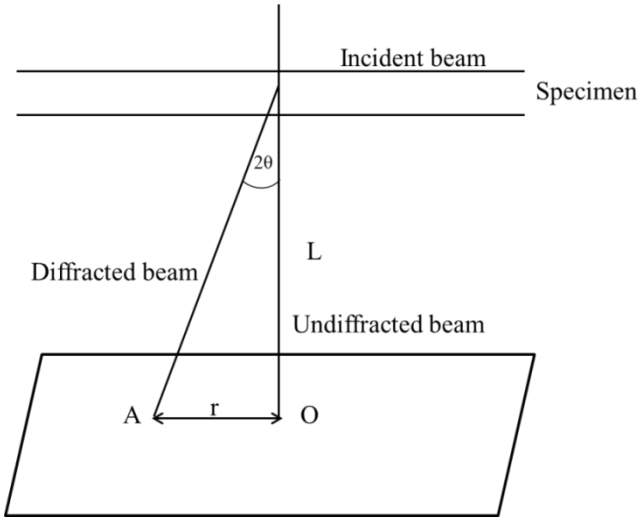

Figure 3.9: Schematic diagram of the geometry of the formation of a diffraction pattern.

3.4.2.3 Different diffraction patterns

Given that planes of a crystal would diffract electrons if these planes were approximately parallel to the electron beam, a single crystal specimen orientated in such a way that that a series of planes are parallel to the incident beam will produce a diffraction pattern with a regular array of spots (figure. 3.10 a). Figure 3.10 b shows a specimen consisting of a crystals with various crystal orientations, this specimen will therefore produce a diffraction pattern in which the spots fall in rings. For specimens containing a significant amount of crystal orientations, a diffraction pattern with continuous rings will be observed (figure 3.10 c) [3.12].

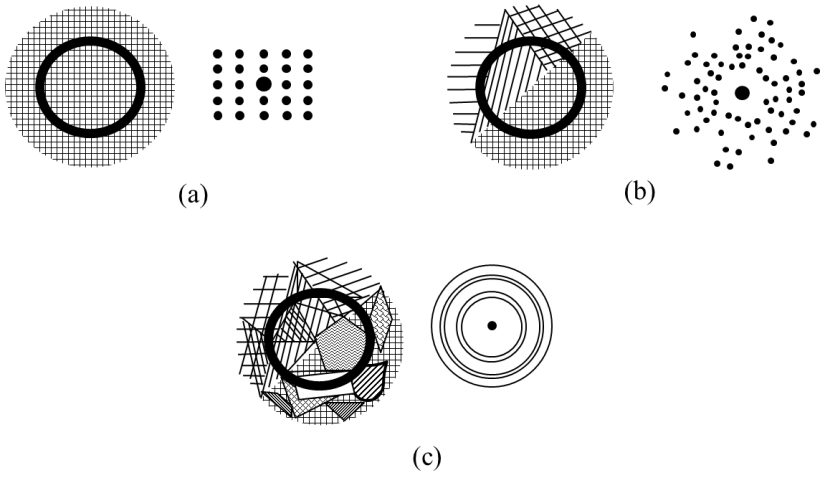

Figure 3.10: Shows the various types of diffraction patterns produced from various crystal orientations, (a) a perfect crystal, (b) a specimen with a small number of grains and (c) a significant amount of randomly orientated grains.

3.4.2.4 Operating principles

The TEM consists of an electron gun, a series of electromagnetic lenses, a viewing screen and a camera, all of which are stacked into a vertical microscope column as shown in figure 3.11.

The electrons are supplied by a heated filament emitting an abundance of light and electrons. The electrons are accelerated towards an anode such that a beam of electrons with controlled energy is produced. The electron beam may be deflected in such a way that they are aligned parallel to the optical axis, thus function is controlled by the gun deflector coils. The area of the specimen illuminated is controlled by the condenser system; consisting of a first and second condenser lens. The beam is focused to a relatively small spot by the first condenser lens, therefore effectively controlling the optical spot size so that the condenser can obtain a spot size less than 1μm.The second condenser lens then controls the angle of convergence, of the electron beam, and the area of the specimen which is illuminated[3.12].

The condenser aperture is then used to control the number of electrons allowed into the electron beam, thus controlling the intensity of illumination. Astigmatism in the illumination system is then compensated for by the use of a condenser stigmator. The electron beam is then focused by with the aid of the wobbler coils, whilst the alignment coils direct the beam towards the optical axis [3.11, 3.12].

The most crucial part of the microscope is the specimen chamber. This chamber contains the objective lens, objective aperture and the objective stigmator coils. The first intermediate image and diffraction pattern of the specimen are produced by the first objector lens. The objective aperture is found in the back focal plane of the objective lens and is used to enable the operator to control the electrons that will contribute to the formation of the final image of the specimen. The 'selected area' aperture is found in the plane of the first intermediate image and allows a certain region of the image to be selected for analysis. The magnification of the image is then controlled by the use of the 1^{st} and 2^{nd} intermediate lenses. The projector lens then assists in magnifying the central part of the image and projects it onto the fluorescence screen which displays the image. A charge coupled device (CCD) camera records the image [3.8, 3.12].

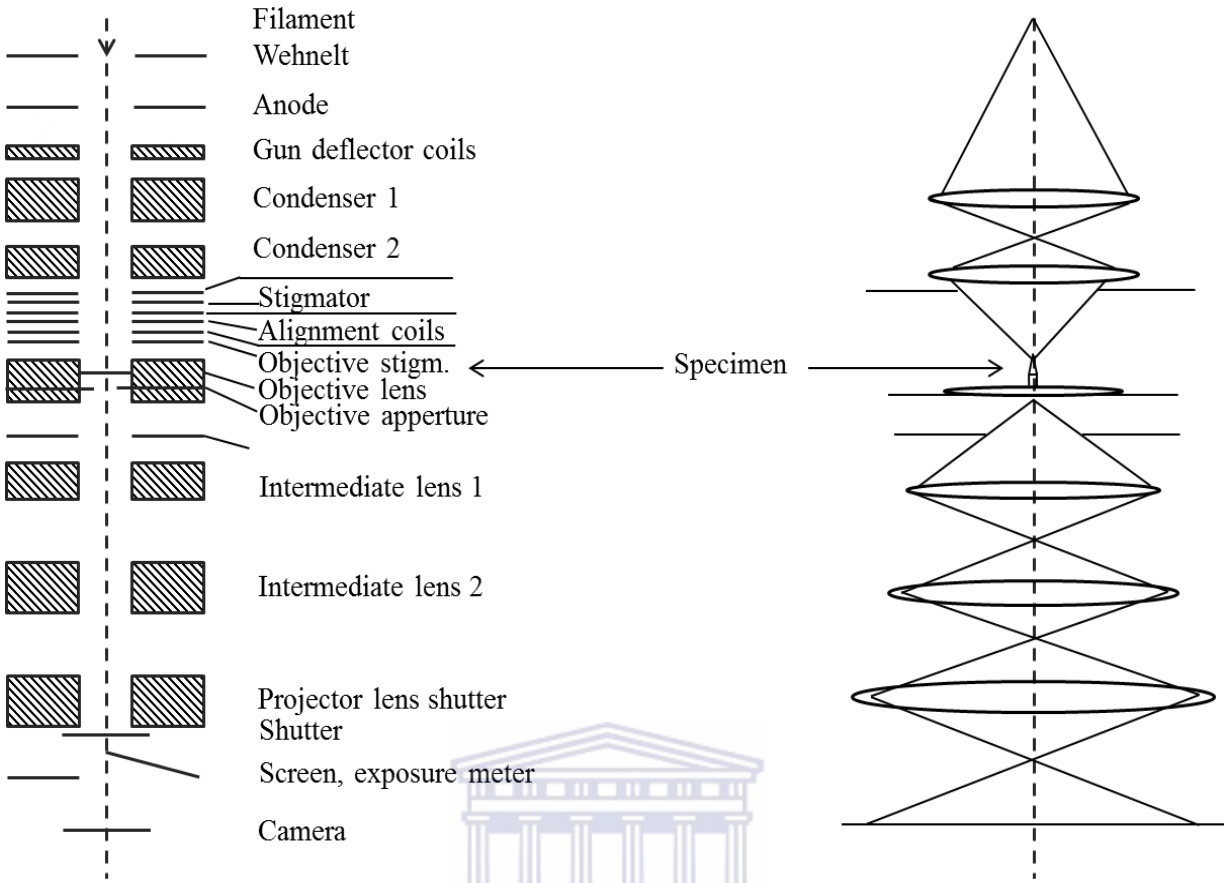

Figure 3.6: A cross-section of the basic components of a HRTEM.

The TEM used has, Scanning Transmission Electron Microscopy (STEM) capabilities. STEM is useful to determine whether the fine spots observed by TEM are indeed particles. In STEM the higher atomic number elements such as silver, will appear brighter, in comparison to TEM which shows the particles as dark spots [3.12].

3.4.2.5 Characteristic X-rays and Energy Dispersive Spectroscopy (EDS)

The Basic theory of EDS spectroscopy may be understood by considering the schematic structure of an atom, as illustrated by figure 3.12. The nucleus is surrounded by a series of ‘shells’, these shells are labelled as K.L,M.. etc. corresponding to their respective quantum numbers n=1,2,3. When the atom is exposed to an electron beam, one of the inner electrons (eg.an electron in the K shell) may be dislodged, leaving the atom in an excited state. The atom will then return to the ground state by filling the vacancy in the K shell, with one of the

electrons in the outer shells (eg. L or M shell). When the atom from the outer shell fills the inner shell, a loss of energy is observed, namely the difference in energy between the vacant K shell and the shell contributing the electron. This difference in energy is a discrete amount of energy characteristic of the atom and is emitted as an x-ray [3.12].

When an electron form the L shell fills a vacancy in the K shell, the resulting x-ray is known as K_α radiation and when electrons form the M shell fill a K shell vacancy a K_β x-ray is emitted. The same terminology applies for electrons that are dislodged from outer shells.

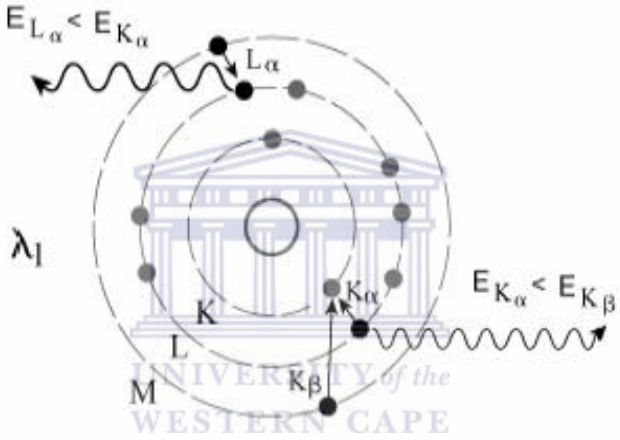

Figure 3.7: Schematic of the characteristic x-ray emission by an atom [3.12].

The basis for energy dispersive spectroscopy (EDS) is illustrated by the phenomenon observed in figure 3.12. The technique employs energy dispersion, which refers to the separation of x-rays according to their respective energies. Energy dispersion is accomplished with the aid of semiconductor detectors. When x-rays are incident on a given crystal, the electrons within the crystal will absorb an amount of energy and are hence excited, the relationship between the x-ray energy and the amount of excited electrons are directly proportional. The energy absorbed by the electrons are converted to electronic signals, the emitted signals are then amplified. The strength of the current produced (signal) is directly related to the energy of the x-ray. The amplified electronic signals generated by the

semiconductor are converted to digital form and fed into a multi-channel analyser (MCA). The signals are then sorted by the MCA, which essentially counts the amount of x-rays at each energy level incident on the crystal. The collected information is then displayed as a spectrum [3.12].

3.4.2.6 Sample preparation

HRTEM analysis of silver nanoparticles was performed on a Tecnai F20. The samples were prepared by dropping the silver nanoparticle suspensions on Formvar and lacey carbon copper grids and leaving it to dry for approximately 10 minutes with the aid of a light. The microscope was operated at 200 kV.

3.4.3 Scanning Electron Microscopy (SEM)

3.4.3.1Introduction

The scanning electron microscope (SEM) may be utilised to obtain structural information as well as elemental composition of a given specimen. The basic operation of a SEM is the heating of a cathode, which in turn produces electrons. Tungsten and Lanthanum hexaboride (LaB_6) filaments are most commonly used as an electron source due to their their relatively low work functions and high melting points [3.13].

The energy of the electrons produced range from a few hundred eV to 40keV. The beams of electrons are accelerated towards an anode with the aid of an applied voltage, and eventually make its way through an aperture in the anode into the vacuum chamber of the microscope. The condenser lens is the primary lens influencing the motion of the beam, as it passes through the pole piece. The beam is deflected by the condenser lens, resulting in the formation of a focused beam through the focal point situated above the condenser aperture [3.13].

Below the condenser aperture, divergence of the beam occurs once more, thus a final objective lens is introduced to focus the beam even further by converging it to a focal point at the surface of the specimen through an objective aperture. The surface of the specimen is then scanned by an electron beam with scanning coils. With the aid of positioning detectors and signals that are emitted can be utilized for the formation of an image of the scanned near-surface of the specimen. Figure 3.13 shows the schematic diagram of a SEM [3.13].

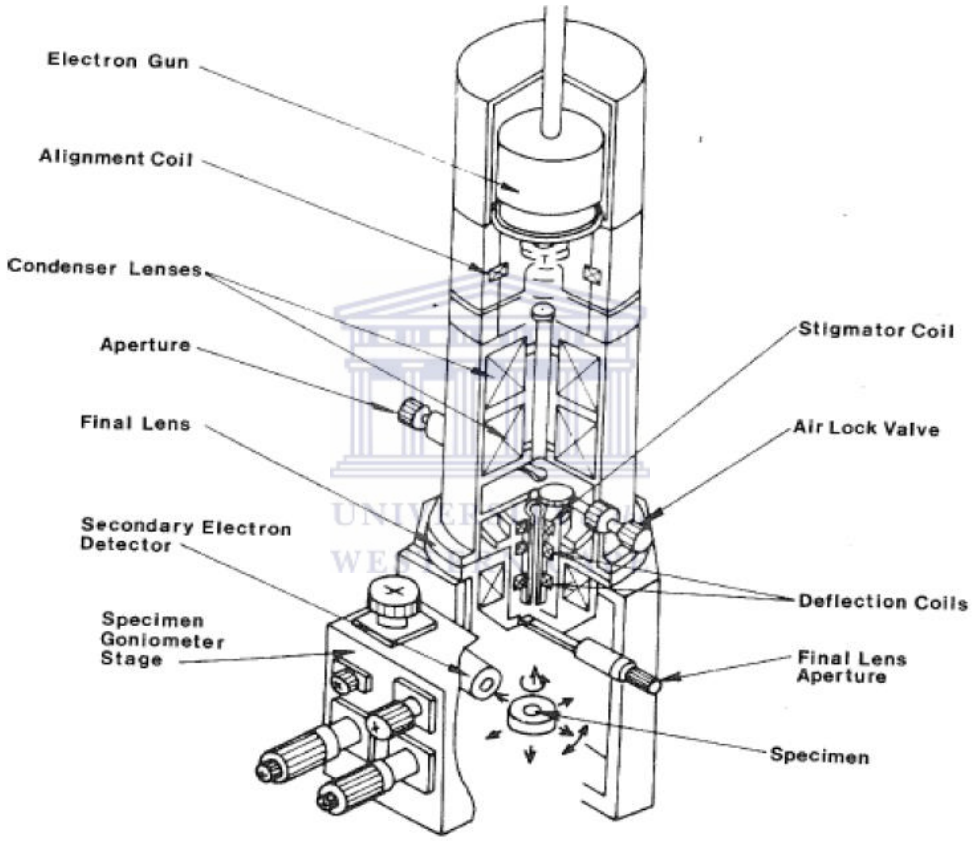

Figure 3.83: Schematic diagram of a typical SEM [3.5]

3.4.3.2 Resolution

The resolution of a microscope may be described as the smallest distance between two objects at which they appear as two separate entities, figure 3.12 shows the schematic diagram illustrating the concept of resolution [3.13].

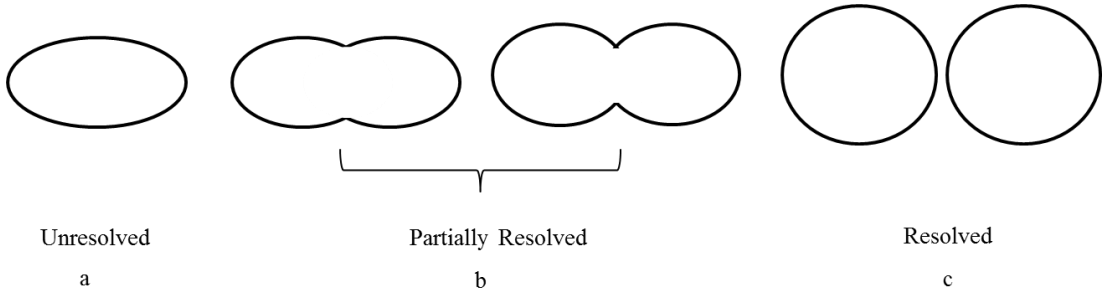

Figure 3.9: Schematic representation of the basic concept of resolution.

The concept of resolution can be understood by considering a vehicle approaching at night with its headlights on. When the vehicle is far away the lights of the car may appear as one light (figure 3.14(a)), however as the vehicle approaches the headlights become partially resolved as in the case of figure 3.14 (b). Once the vehicle is up close, the headlights of the vehicle appear as two separate headlights (figure3.14 (c)) [3.13].

The mathematical representation of the resolution (d_r) of a SEM is given by:

$$d_r = \frac{0.61\lambda}{n sin\alpha} \tag{3.16}$$

Where λ is the wavelength of the electron beam, n the index of refraction (usually n=1 for vacuum) and α, the aperture angle. In order to obtain a relatively good resolution, the aperture size may be decreased such that a more focused electron beam is obtained. The acceleration voltage may also be increased to obtain a smaller wavelength according to the De Broglie relation [3.13].

3.4.3.3 Depth of field and working distance.

The term depth of field refers to the extent that a specific area of a specimen appears to be in focus. The working distance (W_D) is defined as the distance between the uppermost section of the specimen and the final lens (objective lens), and may therefore be used to adjust the depth of field. An increase in the value of $W_{D,}$ results in a decrease in a decreased aperture

size, with a corresponding increase in the depth of field with a lower resolution. A greater working distance would therefore increase the aperture size and in turn decrease the depth of filed as illustrated by figure 3.15 [3.13].

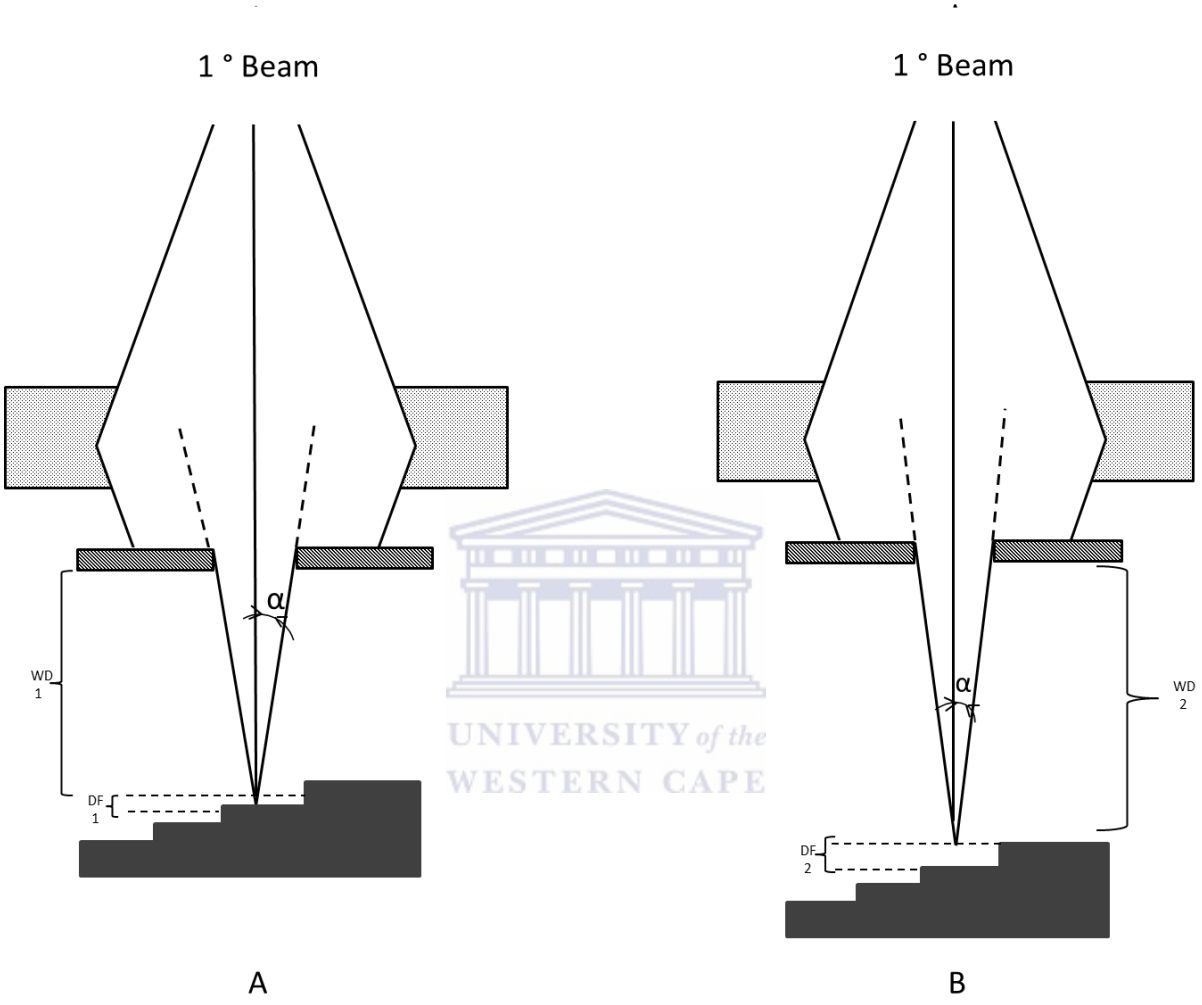

Figure 3.105: Schematic Diagram of the enhancement of the depth of field with ad increasing WD, (A) a short working distace (B) a larger WD, showing an increase in in the depth of field (DF).

3.4.3.4 Electron beam specimen interaction

When electrons interact with specimen atoms, they have a series of fates, each of which are dependent on the energy lost during the interaction. These signals include backscattered , secondary, transmitted electrons and specimen current. X-ray and auger electrons may also be

used to provide information about the composition of a specimen. Figure 3.16 illustrates the various electron beam specimen interaction produced in the SEM [3.13].

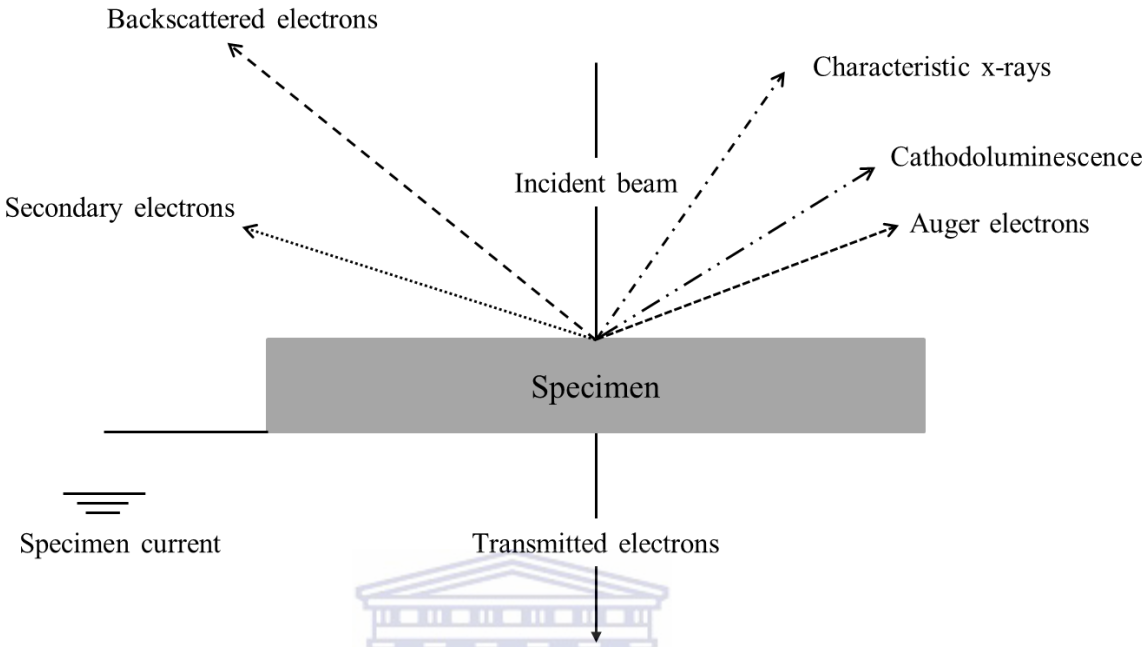

Figure 3.16: Schematic diagram illustrating the various signals obtained from beam specimen interaction in the SEM.

The electrons in the incident beam are scattered in the specimen in a shape similar to that of a pear, this pear shape is named the interaction volume, as represented by figure 3.17.

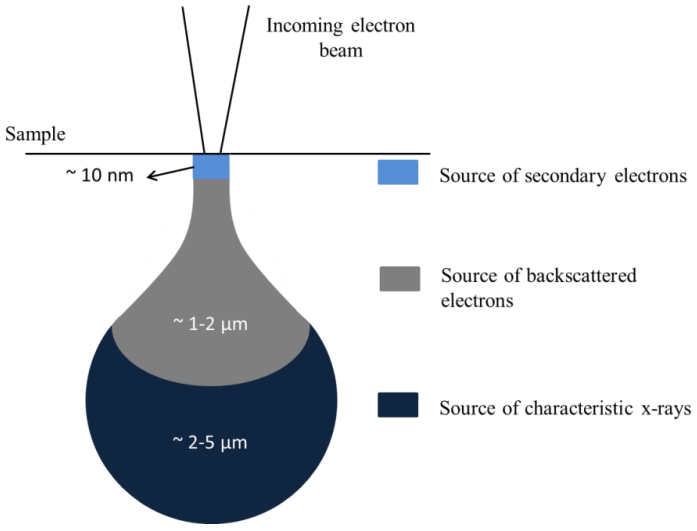

Figure 3.11: Schematic diagram of the interaction volume.

Signals are emitted from the interaction volume when the atoms in this volume are excited, and hence emit signals from different depths within the interaction volume. Depending on the nature and origin of the emitted signal, one could possibly obtain elemental and surface information of the specimen. Secondary electron, backscattered electrons, specimen current and transmitted signals provide information on the morphology of the sample, whilst elemental composition of the specimen may be obtained from characteristic X-ray, cathodoluminescence and auger electron signals [3.13].

3.4.3.5 Experimental set-up

SEM analysis of the silver nanoparticles and thin films was performed on an Auriga HRSEM at the Electron Microscopy Unit at the University of the Western Cape. The microscope was operated at 30 kV, 50 kV and 100 kV.

3.4.4 X-ray Diffraction (XRD)

3.4.4.1 Introduction

X-rays are short wavelength (high energy) electromagnetic radiation. The wavelengths are at the order of several angstroms (10^{-10}) corresponding to the interplanar distance within crystals. As a result, the x-rays may undergo diffraction in the crystal planes and hence be used to obtain structural information regarding the material [3.11].

An ideal crystal is that which consists of periodic array of atoms that forms planes. The electrons of these atoms are then accelerated upon the interaction with the electromagnetic (EM) wave; the electrons will oscillate at the same resonant frequency as that of the EM wave [3.11].

Constructive interference of the x-rays will occur only if the Bragg condition is satisfied, this process is known as x-ray diffraction. Each material poses a unique crystal structure arranged

in a periodic pattern in three dimensions, thus producing both quantitative and qualitative material analysis. In this study XRD will be used to identify the crystal structure as well as any phases that may have formed during the synthesis of silver nanoparticles [3.11].

3.4.4.2 Geometry of crystals

The periodic arrangement of atoms within a crystal material may be thought of as an array of imaginary points having fixed relation in space to the atoms of the crystal, rather than considering the actual atoms that the crystal is composed of. This array of imaginary points is known as a point lattice and is divided such that the surrounding of each points are identical, as shown in figure 3.18.

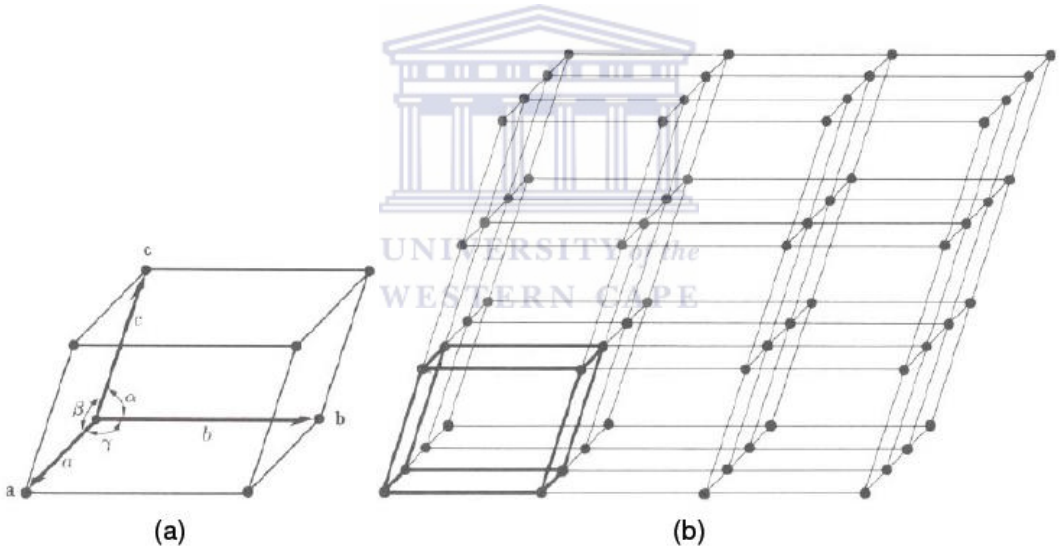

Figure 3.12: Schematic Diagram of (a) primitive cell and the angles between the translation vectors and (b) its point lattice [3.14].

The point lattice consist of three translational vectors $\vec{a}, \vec{b}$ *and* $\vec{c}$. Therefore any position in the lattice $\vec{r}$ may be represented as an integral multiple of the translation vectors given by:

$$\vec{r} = u\vec{a} + v\vec{b} + w\vec{c} \tag{3.17}$$

Where *u*, *v* and *w* are integers. The position vectors may be represented more compactly as [*u*,*v*,*w*] as indicated by figure 3.19.

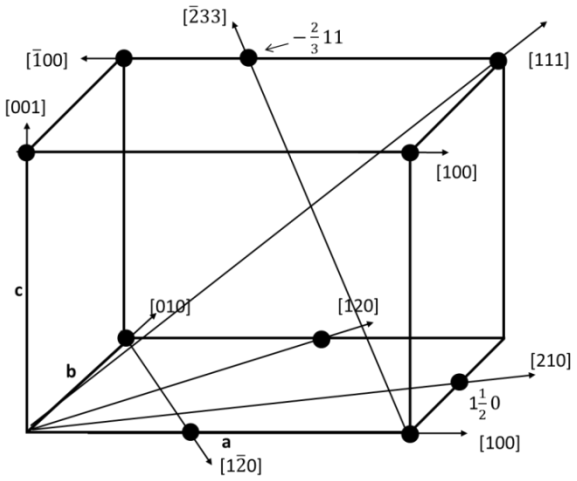

Figure 3.13: Schematic diagram showing indices of directions.

Regardless of the values *u*,*v w* they should slways be converted to the smallest set of integers, eg. [$\frac{1}{2}\ \frac{1}{2}1$], [112] and [224] all represent the same direction, however [112] id the preferred form. Negative indices are represented by a bar on top of the number eg. [$\bar{1}$12].

A point lattice group is a collection of symmetry operations, (eg. mirror and rotation reflections) which maintain fixed points. There are fourteen distinct lattice groups that remain unchanged when symmetry operations are performed, these lattices are known as Bravais Lattices [3.14].

There are seven crystal systems into which crystals may be classified into namely; triclinic, monoclinic, orthorhombic, cubic, tetragonal, hexagonal and trigonal. A cubic system will contain lattices: the simple cubic (sc), body centered cubic (bcc) and the face centered cubic (*fcc).* Table 3.5 shows a tabulated description of the 14 Bravais Lattices. The letters P, F and I represent primitive centering, face centered and body centered, whilst A, B and C represent base-centered cells centered on one pair of opposite faces A, B or C [3.14].

Table 3.5: Bravais Lattices and crystal systems.

System	Axial lengths and angles	Bravais Lattice	Lattice symbol
Cubic	Three equal axes at right angles $a = b = c, \alpha = \beta = \gamma = 90°$	Simple Body-centered Face-centered	P I F
Tetragonal	Three axes at right angles, two equal $a = b \neq c, \alpha = \beta = \gamma = 90°$	Simple Body-centered	P I
Orthorhombic	Three unequal axes at right angles $a \neq b \neq c, \alpha = \beta = \gamma = 90°$	Simple Body-centered Base-centered Face-centered	P I C F
Rhombohedral (Trigonal)	Three equal axes , equally inclined $a = b = c, \alpha = \beta = \gamma \neq 90°$	Simple	R
Hexagonal	Two coplanar axes at 120° , third axis at right angles $a = b \neq c, \alpha = \beta = 90°, \gamma = 120°$	Simple	P
Monoclinic	Three unequal axes, one pair not at right angles $a \neq b \neq c, \alpha = \gamma = 90° \neq \beta$	Simple Base – centered	P C
Triclinc	Three unequal axes , unequally inclined and non at right angles $a \neq b \neq c, \alpha \neq \gamma \neq \beta \neq 90°$	Simple	P

3.4.4.3 Bragg's description of X-ray diffraction

The crystal structure of materials is investigated by studying the diffraction of photons, electrons and neutrons. The diffraction mainly depends on the wavelength as well as the crystal structure. For optical wavelengths of a few thousand angstroms, the waves that are scattered elastically by the atoms of the crystal result in ordinary reflections [3.14]. However for optical wavelengths in the order of only several angstroms, such as that of X-rays, the direction of the diffracted beams differ significantly from that of the incident beams. W.L Bragg formulated a simple explanation of the diffracted beam of a crystal [3.15].

Consider a set of parallel planes, a distance *d* apart, that specularly reflect the incident x-rays elastically. Suppose two waves that are in phase are incident at an angle of θ_B to the parallel planes as shown in figure 3.20 [3.15].

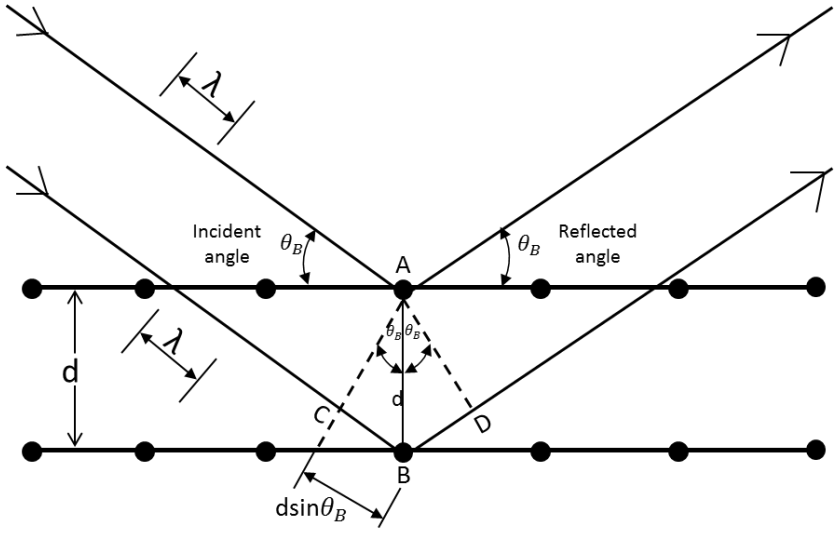

Figure 3.14: Schematic representation of the diffraction from a perfect crystal plane.

The path difference for waves that are reflected from adjacent crystal planes is $CB + BD = 2dsin\theta_B$ [3.15].

For constructive interference from adjacent planes to occur, the path difference must be equal to a whole number n of the wavelength (λ) [3.15]:

$$2dsin\theta_B = n\lambda \tag{3.18}$$

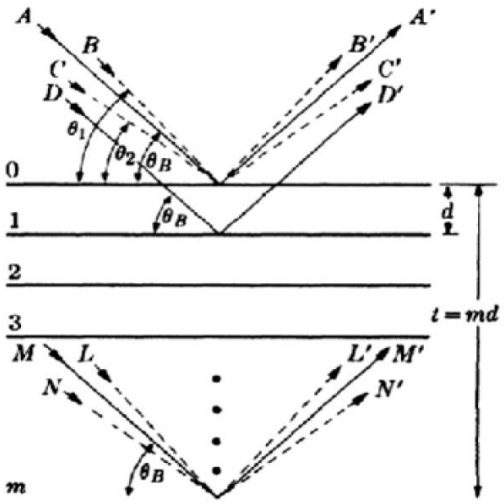

Figure 3.15: Effect of crystal size on diffraction [3.14].

Rays **A,D ..M** in figure 3.20 makes an angle of θ_B with the planes of diffraction. Destructive interference is not completed when the incident x-rays make Bragg angles that differ slightly from θ_B. hence ray **B**, makes a slightly larger angle of θ_1, so that ray **L**' from the *m*th plane below the surface is (*m+1*) wavelength out of phase with ray **B**', the ray from the surface plane, as a result the intensity of the of the beam diffracted at an angle of $2\theta_1$ is equal to zero. At angles of $2\theta_2$ the intensity is also equal to zero since θ_2 is such that ray **N'** from the *m*th plane below the surface is (m-1) wavelengths out of phase with ray C' from the plane surface. As a result, there are two limiting angles, $2\theta_1$ and $2\theta_2$ at which the intensity of diffraction must drop to zero. Consequently the diffracted intensity at angles near $2\theta_B$, but not less than $2\theta_2$ and greater than $2\theta_1$, is not equal to zero, but has intermediate values between the maximum intensity of the diffracted beam at $2\theta_B$ and zero. This phenomenon is shown in figure 3.21 [3.14].

Figure 3.22 (a), displays the curve of diffracted intensity vs. 2θ in contrast to that of figure 3.22 (b) which illustrates the hypothetical case of diffraction occurring only at the exact Bragg angle [3.14].

As the thickness of the crystal is reduced, the width of the diffraction curve illustrated in figure 3.22 (a) will increase. The width B, is usually measured in radians, at an intensity which is equal to half of the maximum intensity (FWHM). Therefore,

$$B = \frac{1}{2}(2\theta_1 - 2\theta_2) = \theta_1 - \theta_2 \tag{3.19}$$

The path difference of the two angles is related to the total thickness of the crystal by:

$$2tsin\theta_1 = (m+1)\lambda \tag{3.20}$$

$$2tsin\theta_2 = (m-1)\lambda \tag{3.21}$$

By subtraction, one obtains

$$t(\sin\theta_1 - \sin\theta_2) = 2tcos\left(\frac{\theta_1+\theta_2}{2}\right)sin\left(\frac{\theta_1-\theta_2}{2}\right) = \lambda \tag{3.22}$$

Since θ_1 and θ_2 are both relatively close to θ_B, its follows that:

$$\theta_1 + \theta_2 \cong 2\theta_B \tag{3.23}$$

And

$$\sin\left(\frac{\theta_1-\theta_2}{2}\right) \cong \frac{\theta_1-\theta_2}{2} \tag{3.24}$$

Therefore

$$2t\left(\frac{\theta_1-\theta_2}{2}\right)cos\theta_B = \lambda \Rightarrow t = \frac{\lambda}{Bcos\theta_B} \tag{3.25}$$

A more exact treatment of this problem yields

$$t = \frac{0.9\lambda}{Bcos\theta_B} \tag{3.26}$$

The above relation is known as the Scherrer Formula, and is used to estimate the crystal size of very small crystals, by measuring the width of their diffraction curves [3.14].

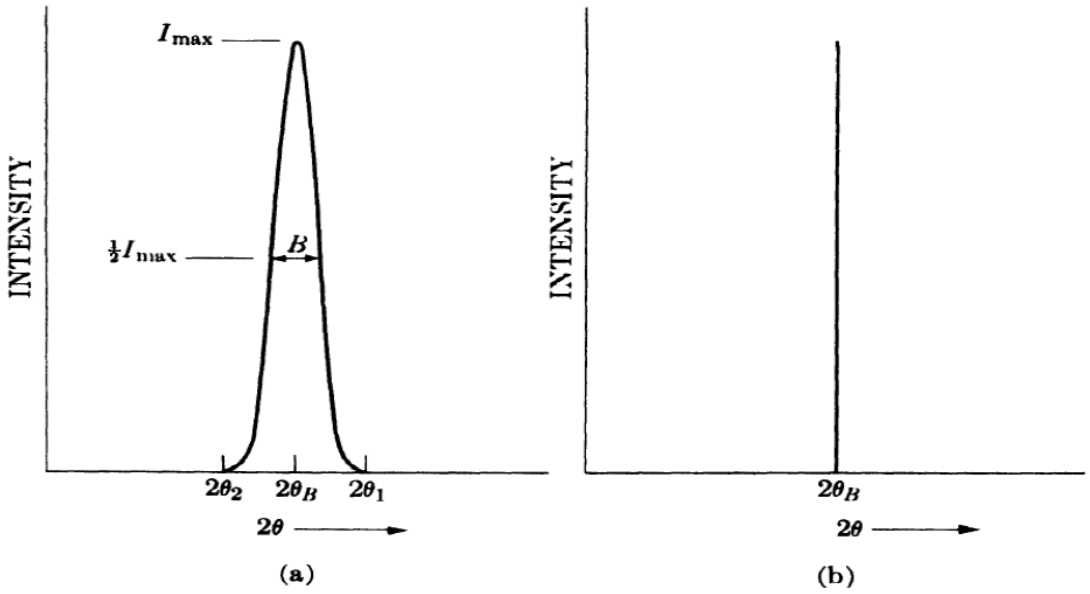

Figure 3.16: Schematic illustration of the effect of fine crystalline sizes on diffraction curves [3.14].

3.4.4.4 The X-Ray Diffractometer

The X-ray diffractometer is the instrument used to study the crystal structure of a material by measuring the intensity of the diffracted beam with an electronic counter. The diffractometer utilizes monochromatic x-rays produced at point S, whilst the x-ray detector is placed on the circumference of the circle at G, with the powdered samples at the centre of the circle at point C. The divergent x-rays originated from point S, hit the specimen and are diffracted such that it forms a convergent diffracted beam. This beam will then come to a focus at the slit F, and enters the counter G, slits A and B are used to define as well as collimate the incident and diffracted beam respectively [3.14].

The sample at point C, is supported on top a of a table H. This table rotates about an axis O, which is situated such that it is placed perpendicular to the drawing. The focal spot on the target of the x-ray tube is shown at point T, on figure 3.23.

The counter and the receiving slits are supported by the carriage at point E, which may be rotated about the axis O. The angular position 2θ of the carriage may be read on the graduating scale K.E and H are coupled mechanically such that the rotation of the counter through 2θ degrees is automatically causes rotation of the specimen C, through θ degrees. This setup preserves the focusing condition of the instrument [3.14].

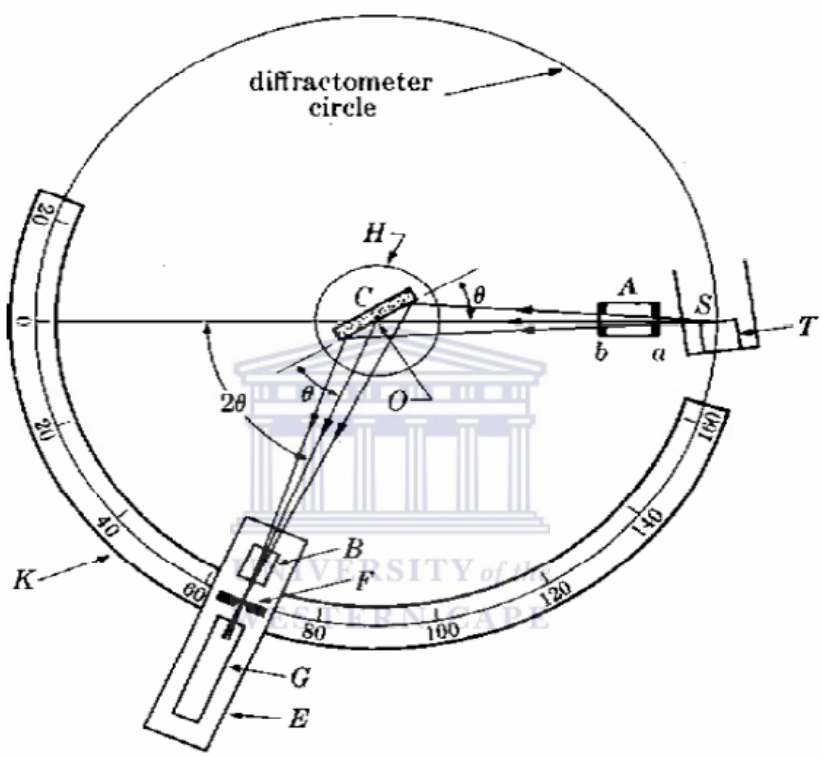

Figure 3.17: Schematic illustration of an x-ray diffractometer [3.14].

3.4.4.5 The Laue equations

The Laue equations provide a unique geometrical description for the diffraction of crystal planes. Figure 3.24 shows that the scattered wave vector ($\vec{k'}$) is obtained by bthe addition of the scattering vector $\Delta\vec{k}$ and the incident wave vector $\vec{k}$. $\Delta\vec{k}$ is defined as the change in wave vector upon scattering. The scattered wave vector lies in the reciprocal space, an abstract

mathematical concept in which distances are inversed to that of the real space and x-ray diffraction is described by Fourier analysis [3.15].

The Laue equations are therefore obtained by considering the orthogonal relationships between the crystal lattice vectors and the scattering vector, as well as the condition that the resultant of the incident and diffracted waves must be a point in reciprocal space [3.15].

$$\vec{a} \cdot \overrightarrow{\Delta k} = 2\pi h, \vec{b} \cdot \overrightarrow{\Delta k} = 2\pi k \text{ and } \vec{c} \cdot \overrightarrow{\Delta k} = 2\pi l$$

where the integers *h, k,* and *l* are the indices of the Bragg plane responsible for the diffraction. In order for diffraction to occur these equations need to be satisfied simultaneously.

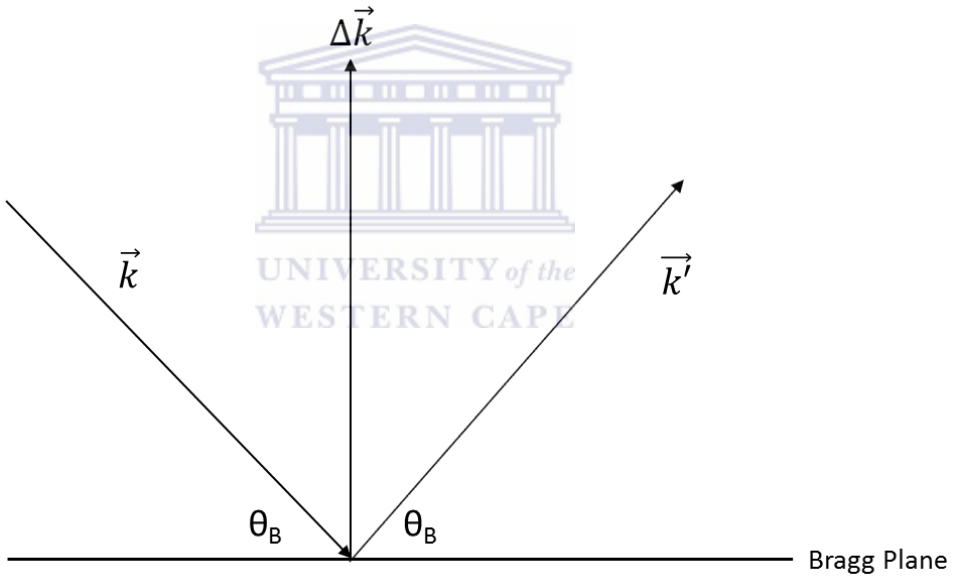

Figure 3.18: Schematic diagram showing the definition of the scattering vector $\overrightarrow{\Delta \boldsymbol{k}}$ ($\overrightarrow{\Delta \boldsymbol{k}} = \overrightarrow{\boldsymbol{k'}} - \vec{\boldsymbol{k}}$) as well as the Bragg plane and diffraction during x-ray diffraction**.**

3.4.4.6 Experimental set-up

XRD data was collected with a Bruker AXS DS Advance diffractometer, with 2θ values ranging from 20-90°, with a step size of 0.028° operating at 45 kV and 40mA at Ithemba Labs Cape Town. Monochromatic Copper (Cu) $K\alpha_1$ radiation with a wavelength of 0.154 nm was used as the X-ray source.

3.4.5 Thermogravimetric Analysis (TGA)

3.4.5.1 Introduction

Thermogravimetric analysis is an analytical technique, used to provide information about the thermal properties of a given material. The technique monitors the mass of a given sample as function of temperature, whilst the specimen is subjected to a relatively controlled temperature program in a controlled atmosphere. All compounds will have a characteristic TGA curve, since each compound has a unique sequence of physicochemical reactions that will occur over a definite range of temperatures at rates which are dependent on the molecular structure. The variation in the weight observed occurs due to the separation or the formation of different chemical and physical bonds at elevated temperatures that result in the development of unstable products or the formation of reaction products that are heavier. This information may therefore provide useful information regarding the thermodynamics and kinetics of various chemical reactions, reaction mechanisms, and the intermediate and final products [3.13].

3.4.5.2 The instrument

The TGA instrument consists of 5 key components, namely the microbalance, furnace, programmer controller, and a computer or data acquisition system. The sample is continually weighed by the microbalance as it is heated to elevated temperatures. The samples are placed in a shallow crucible, which is attached to the microbalance. The balance is an automatic-recording balance, which detects the deviation of the mass of the sample. A set of photocells are connected to the arm of the balance and a lamp. If any changes occur in the weight of the sample, the balance will rotate, and move a flag so that light incident on each photocell is no longer equal. The signal is then amplified and fed back as a current to a torque motor in order to restore the balance. The current produced is proportional to the change in weight

and is recorded on the y axis of the recorder. The sample is held in a crucible, situated inside the furnace of the detector. The temperature change in the furnace is continuously measured with the aid of a thermocouple; this signal is then recorded on the x axis. The most common heating rates are from 5-10°/min. The sample is exposed to a non-interactive atmosphere in order to standardize the conditions of the experiment without affecting the sample. Common gases employed the analysis of TGA include air, Ar, Cl_2, CO_2, H_2, HCN, H_2O, He, N_2, O2 and SO_2 [3.16] .Figure 3.25 shows the schematic diagram of the set-up of a TGA instrument.

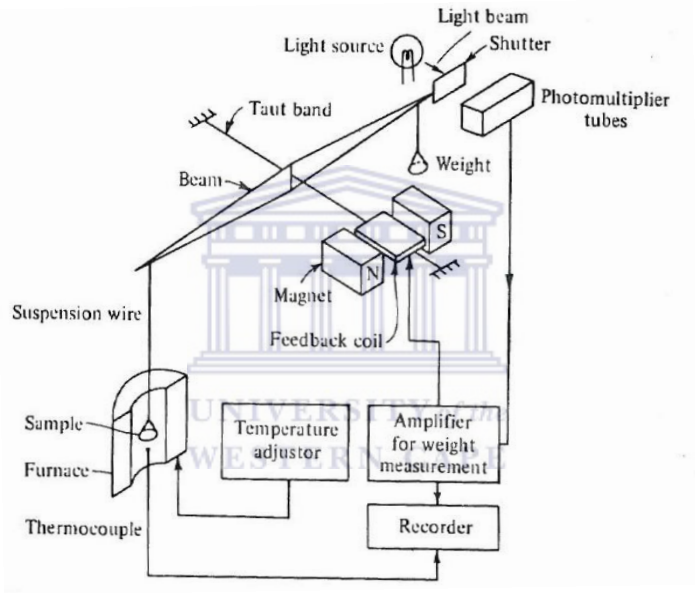

Figure 3.195: Schematic of the TGA instrument [3.16].

3.4.5.3 Experimental set-up

TGA of silver nanoparticles was performed using a Perkin Elma STA 6000, a mass of approximately 17mg of PVP protected silver nanoparticles was used to perform the analysis. The non-interactive gas employed was argon in a temperature range of 30-600° C at a rate of 10°/min. The measurement was performed at the South African Institute for Advanced Materials Chemistry (SAIAMC) at UWC.

3.5 References

[3.1] Carotenuto. G, Pepe. G. P, and Nicolais. L, *Eur. Phys. J. B*, 17, p 11 (2000)

[3.2] Kellner. R, "Analytical chemistry: the authentic text to the FECS curriculum analytical" chemistry, *Weinheim: Wiley VCH* (1998)

[3.3] Marczenko. Z, and Balcerak, M "Separation Preconcentration and Spectrophotometry in Inorganic Analysis", *Amsterdam: Elsevier Science B.V,* (2000)

[3.4] Gasaymeh. S,Radiman. S, Heng. L, Saion. E, Mohamed Saeed. G, *Am. J. Applied Sci.,* **7**, p 892 (2010)

[3.5] Nalwa. H, "Handbook of Thin Films Materials", *Academic Press*, **5**, p 61 (2002)

[3.6] Monticone S, Tufeu. R, Kanaev. A, *J. Phys. Chem. B*,**102,** p 2854 (1998)

[3.7] Reda. S, Al-Ghannam. S, *AMPC*, **2**, p 75 (2012)

[3.8] Bass. M, Van Stryland. E, and Williams. D "Handbook of Optics", *New York: McGraw-Hill,* 2nd edition (1995)

[3.9] Ulery. A and Drees. L "Methods of Soil Analysis", *Madison: Soil Science Society of America* (2008)

[3.10] Theophanides. T "Infrared Spectroscopy Materials Science Engineering and Technology", *InTech* (2012)

[3.11] Chescoe. D, and Goodhew. P "The operation of the transmission electron microscope", *New York: Oxford University Press,* (1984)

[3.12] Goodhew. P, Humphreys. J, and Beanland. R "Electron Microscopy and Analysis", 3rd edition, *New York: Taylor and Francis,* (2001)

[3.13] Postek. M, Howard. K, Johnson. H and McMichael. K , "Scanning Electron Microscopy- A students handbook", *Vermont: Ladd Research Industries* (1980)

[3.14] Cullity. B, "Elements of X-ray Diffraction", 2nd edition , *USA: Addison Wesley Publishing Company Inc.* (1978)

[3.15] Kittel. C, " Introduction to Solid State Physics", 8th edition, *USA: John Wiley and Sons* (2005)

[3.16] Willard. H, Merrit. L, Dean. J, and Settle. F "Instrumental Methods of Analysis", 6th edition, *New York: D. Van Nostrad Company* (1981)

CHAPTER 4

Synthesis and Characterization of Silver Nanoparticles

4.1 Introduction

Various synthesis methods have been employed to produce silver nanoparticles with varying morphologies, such as photochemical reduction [4.1], microwave irradiation [4.2], electrochemical synthesis [4.3] and atomic beam sputtering [4.4]. Most of these synthetic routes involve 2-step processes and may produce hazardous chemicals in some instances. However, these methods may also be relatively complex and costly [4.5].

The polyol synthesis is a cost effective, simple one-step, environmentally friendly synthesis technique to produce silver nanoparticles of various morphologies. This process involves the dissolution of silver nitrate in the presence of a reducing agent and stabilizer, which is used to prevent agglomeration of the particles [4.6]. Although this process generally produces nanoparticles that are non-uniformly distributed, it is cost effective and simple.

The properties of the silver nanoparticles are highly dependent on the morphology of the particles, hence control over the synthesis conditions are required such that uniform size and shaped particles are obtained by the polyol synthesis. Parameters such as temperature, reaction time, stabilizer/ surfactant concentration, and types of surfactant are among the factors that determine the distribution, shape and size of the nanoparticles. Hence, this chapter provides insight into the effect that reaction time, temperature, stabilizer/ surfactant concentration, solvent, and surfactant has on the formation and properties of the silver

nanoparticles by analysing results obtained from HRTEM, HRSEM, UV-VIS, XRD, and TGA techniques.

4.2 Silver nanoparticle formation and characterization

Silver nanoparticle suspensions were prepared by a modified polyol synthesis in the presence of PVP as a stabilizer, as described by Carotenuto et al [4.6]. A detailed procedure of the synthesis of the silver nanoparticles is provided in Section 3.2 of Chapter 3.

PVP is a non-ionic surfactant and hence protects the silver nanoparticles sterically. The donated lone pairs of the oxygen and nitrogen atoms found in the polar groups of PVP, occupy two *sp* orbitals of the silver ions, hence forming a complex compound. The particles were protected by the PVP due to the formation of coordinate bonds between the silver ions and the nitrogen and oxygen present in the polymer. This coordinate bond leads to the formation of a covering layer across the surface of the silver nanoparticles. The reaction between silver and PVP is shown in equation (4.1) [4.7, 4.8, 4.9,].

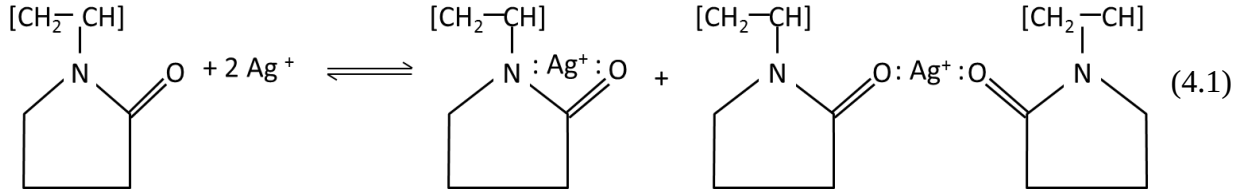

(4.1)

UV-VIS is one of the most important characterization tools to analyse silver nanoparticles. Due to surface plasmon resonance, silver nanoparticles give rise to a characteristic plasmon peak at ~420 nm in the UV-VIS spectrum.

Figure 4.1 shows the UV-VIS spectrum of the prepared silver nanoparticle suspension. The presence of a characteristic plasmon peak at approximately 420 nm, confirmed the presence of silver nanoparticles [4.10]. The peak arises due to the collective oscillations of the conduction electrons of the silver nanoparticles, upon their interaction with electromagnetic

(EM) radiation. An overview of the origin of the plasmon resonance of noble metal nanoparticles was presented in Section 2.2.

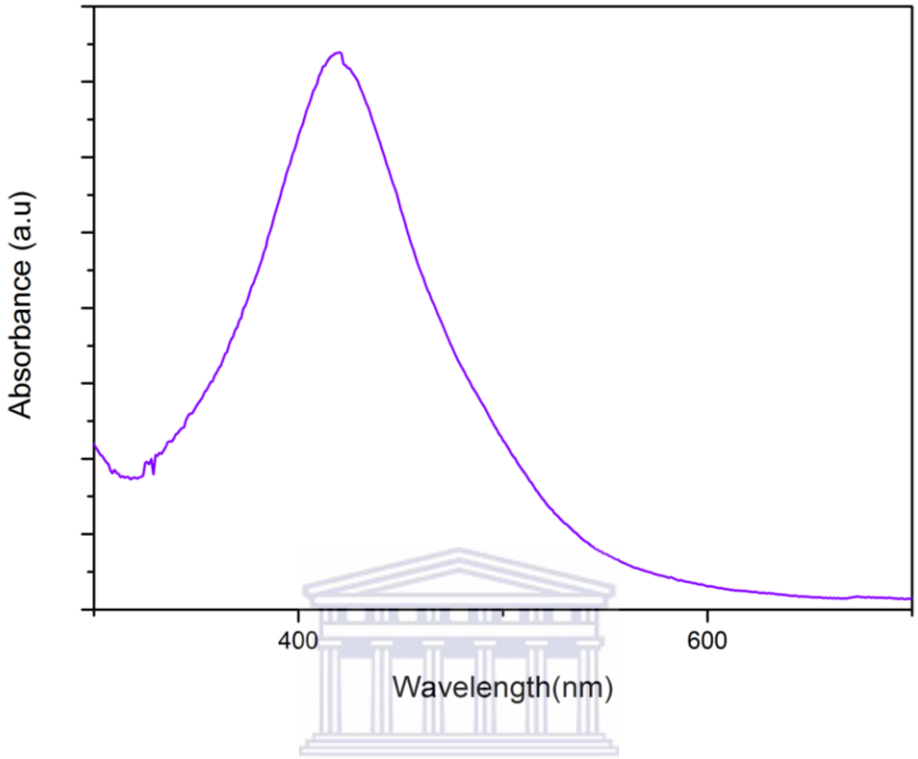

Figure 4.1: UV-VIS spectrum of a silver nanoparticle suspension.

An increase in the absorbance of the plasmon peak corresponds to an increased concentration of silver nanoparticles [4.10], since increased amounts of EM radiation is absorbed by a more concentrated suspension. As mentioned in Section 3.4.1.2, this observation stems from the Beer-Lambert law (equation 3.3) which shows the linear relationship between absorbance and the concentration of the suspension [4.11].

The degree of dispersion of the nanoparticles in the suspension, concentration and size of the nanoparticles are primarily, depicted by the UV-VIS spectrum of the suspension. The full width half maximum (FWHM) of the plasmon resonance peak can predict the dispersion of the particles; a broader peak corresponds to a non-uniform distribution of the nanoparticles, whilst a narrower peak may correspond to a more uniform distribution, thus revealing information about the degree of agglomeration of the particles[4.10, 4.12, 4.13]. These

results may be obtained by applying a Gaussian fit to the UV-VIS spectrum of the silver nanoparticles. The FWHM of the plasmon resonance peak illustrated in Figure 4.1 was measured to be 82.2 nm. Changes in this value would provide an indication of how the dispersion of the silver nanoparticles is affected when reaction parameters are varied, these values vary significantly in literature [4.10, 4.12, 4.13].

HRTEM analyses of the silver nanoparticle suspensions revealed information about the size and morphology of the silver nanoparticles, whilst EDS analysis confirmed the presence of silver (Figure 4.2 (c) inset). HRTEM micrographs showed the presence of various shapes (Figure 4.2). The sizes of the spherical silver nanoparticles illustrated in Figure 4.2 (a), ranged from 2 nm to 60 nm, whilst the sheet like structures exhibited in Figure 4.2 (b and c), ranged from 500 nm to 3 μm. Similar sheet like structures as that shown in Figure 11 (b) has been observed by Du et al. However, instead of PVP, ammonia was used to produce these structures [4.14]. Hence, confirming that PVP may also be incorporated to produce these structures.

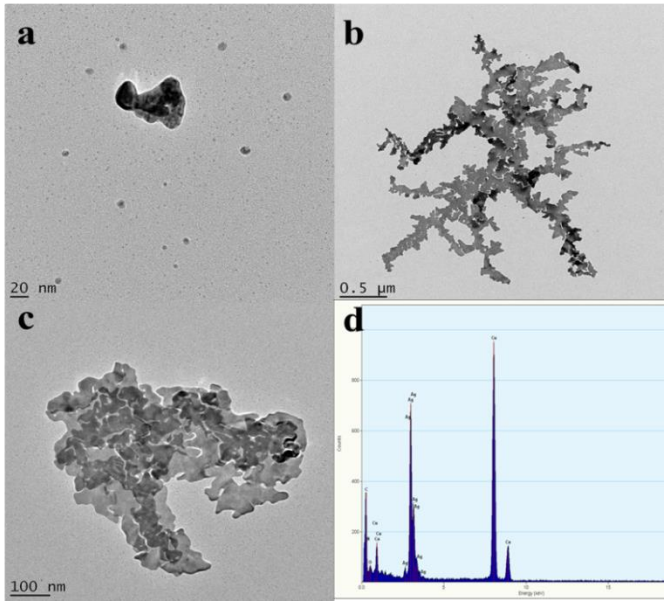

Figure 4.2: HRTEM micrographs of the silver nanoparticle suspension (a) small spherical particles and agglomerated particles, (b) sheet like structure with surrounding small particles (c) large sheet like structures and (d) the EDS spectrum of the structure exhibited in the micrograph, confirming that the structures are all silver.

HRTEM analyses of the silver nanoparticles showed that various structures were produced using the polyol synthesis. The Selected Area Electron Diffraction (SAED) pattern of the silver nanoparticles presented in Figure 4.2 (a) exhibit concentric rings (Figure 4.3), with intermittent bright spots, indicative of the polycrystalline nature of the silver nanoparticles. The rings may be indexed on the basis of the face-centered cubic (*fcc*) crystal structure of silver, as (111), (200), (220), (311) and (222) [4.15, 4.16, 4.17].

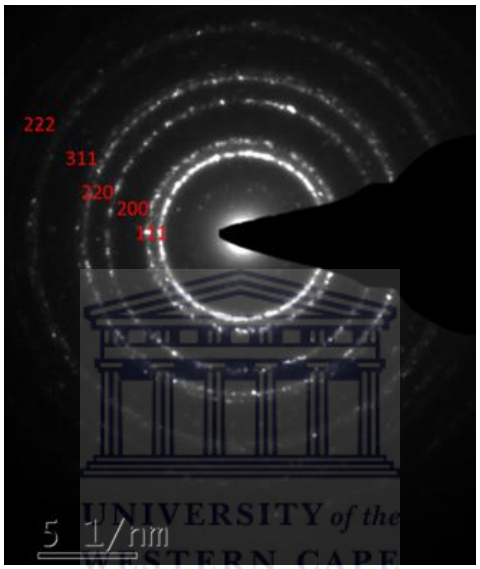

Figure 4.3: SAED pattern of the silver nanoparticles presented in Figure 4.2 (a).

The polycrystalline nature of the silver nanoparticles, may be confirmed by considering the X-ray Diffraction (XRD) analysis of the silver nanoparticles.

XRD studies of silver nanoparticles

From X-Ray diffraction analysis one can obtain information about the crystal structure and the crystallite size of the nanoparticles by means of the Debye-Sherrer equation. The XRD spectrum of the prepared silver nanoparticles is shown in Figure 4.4.

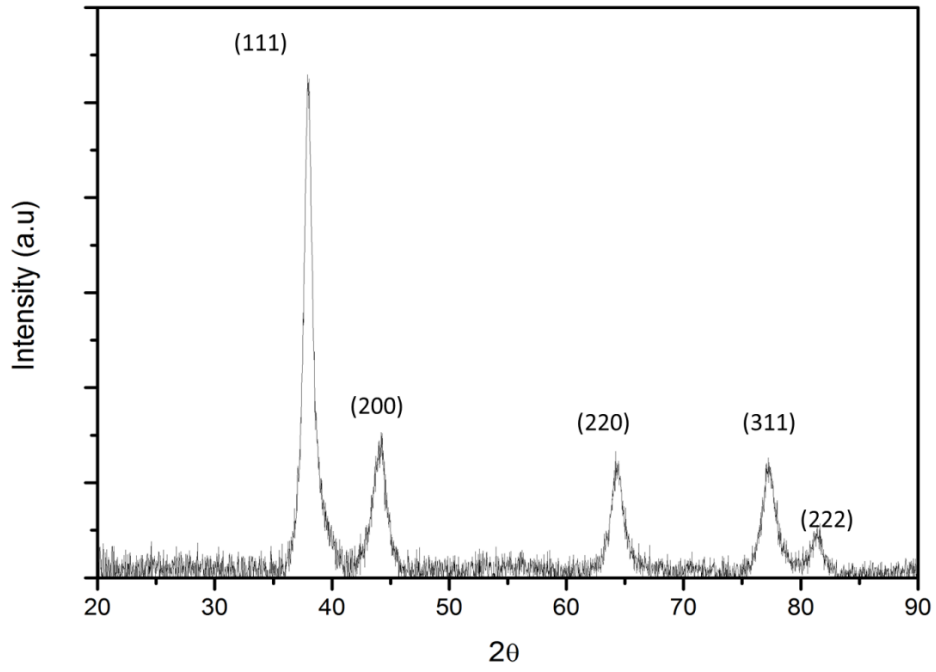

Figure 4.4: XRD spectrum of silver nanoparticles.

The XRD spectrum displayed in Figure 4.4 shows five peaks positioned at 2θ values of 37.89°, 44.21°, 64.30°, 77.34° and 81.39° corresponding to (111), (200), (220), (311) and (222) *fcc* planes of silver, respectively [4.6, 4.18]. The lattice constant (*a*) was determined from the (111) peak (Section 3.4.2 equation (3.11)) , and measured to be 4.1Å. These values are well in agreement with the Joint Committee on Powder Diffraction Standards (JCPDS) No. 04-0783.

The intensity of the (111) facets are much stronger than that of the other facets observed in the XRD spectrum, suggesting that the crystals are mainly dominated by the (111) facets, hence the crystal growth of the silver stuctures are preferentially oriented along the [111] direction. Similar results have been observed by Swarnavalli et al [4.14, 4.19].

The crystallite size of the nanoparticles, *t* were obtained by means of the Debye-Scherrer equation:

$$t = \frac{k\lambda}{\beta_{\frac{1}{2}} cos\theta}, \tag{4.2}$$

where *k* is a constant (*k=0.89*), and λ= 1.54060 Å is the $CuK_{\alpha 1}$ wavelength, and $\beta_{\frac{1}{2}}$ the full width half maximum (FWHM) of the peak at 2θ. By considering the FWHM of the (111) direction in the XRD spectrum, a value of d = 1.48 nm was measured. Since the crystallite size measured by XRD is smaller than the size of the silver nanoparticles obtained from HRTEM (Figure 4.2 (a)) , it confirms that the prepared silver structures were polycrystalline [4.20]. Sun et al prepared silver nanoparticles of various morphologies and observed that spherical shaped silver nanoparticles were polycrystalline. They had also observed that the crystallite size determined using the XRD spectra was smaller than the size of the silver nanoparticles observed by HRTEM. This had confirmed the polycrystalline nature of the produced spherical silver nanoparticles, hence our results are in agreement with that of Sun et al [4.21].

TGA results of silver nanoparticles

Thermogravimetric analysis (TGA) was performed on the silver nanoparticles in order to investigate at what temperature the polymer (PVP) would decompose. Figure 4.5 shows the TGA thermogram of PVP-stabilized silver nanoparticles.

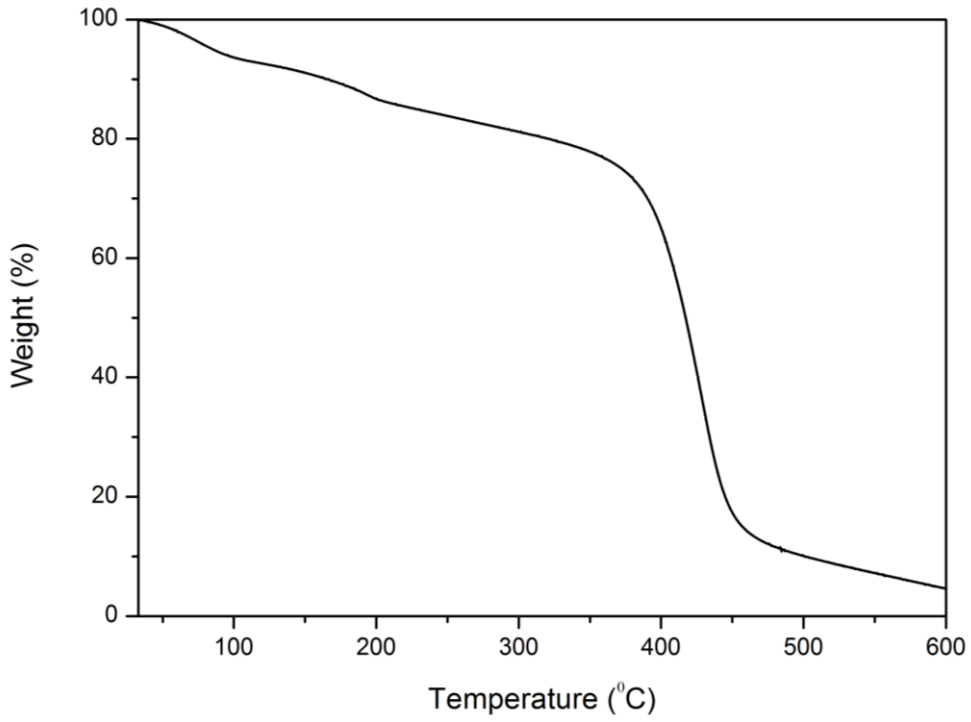

Figure 4.5: TGA thermogram of PVP stabilized silver nanoparticle. Showing a gradual weight loss from 30^0 C - 600^0 C.

The analysis was performed on a Perkin Elma STA 6000, from room temperature to 600° C, with a heating rate of 10° C/min. The weight loss observed from 30- 100° C may be due to the evaporation of any excess solvent and moisture that was still present in the powder, whilst the weight loss up to 200° C could be attributed to the melting point of the PVP, which ranges between 150-180°C. In the range of 100-200° C the low molecular weight oligomers of the PVP is evaporated, and is insuffficent to melt the molten PVP. However significant weight loss is observed from approximately 350-500° C, this weightloss corresponds to the structural decomposition of the PVP [4.6, 4.22].

Around 600^0 C, some material is still present as shown in the thermogram (Figure 4.5), suggesting that the remaining material has a relatively high melting point, which may be due to the silver. Similar results have been observed by Gasameh et al [4.22].

From the results obtained, it is evident that silver nanoparticles may be produced by the polyol synthesis, and optimization of the synthesis is required. Therefore the effect of

reaction time, temperature, surfactant concentration and solvent was investigated in order to gain further insight into nanoparticle formation and growth.

4.3 Effect of reaction time at room temperature.

In order to investigate the effect of reaction time on the formation of the silver nanoparticles, $AgNO_3$ and PVP was dissolved in ethanol at room temperature and stirred with a magnetic stirrer (the details of the reaction is provided in Section 3.2.1) . UV-VIS and HRTEM was used to structurally characterize the silver nanoparticles.

4.3.1 Optical properties of silver nanoparticles prepared at room temperature at various reaction times.

The UV-VIS spectra of the silver nanoparticle suspensions taken at various reaction times ranging from 1 hour to 6 days, are displayed in Figure 4.6.

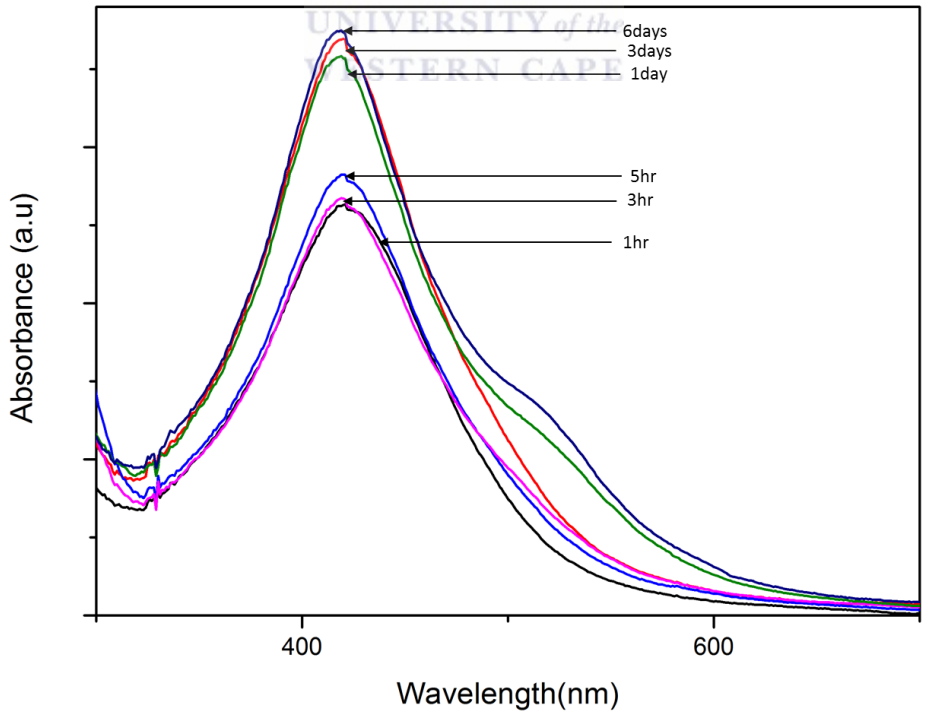

Figure 4.6: UV-VIS spectrum of silver nanoparticle suspensions prepared at room temperature at increasing time intervals

As the reaction time increased, an increase in the absorption peak height was observed. This indicates that more silver nanoparticles were produced with an increased reaction time [4.10]. Slistan-Grijalva et al, obtained similar results [4.23].

Table 4.1: FWHM and plasmon peak data of suspensions prepared at room temperature at various reaction times.

Time	FWHM (nm)	Plasmon Peak (nm)
1 hr	83.4	421.3
3 hrs	81.5	421.2
5 hrs	79.5	421.0
1 day	78.5	419.7
3 days	82.7	419.7
6 days	76.1	419.9

Table 4.1, shows the FWHM and corresponding plasmon peaks of suspensions prepared at various reaction times, obtained from the UV-VIS spectrum in Figure 4.6. As the reaction proceeded from 1hr – 1 day the FWHM decreased, thus indicating that the particles became more uniform and that the particles were not aggregating [4.10, 4.12**].** The positions of the plasmon peaks remained more or less constant throughout the entire time period, indicating that the overall size of the particles remained roughly the same as no red shifts or blue shifts were observed [4.24]. As the reaction began to proceed to 3 days, an increase in the FWHM was observed, indicating that agglomeration of the particles was taking place [4.12, 4.13]. However, as the reaction progressed to 6 days the FWHM decreased once again. During the 6 days of the experiment, the temperature in the room varied and hence could be a possible reason for the variation in the FWHM.

For reaction times of 1 and 6 days, quadrupole resonance peaks were observed. These peaks occur due to non-uniform incident electromagnetic radiation across the particles, suggesting that the various particles in the suspensions have a different oscillation pattern to that of the

primary dipole [4.25]. This phenomenon occurs when the size of the nanoparticles in the suspension varies, such that the electron oscillation of the particles are no longer uniform. For larger particles the charges are essentially spread over a larger surface area, thus producing an oscillation at greater wavelengths [4.24]. This suggested that particles with various shapes and sizes were produced.

4.3.2HRTEM analysis of silver nanoparticles prepared at room temperature at various reaction times.

The HRTEM micrographs of the nanoparticles suspensions at various times are displayed in Figure 4.7.

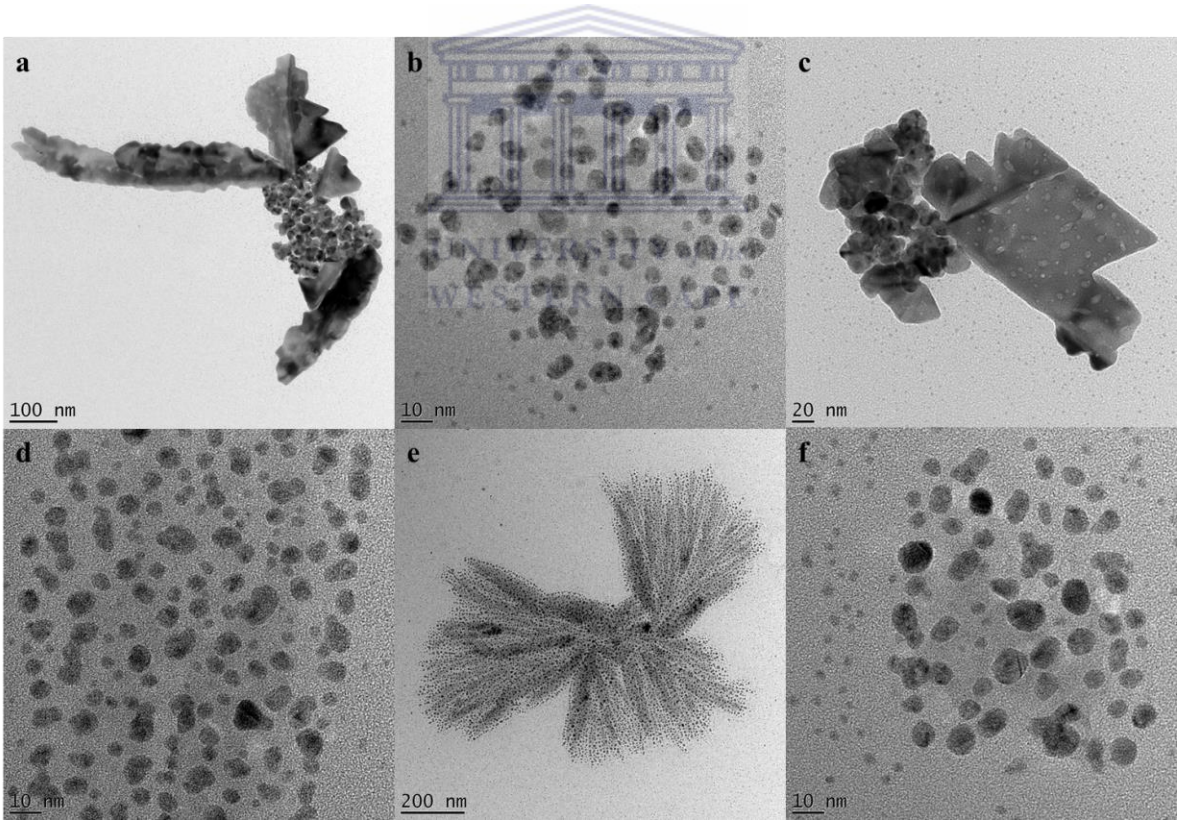

Figure 4.7: HRTEM micrographs of silver nanoparticles prepared at various reaction times (a and b) after 1 hour of stirring, (c and d) after 5 hours of reaction time, and (d and e) after 6 days of stirring.

HRTEM micrographs showed that the particles decrease in size as the reaction proceeded. An increase in the concentration of the particles is also observed, corresponding to the results obtained by the UV-VIS spectrum (Figure 4.6). The sizes of the silver nanoparticles prepared at 1 hour, 5 hour, and 6 days was measured to be 3.58 ±1.85, 6.02 ± 2.22, and 4.91±1.85 nm. The error associated with the sizes of the silver nanoparticles suggests that the particles remained roughly the same. In addition, HRTEM analysis of the nanoparticles only makes use of one drop of the suspension, hence only providing an indication of the morphology of the nanoparticles produced within the one drop used during sample preparation for HRTEM analysis.

Since a reaction time of 6 days is a relatively long period, temperature was introduced to the experiment in order to investigate whether it may decrease the overall reaction time.

4.4 Effect of temperature: room temperature vs. 80^0 C.

In order to investigate whether an increase in the reaction temperature will yield a shorter reaction time and perhaps a decrease and more uniform particle distribution, a silver nanoparticle suspension was synthesised by refluxing $AgNO_3$ in a solution of PVP and ethanol. Section 3.2.2 provides the details of the synthesis.

4.4.1 Optical properties of silver nanoparticles prepared at room temperature and 80 ^{0}C.

Figure 4.8 shows the UV-VIS spectra of suspensions prepared at room temperature and at a reflux temperature of 80^0 C. The suspensions were magnetically stirred for 1 day, the reaction time and concentration of PVP and $AgNO_3$ was kept constant.

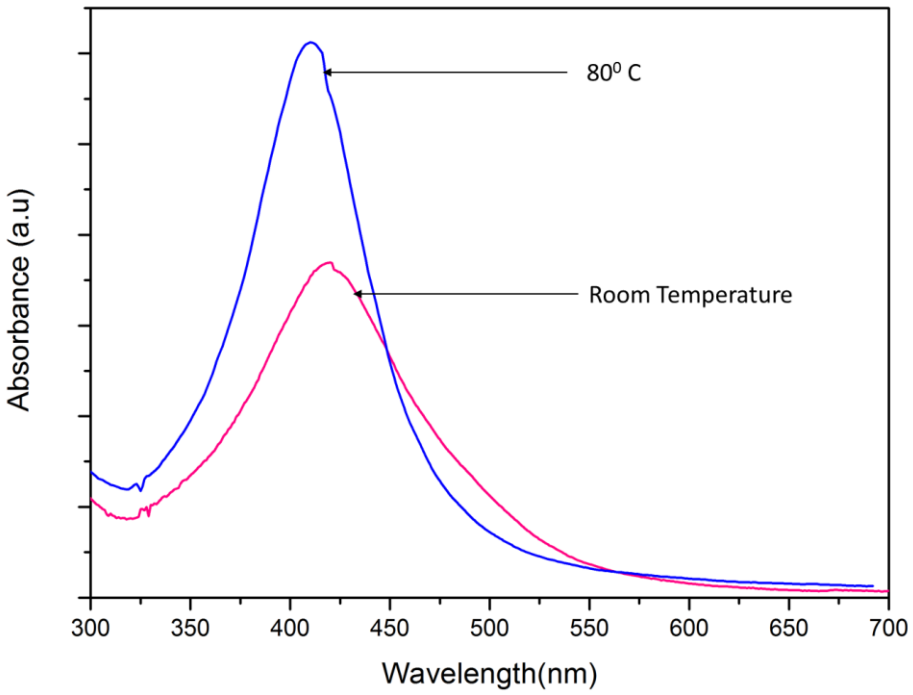

Figure 4.8: UV-VIS spectrum of silver nanoparticle suspensions prepared at room temperature and 80^0 C.

A significant increase in the height of the plasmon peak was observed (Figure 4.8) when the reaction was performed at 80^0 C (reflux temperature of ethanol), indicating that the concentration of the silver nanoparticles produced had increased [4.10]. In addition, a decrease in the FWHM of the plasmon peak as well as a blue shift was observed as shown in Table 4.2, compared to when the reaction was performed at room temperature.

Table 4.2: FWHM and Plasmon Resonance Peak data of silver nanoparticle suspensions prepared at room temperatures and 80^0 C.

Temperature (^{0} C)	**FWHM (nm)**	**Plasmon Peak (nm)**
Room Temperature (25)	82.2	419.7
80	62.4	412

Shifts of the plasmon peak to shorter (blue) or longer (red) wavelengths also reveal information about the size of the nanoparticles. Blue shifts correspond to reduced particle sizes, whilst red shifts correspond to increased particles sizes. A blue shift occurs as a result of increased electron densities of the particles [4.24], which in turn produce an increase in the

electron oscillation, hence causing a shift towards shorter wavelengths [4.24]. Red shift would therefore result in a reverse effect; hence causing shifts to longer wavelengths [4.24].

Since the FWHM had decreased (Table 4.2) and the plasmon peak position had shifted to shorter wavelengths (blue shift), it would suggest that the particles in the suspension are more uniform as well as smaller in size [4.10].

4.4.2HRTEM analysis of silver nanoparticles prepared at room temperature and 80 ^{0}C.

HRTEM was therefore used to investigate the size and morphology of the particles. The HRTEM micrographs of the silver nanoparticles prepared at room temperature and 80^{0}C, are illustrated in Figure 4.9.

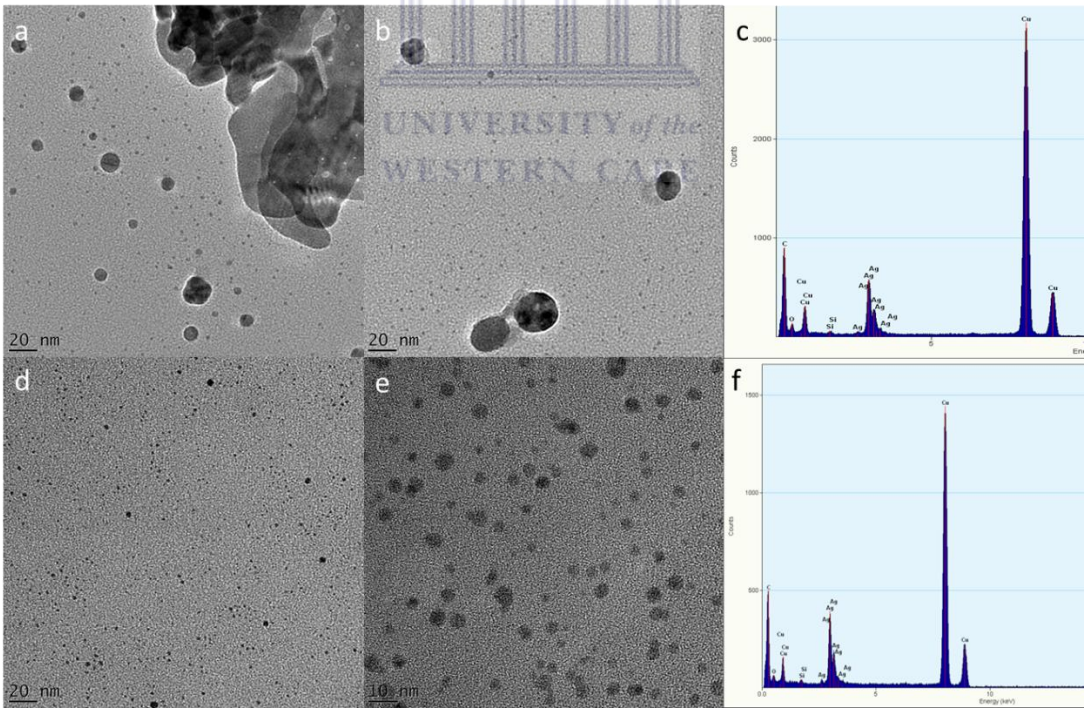

Figure 4.9: HRTEM micrographs of silver nanoparticle suspensions synthesized at (a and b) room temperature with a broad size distribution, (c and d) suspensions prepared at 80^{0}C, (b) and (d) are the EDS spectrums of the nanoparticles shown in the micrographs.

From Figure 4.9, it is evident that various structures were present in the suspensions. For suspensions prepared at room temperature, the presence of large (951 nm) sheet like structures (Figure 4.9 (a)), agglomerates as well as small particles (2 nm) were observed (Figure 4.9 (b)), thus confirming the broad size distribution of the particles predicted by the UV-VIS spectrum (Figure 4.8). HRTEM micrographs of the suspension prepared at 80^0 C revealed sheet like (442 nm) structures (not shown here), and very small (1.25 nm) particles (Figure 4.9(c) and (d)). This confirms the results predicted by the UV-VIS data, since a more uniform size distribution and smaller sizes were obtained when the reaction was performed at 80^0 C.

When the silver nanoparticle suspensions are exposed to reflux temperatures, the particles may be characterized by wide Brownian motions, which results in an increased mobility of the atoms on the surface. The probability of particle collision is therefore increased, and hence particle coalescence is greater due to sintering. The system will then try to attain thermodynamic equilibrium as a result of the coalescence and in turn decrease the total surface area of the particles. However, the presence of the stabilizer, PVP, prevents the sintering of the colloids, thus producing smaller particles as predicted by the blue shift of the plasmon peak (Figure 4.8) and the HRTEM analysis (Figure 4.9 (c) and (d)) of the suspension prepared at 80°C [4.6].

One could conclude that when preparing suspensions at room temperature the environment is uncontrolled and the surrounding temperature of the particles may vary, thus influencing the growth of the particles.

Since the UV-VIS and HRTEM results of silver nanoparticle suspensions suggest that an increase in temperature is necessary in the synthesis of silver nanoparticles, not only to speed

up the reaction, but to decrease the size of the particles and produce more uniform particles, the effect of the reaction time at reflux temperatures was investigated.

4.5 Effect of reaction time at reflux temperature (80^0 C).

The effect of the reaction time at the reflux temperature of 80^0 C was investigated by dissolving $AgNO_3$ in a solution of PVP and ethanol. The detail of the experiment is provided in Section 3.2.3. Samples were taken every consecutive hour, to investigate the optimal reaction time at reflux temperature.

4.5.1 Optical properties of silver nanoparticles prepared at various reaction times at 80^0 C.

Figure 4.10 shows the UV-VIS spectrum of silver nanoparticle suspensions taken during the synthesis at various reaction times. A characteristic plasmon peak, at approximately 413 nm (Figure 4.10) accompanied by a colour change from clear to brown indicated the presence and formation of silver nanoparticles [4.10].

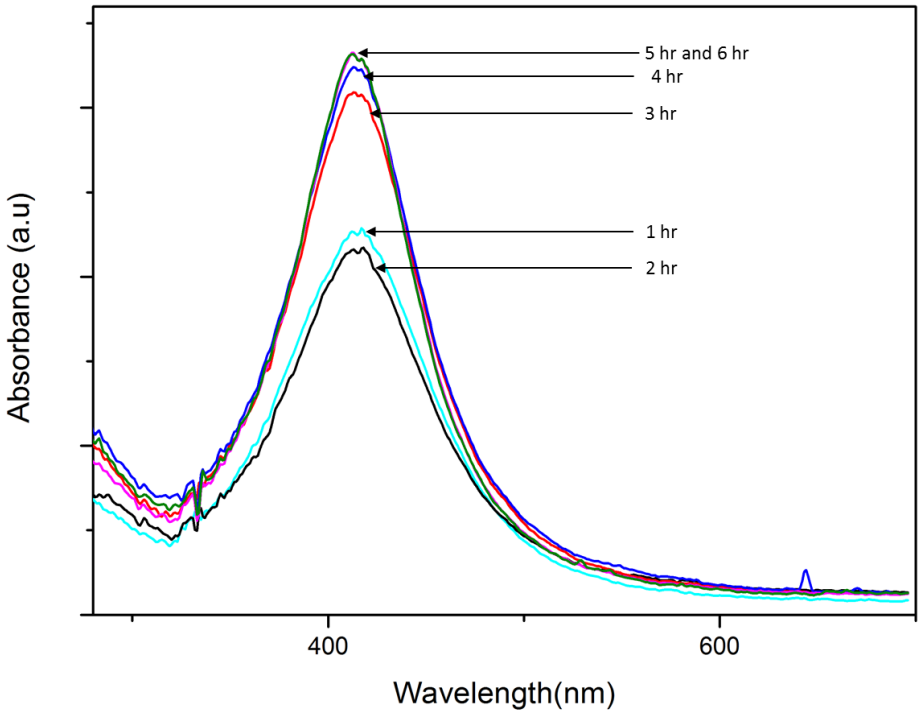

Figure 4.10: UV-VIS spectrum of silver nanoparticle suspensions prepared at various reaction times.

As the reaction time increased, a noticeable increase in the height of the absorbance peak was observed; an indication that the concentration of the silver nanoparticles increased with the reaction time [4.6]. After the second hour a slight drop was observed in the plasmon peak height, which could possibly imply that the concentration of the nanoparticles decreased. This may be attributed to a temperature drop during the course of the second hour from 80° C to approximately 70° C. As the reaction proceeded, the temperature increased to 80° C once again and remained roughly stable during the course of the experiment. This indicates that the temperature has a significant effect on the formation of silver nanoparticle, and that a stable control of the temperature is required to obtain optimal results.

From 1 to 5 hours of the reaction, an increase in the absorbance was observed up to 5 hours of reaction time, indicating that more particles were produced.

The UV-VIS spectra of the 5 and 6 hour reaction times were identical and hence appear to have similar concentrations. Hence no more particles were being produced.

The FWHM and plasmon peak position of the silver nanoparticles prepared at reflux temperature is shown in Table 4.3.

Table 2.3: Data of the characteristic plasmon peaks and FWHM of various reaction times during the reaction.

Time (hr)	FWHM (nm)	Plasmon Peak (nm)
1	79.9	414.2
2	75.9	414.3
3	71.8	413.6
4	68.7	413.5
5	67.1	412.6
6	65.1	412.4

With an increase in the reaction time, a corresponding decrease in the FWHM and plasmon peak position was observed (Table 4.3). Thus indicating that an increase in the reaction time at reflux temperatures produces more uniform distribution of silver nanoparticles [4.10, 4.12, 4.13]. Since the change in the absorbance appeared to be minimal (Figure 4.10) between 5 and 6 hours of the reaction, it may be concluded that a reaction time of 6 hours is the optimal reaction time for the synthesis of silver nanoparticles at elevated temperature, since no new nanoparticles are formed at this stage and a narrower FWHM was obtained (Table 2.3).

The HRTEM analysis of the silver nanoparticles prepared at various reaction times at reflux temperature is discussed in the section to follow.

4.5.2 HRTEM analysis of silver nanoparticles prepared at various reaction times at 80^0 C.

HRTEM micrographs of suspensions prepared at various reaction times, shows the growth of the silver nanoparticles during the reaction. The presence of small spherical particles (Figure 4.11 (a)), and sheets (Figure 4.11 (b)) were observed. The Scanning Transmission Electron Microscopy (STEM) micrograph of the silver nanoparticles, observed in close proximity of the sheet like structure illustrated in Figure 4.11 (b), is shown in Figure 4.11 (c). The micrographs represent the various structures observed throughout the reaction.

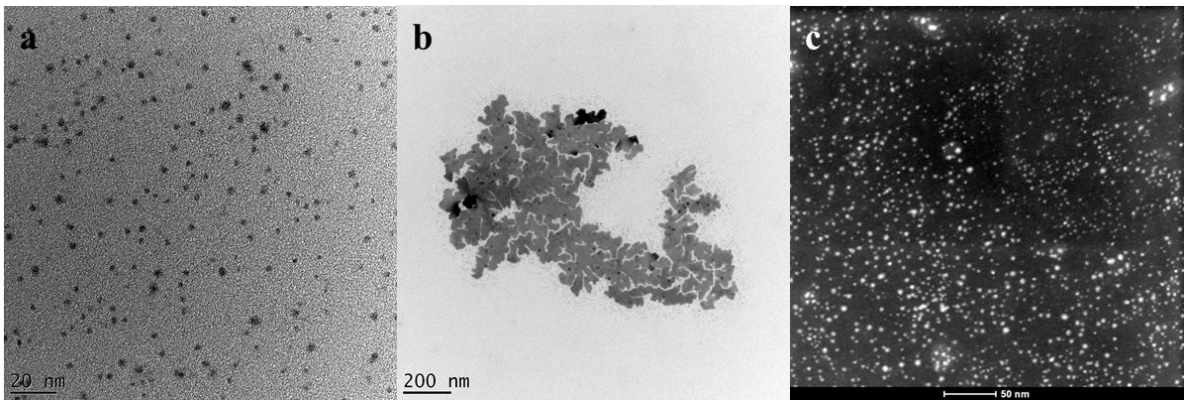

Figure 4.11: HRTEM micrographs of silver nanoparticle suspension at 1hour of the reaction time show the presence of (a) small spherical particles, (b) sheet like structures, and (c) STEM image of small silver nanoparticles surrounding the sheet like structure.

From the micrographs it is evident that formation of the silver nanoparticles occurs within the 1st hour of the synthesis. As the reaction progresses to 6 hours, the presence of sheet like structures are no longer observed (decreased from 824 nm to 310 nm from 1 to 3 hours). However , this may be due to the limitation provided by HRTEM analysis since it only makes use of a relatively small portion of the suspension. The portion of the suspension used for the analysis may have only contained spherical particles, hence the absence of these structures in the micrographs.

Small particles (1.9 nm) were observed in close proximity of the sheet like structures as evidenced by the HRTEM and STEM images in Figure 4.11 (a and c). This may indicate that the particles undergo a process known as Ostwald ripening [4.26] during the reaction. Initially the particles have a non-uniform distribution of particles, leaving the system thermodynamically unstable. The system will try to attain a more energetically stable environment by allowing the smaller higher energy particle to be absorbed by the larger particles that have lower energy. This relationship is explained by the curvature dependence of the chemical potential [4.26, 4.27].

$$\mu = \mu_0 + V_m \gamma \kappa \tag{4.3}$$

Here μ_0 is the chemical potential of an atom on a flat interface, V_m the volume molar ratio, γ the specific surface energy, and κ the mean interfacial curvature. Equation (4.3) shows that the particles will flow from a region of lower curvature towards a region of higher curvature. As a result the smaller particles with greater curvature and higher energy will flow towards regions with lower energy, in which case the larger particles will prevail. As a result of the dissolution of the smaller particles onto larger ones; the overall energy of the system is decreased. Thus the process of Ostwald ripening results in an overall increase in the particle

size [4.27]. This process may be prevented by allowing a controlled system such that the particles that are produced initially have the same particle size [4.27].

PVP prevents particle agglomeration, by adsorbing onto the surface of the silver nanoparticles. The ability to protect the nanoparticles may depend on the concentration of PVP used during the synthesis, since sufficient PVP should be provided to adsorb onto all the nanoparticles produced in the suspension. The effect of PVP concentration on the formation of silver nanoparticles will therefore be discussed in the Section to follow.

4.6 Effect of PVP concentration at 80^0 C.

Silver nanoparticle suspensions were prepared by reducing silver nitrate in the presence of PVP and ethanol, at 80^0 C. The concentration of the PVP was increased, which ranged from 4 to 20 wt. %, in order to investigate the optimal concentration of PVP required to obtain the best possible dispersion of the silver nanoparticles. A detailed procedure is provided in Section 3.2.4.

4.6.1 Optical Properties of the effect of PVP concentration at 80^0 C.

Figure 4.12 shows the UV-VIS spectrum of silver nanoparticles supsensions with increasing PVP concentrations. Characteristic plasmon peak at approximately 412nm confirmed the presence of silver nanoparticles [4.10].

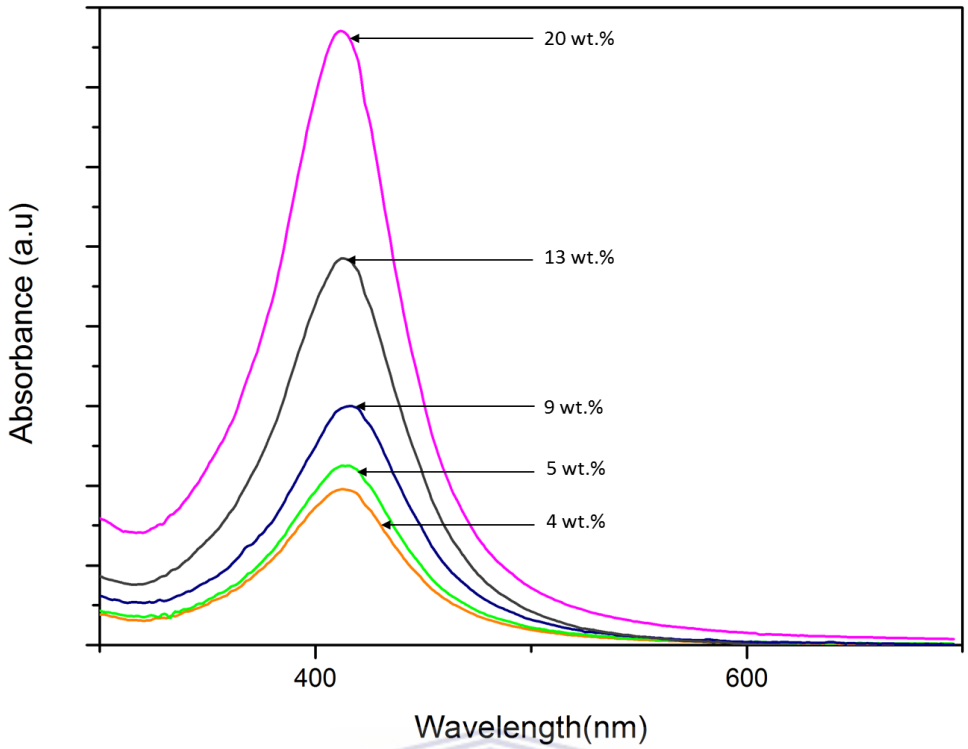

Figure 4.12: UV-VIS spectrum of silver nanoparticle suspensions with increasing PVP concentration.

As the concentration of the PVP was increased an increase in the height of the plasmon peak was observed, indicative of an increase in concentration of silver nanoparticles [4.10]. The position of the plasmon peaks and FWHM of the UV-VIS spectra of suspensions with varying concentration of PVP is exhibited in Table 4.4.

Table 4.4: Data of the characteristic plasmon peaks and FWHM of suspensions with varying PVP concentration, ranging from 4 to 20 wt. %.

PVP (wt. %)	Plasmon Peak	FWHM
4	410.7	60.1
5	412	59
9	413.7	60.7
13	411.2	61.6
20	409.7	57.9

Table 4.4 shows that the plasmon peak of the silver nanoparticles fluctuate as the PVP concentration increases; initially there is an increase from 4 to 9 wt.%, and then a decrease from 9 to 20 wt.%. However, these fluctuations are minimal and appear to be more or less the same. Since the sizes are so broad, one would expect to have more of the same or different particles present in the suspension (all depending on what sizes were present in the extracted sample used for the UV-VIS analysis).

As the PVP concentration increased to above 5 wt.% PVP, the viscosity of the suspension increased (visual observation). Immediate colour changes of the mercky suspensions to brown were observed with increasing PVP, indicating the formation of silver nanoparticles in the initial stages of the reaction.

UV-VIS spectra of the silver nanoparticle suspensions may also be used to determine the band gap of the silver nanoparticles, since silver has a direct band gap [4.22]. The process of determination of the band gaps of the silver nanoparticles are described in Section 3.4.1.3.

The plot of A^2 vs. $h\nu$ for the effect of PVP concentration on the formation of silver nanoparticles is illustrated in Figure 4.13.

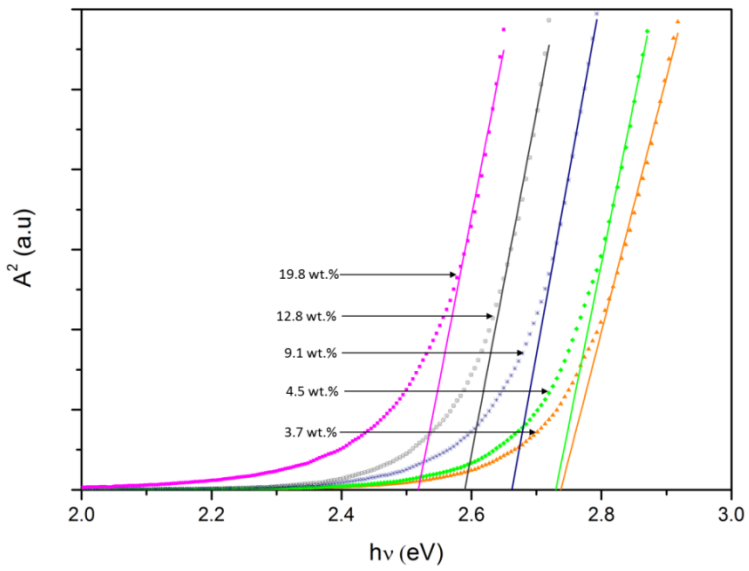

Figure 4.13: Plot of A^2 vs. hυ to determine the band gap of the silver nanoparticles at various concentrations of PVP.

Using the band gaps determined for the particles with varying PVP concentration, a graph of the effect of PVP concentration on the band gap was plotted, as illustrated in Figure 4.14.

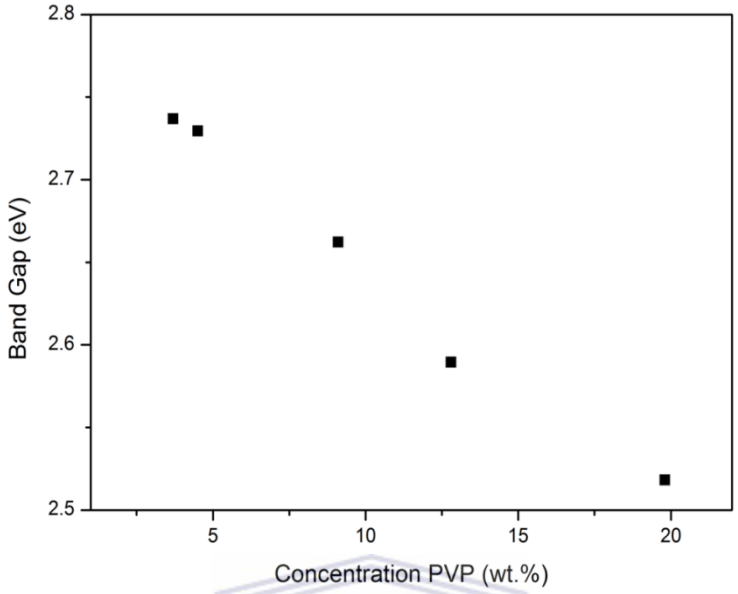

Figure 4.14: Plot of the band gap energy as a function of the PVP concentration.

Figure 4.14 illustrates an indirect relation between the band gap energy of the silver nanoparticles and the PVP concentration. This suggests that the silver nanoparticles increase in size as the PVP concentration is increased. As the size of the nanoparticles increase the amount of atoms constituting the particles increase, and the energy levels become less discrete [4.28].

The suspension containing the most amount of PVP (1:50, Ag:PVP) had the smallest FWHM. This may indicate that this ratio is the best to produce more uniformly distributed silver nanoparticles.

The HRTEM analysis of the silver nanoparticles provide information about the morphology of the particles with increasing PVP concentration, and may be used to confirm the prediction made by the UV-VIS analysis.

4.6.2 HRTEM analysis of the effect of PVP concentration at 80^0 C.

HRTEM micrographs (Figure 4.15) of the silver nanoparticles suspensions revealed the presence of various structures. Once again a combination of sheet like structures, agglomerates and small particles were observed. Figure 4.15 shows a representation of the silver nanoparticles observed throughout the samples of different PVP concentrations. The EDS spectrum of the sheet like structure illustrated in Figure 4.15 (a) is shown in the inset of Figure 4. 15 (a).

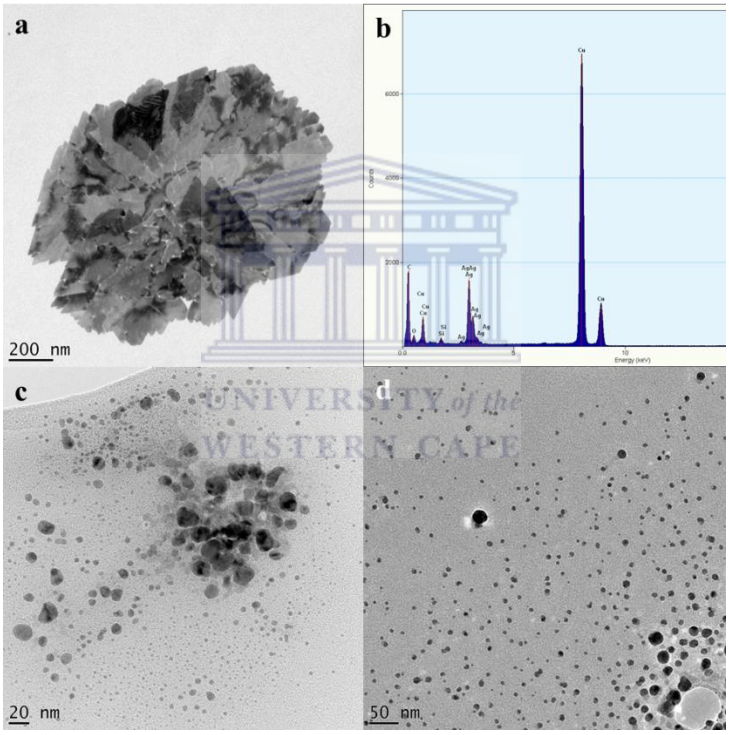

Figure 4.15: HRTEM micrographs of (a) sheets, (c) and (d) particles observed for various concentrations of PVP, (b) shows the EDS spectra of the sheet like structure exhibited in (a).

The micrographs were used to obtain the average particles sizes of the spherical silver nanoparticles prepared with increasing PVP concentrations. The sizes obtained for the PVP concentrations of 4, 5, and 13 wt.%, was 2.99 ± 0.785, 3.56 ± 3.867, and 8.15 ± 7.689 nm, respectively. Hence, an increase in the particle size was observed with an increase in PVP

concentration The standard deviation also increased, indicating that the dispersion of the particles decreases (becomes less uniform). This result does not agree with the results predicted by the FWHM of the UV-VIS results. The discrepancy may be due to the limitation mentioned before; since HRTEM only makes use of one drop of the sample, it is not a true representation of the particles. Evidently the size of the silver nanoparticles increased as the PVP concentration was increased, confirming the results obtained from the band gap analysis of the silver nanoparticles with increasing PVP concentration.

The increase in size may be due to the increased viscosity since it results in a decreased diffusion of the Ag atoms within the nanoparticle suspension, thus slowing down the reduction of silver ions within the system [4.29]. Increases in the viscosity may also lead to a reduced rate of nucleation R_N in the growth process of the reaction as depicted by:

$$R_N = \frac{C_o kT}{3\pi\lambda^3\eta} e^{\left(\frac{\Delta G^*}{kT}\right)} \tag{4.4}$$

Where C_o is the solubility, k Boltzmann constant, T the successful jump frequency, λ the diameter of the growth species and η the viscosity of the suspension. Thus from equation (4.4) it is evident that the rate of nucleation is inversely related to the viscosity of the suspension. Uniform particles will be obtained if all nuclei formed in suspension occur simultaneously, however during the synthesis the viscosity of the suspension increased and hence the rate of nucleation varied, preventing the nuclei from forming simultaneously, thus producing non-uniform particle sizes [4.29]. Simultaneous nucleation may possibly be obtained my incorporating a stronger reducing agent [4.30].

EDS analysis (Figure 4.15 inset) of the sheet like structures confirmed the presence of silver, the presence of oxygen, carbon and nitrogen are also evident, which could be due to the presence of PVP.

Figure 4.15 a shows a sheet like structure with dimensions in the micrometre range. High resolution micrographs of the sheet like structures shows that the sheet possess parallel fringes of 2.0 Å and 2.4 Å (Figure 4.16 (a) and (b)), corresponding to the d spacing of {200} and {111} planes, respectively, of *fcc* silver [4.14, 4.31]. The discontinuous and free nature of the parallel fringes suggest that the sheet like structures provide active growth areas for smaller surrounding nanoparticles to attach to the {111} planes [4.14].

The corresponding SAED spots (Figure 4.16 (c)) were obtained along the [111] direction of the silver sheet like structures. These spots illustrate the single crystalline nature of the sheet like structure. The spots may be indexed to $(0\bar{2}2)$, $(2\bar{2}0)$, $(20\bar{2})$, of the *fcc* silver [4.14].

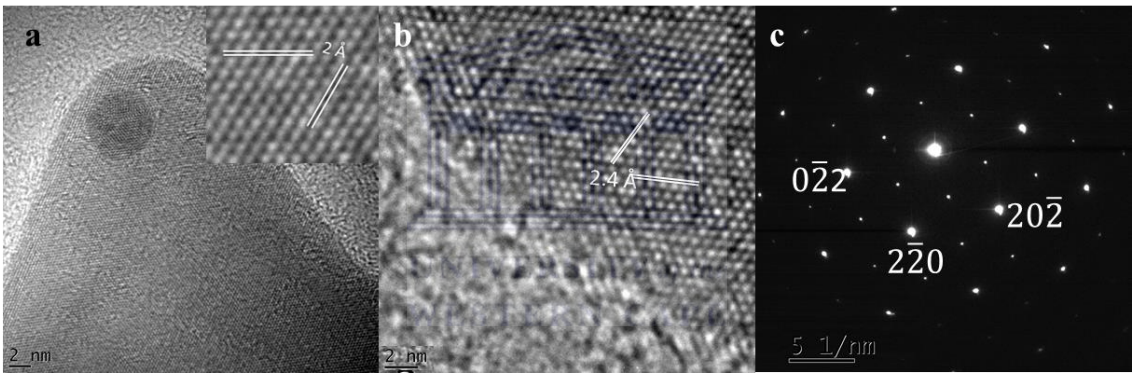

Figure 4.16: High Resolution images of the sheet like structures exhibiting the parallel fringes corresponding to the interplanar d spacing of fcc silver.

The attachment to the {111} planes of the structure, occurs due to the preferential adsorption of PVP onto the {100} surface of silver nanoparticles. This passivates the growth along the {100} facets, leaving the {111} facets exposed and highly reactive, facilitating growth along these facets and hence resulting in the anisotropic growth along the {111} directions of the *fcc* silver crystal [4.23, 4.31, 4.32, 4.33]. Similar results have also been observed by Zang et al [4.32].

In order to gain more insight into the factors that could possibly affect the formation of silver nanoparticles, a different solvent was introduced.

4.7 Effect of solvent.

The initial process of the polyol synthesis technique is the reduction of a metal salt, such as $AgNO_3$ precursor salt solution. When dissolved, the $AgNO_3$ is separated into a positively charged silver ion (Ag^+) and negatively charged nitrate ions (NO_3^-). The donation of an electron from a reducing agent would produce zero valent silver. The silver ions are hence being reduced during this process. A typical redox equation of the silver ions is presented in equation (4.5) [4.34]:

$$Ag^+ + e^- \rightarrow Ag \tag{4.5}$$

It is known that reducing agents influences the size, shape and distribution of the silver nanoparticles [4.35]. In order to obtain a uniform distribution of nanoparticles, the nucleation process should occur rapidly in very short time periods. This implies that the silver ions should be reduced rapidly, to allow the formation of zero valent silver simultaneously, and converted to stable nuclei so that the growth process may continue [4.36]. The strength of the reducing agent is therefore important since stronger reducing agents would allow for the rapid production of silver nuclei in the initial stages, whilst weaker reducing agents would allow for slower reduction periods [4.30].

The reduction of the silver ions in the present study was performed using ethanol and ethylene glycol. A detailed procedure is provided in Section 3.2.5.The reduction equation of silver in an ethanol is given by:

$$2Ag^+ + C_2H_5OH + H_2O \rightarrow 2Ag + C_2H_5O_2^- + 3H^+ \tag{4.6}$$

The reduction of the silver precursor with ethylene glycol occurs via the following mechanism [4.37]:

$$2HOCH_2CH_2OH \rightarrow 2CH_3CHO + 2H_2O \quad (4.7)$$

$$2Ag^+ + 2CH_3CHO \rightarrow CH_3CO–OCCH_3 + 2Ag + 2H^+ \quad (4.8)$$

In the process of equation (4.7), the dehydration of ethylene glycol occurs to produce acetaldehyde, which is ultimately responsible for the reduction of the silver (equation (4.8)) [4.38, 4.39]. During the reduction process the silver atom concentration will increase until it reaches the supersaturation level. Once this level is reached the nucleation and growth of the silver atoms will begin, and hence facilitate the growth of silver nanoparticles in the solution phase [4.37].

4.7.1 Optical Properties of silver nanoparticles prepared in ethanol and ethylene glycol.

The UV-VIS spectra of the silver nanoparticles suspended in ethylene glycol and ethanol are given in Figure 4.17.

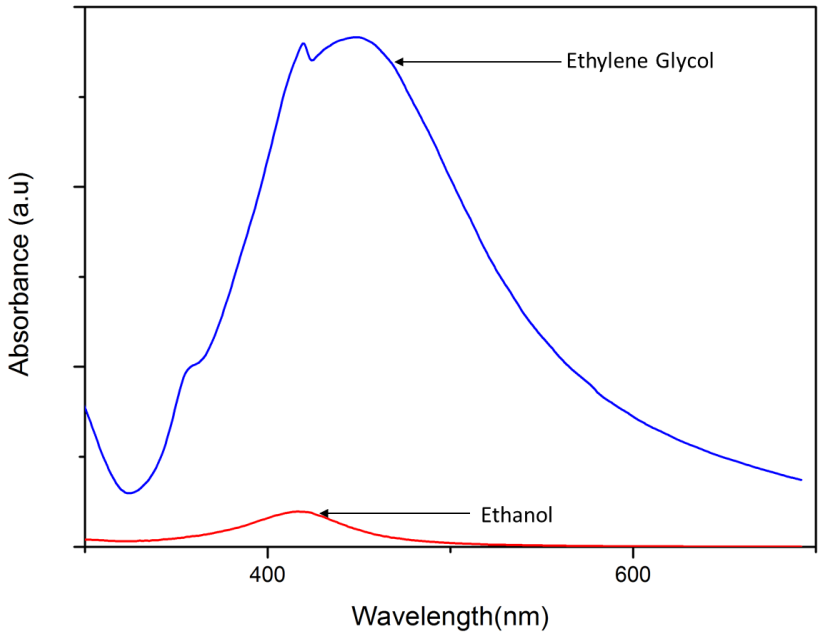

Figure 4.17: UV-VIS spectrum of silver nanoparticle suspensions prepared in ethylene glycol and ethanol.

From Figure 4.17, it is evident that the ethylene glycol has a substantial effect on the amount of the silver nanoparticles produced, since a significant increase (~93 %) in the absorption for the silver nanoparticles (prepared in ethylene glycol) was observed. Hence an increased concentration of silver nanoparticles was produced by the ethylene glycol, compared to the ethanol. This increase may be attributed to the reducing ability of the respective solvents. Ethylene glycol appears to be a stronger reducing agent, compared to ethanol, as more particles were produced.

In addition, the plasmon peak of the ethylene glycol suspended nanoparticles was observed to be broad (Figure 4. 17), indicative of a broad size distribution.

The formation of secondary and ternary peaks at 355 and 471nm in the spectrum of the ethylene glycol suspension may be attributed to the presence of various shaped nanoparticles. Since the plasmon resonance of the silver nanoparticles is directly related to the curvature of the nanoparticles [4.40], the particles with sharper edges will have an enhanced degree of charge separation, due to the concentration of charge at the sharper edges [4.40]. This in turn, would result in a decreased Coloumbic restoring force. Thus, the period of the electron oscillation is increased, and consequently the frequency is decreased.

4.7.2 HRTEM analysis of silver nanoparticles prepared in ethanol and ethylene glycol.

The HRTEM micrographs of the silver nanoparticles prepared in ethylene glycol are shown in Figure 4.18. Various shaped particles such as triangles, squares, rods and spherical particles were observed, as predicted by the presence of secondary and ternary peaks in the UV-VIS spectrum of the suspension (Figure 4.17). The shape of nanoparticles produced is primarily depicted by the nucleation process of the nanoparticle, that is, whether or not homogenous or heterogeneous nucleation takes place.

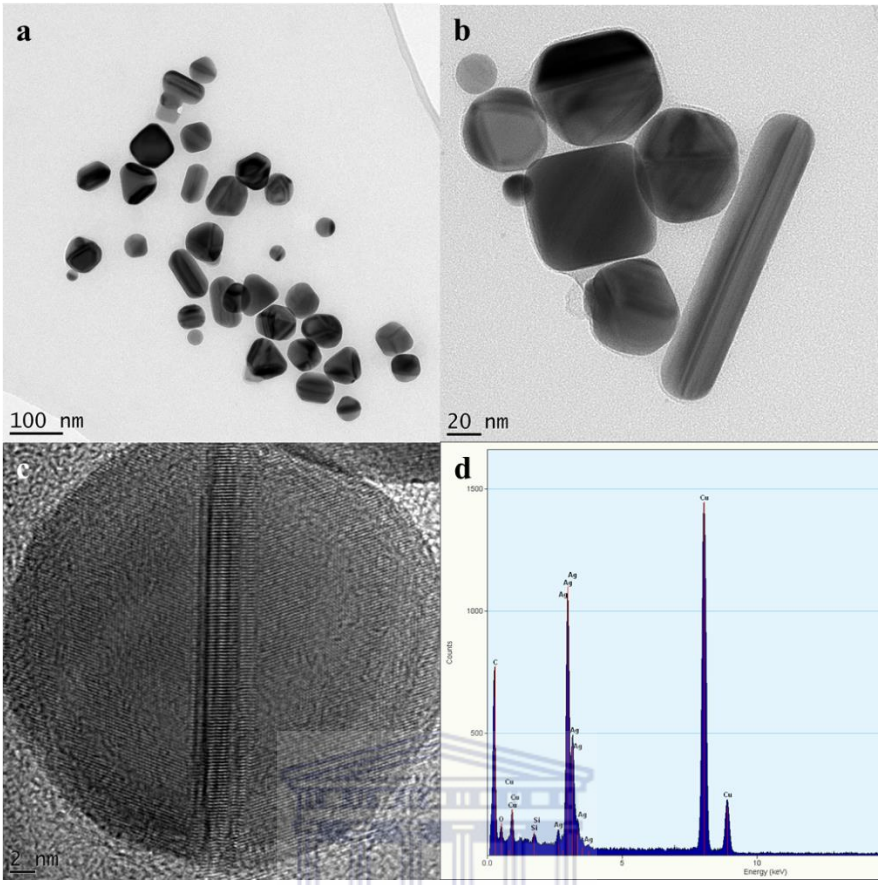

Figure 4.18: HRTEM micrographs of silver nanoparticles prepared in ethylene glycol, (a) low magnification of the various shaped particles, (b) enlarged image of the various shapes produced and (c) high resolution image of a spherical particle with defects, (d) shows the EDS spectra of the nanoparticles.

Homogenous nucleation takes place when the reaction occurs in situ and hence, nucleation and growth of the nanoparticles are controlled by the same chemical process. Thus, single step synthetic processes of nanoparticles, undergo homogenous nucleation. However, in the case of heterogeneous nucleation, the nucleation and growth processes occur separately. A preformed suspension of nanoparticles is added to a reactant mixture, hence isolating the nucleation and growth processes [4.30].

Since the silver nanoparticles reported in this study were produced by a single step, “one pot” synthesis, nucleation and growth was controlled by the same chemical process and hence

homogenous nucleation of the nanoparticles took place. The formation of the nanoparticles may be explained by La Mer model as illustrated in Figure 4.19 [4.30].

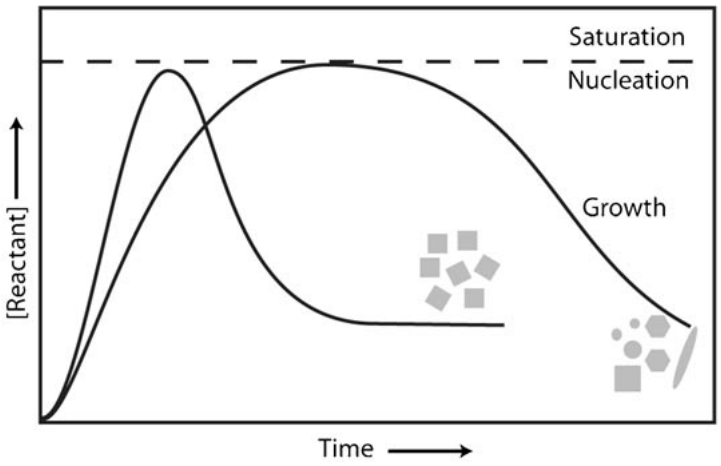

Figure 4.19: The La Mer model describing the nucleation process of nanoparticles, illustrating that a critical concentration of reactant is required to produce uniform shaped nanoparticles [4.30].

As mentioned previously (Section 2.5), the nucleation and growth will occur once the supersaturation concentration of silver atoms is obtained. Above this concentration the reactants would rapidly deplete due to nucleation so that the succeeding growth occurs on the pre-existing nuclei. Further nucleation will be discouraged as long as the reactant concentration does not exceed the supersaturation concentration. Hence, nucleation must occur almost instantaneously in order to produce uniformly shaped particles [4.30].

The formation of the various shaped particles may be attributed to a prolonged nucleation process, since this allows for the non-uniform depletion of reactants in the solution, resulting in the variation in the growth rate of the silver nanoparticles produced at different times during reaction process.

By refluxing the silver nanoparticle suspension at the boiling temperatures of the solvents, the nucleation process is allowed to occur at a faster rate. However, it is necessary to obtain sufficient reactant species, such that the critical nucleation concentration is reached. PVP was

employed to slow down the nucleation rate, and in turn obtain sufficient reactant species, which would result in the production of homogenously shape particles [4.30]. However, since the nanoparticles produced were not homogenously shaped, it suggests the initial concentration of the reactants were not sufficient to obtain the critical nucleation concentration [4.30].

The HRTEM micrograph of the silver nanoparticles produced in ethanol is illustrated in Figure 4.20.

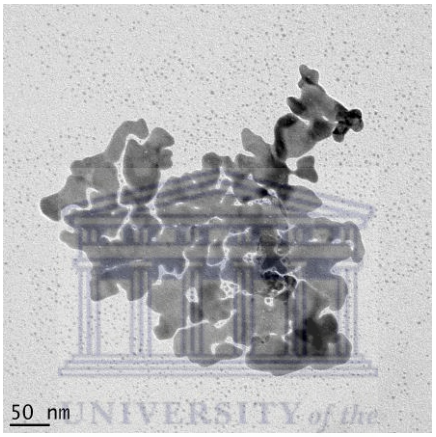

Figure 4.20: HRTEM micrographs of silver nanoparticles prepared in ethanol.

By comparing the particles prepared in ethylene glycol (Figure 4.18) to those prepared in ethanol (Figure 4.20), it is evident that no sheet like structures are present in the ethylene glycol based suspensions. It would therefore imply that the formation of the particle produced is dependent on the reducing ability of the reducing agent/solvent.

A weaker reducing agent would slow down the nucleation rate of the silver nanoparticles. As a result, all the nuclei would not be produced at the same time, and hence a non-uniform distribution of the size of the nanoparticles would be produced. The subsequent growth process would then continue on the pre-existing non-uniform particles produced during the nucleation process. Since the particles produced would hence be non-uniform, Ostwald

ripening would take place such that thermodynamic stability may be obtained [4.30], producing the sheet like structures observed.

The reduction process is also sensitive to the pH of the solution, since it would affect the morphology of the silver nanoparticle produced [4.35]. It is known that the pH of ethanol is 7.3, and ethylene glycol is 7.5 [4.41, 4.42]. After the reaction, the pH of the ethylene glycol suspension was measured to be 4.28, whilst the pH of the ethanol suspension was 2.10. For suspensions with lower pH, the reducing ability is slowed down [4.35] and hence nucleation is slowed down. The formation of acid during the reduction processes is evident from equations (4.6) and (4.8). Since the starting material used was $AgNO_3$, the nitrate ions may have combined with the H^+ ions to form HNO_3, which is a very strong acid, hence the lower pH observed. The variation in pH of the two suspensions may therefore be attributed to the reducing ability of ethylene glycol and ethanol and hence the concentration of H^+ ions produced during the reactions.

In an attempt to steer away from PVP as a surfactant/stabilizer, the stabilizing ability of chitosan, a biodegradable polymer, was investigated.

4.8 Stabilizing abilities of a biodegradable polymer: Chitosan.

Surfactants are employed during the synthesis of the silver nanoparticles in order to prevent particle aggregation. Chitosan is a naturally occurring cationic polysaccharide which can be used as a surfactant to protect silver nanoparticles against particle aggregation [4.43]. The benefits of employing this surfactant in the synthesis is due to its environmentally benign nature and the presence of free amino and hydroxyl groups within its structure, providing it with extraordinary physicochemical properties [4.43]. Recently chitosan has been employed as a reducing agent in the synthesis of gold nanoparticles [4.44].

The use of the stabilizer reported herein, was a preliminary study performed in order to investigate whether or not this polymer may be used to synthesize silver nanoparticles using a cost effective polyol synthesis method.

Chitosan is insoluble in ethanol (95%) [4.43], therefore it was not used as a solvent/reducing agent for the synthesis of the silver nanoparticles. Instead, ethylene glycol was used as a solvent/reducing agent during this investigation. $AgNO_3$ was dissolved in a solution of chitosan and ethylene glycol, and magnetically stirred under reflux. Details of the experimental procedure are provided in Section 3.2.6.

An immediate colour change from clear to dark brown was observed, indicating the formation of silver nanoparticles. However, the suspension settled at the bottom of the round bottomed flask. UV-VIS analysis of the silver nanoparticle suspension proved to be problematic, as a homogenous suspension was not obtained. Therefore the chitosan-stabilized silver nanoparticles were characterized by HRTEM only.

4.8.1 HRTEM analysis of silver nanoparticles protected by chitosan.

HRTEM micrographs of the silver nanoparticles suspension revealed the presence of spherical particles as exhibited in Figure 4.21 (a) and (b). All the particles produced were observed to be spherical, and the presence of small and large particle in the range of 4 nm- 71 nm, were observed. The average particle size distribution was measured to be 9.04 ± 7.1nm. It is therefore evident from the broad size distribution that the silver nanoparticles are not uniform in size.

The EDS spectrum (Figure 4.21 (c)) confirmed the presence of silver. The carbon, nitrogen and oxygen peaks observed could be due to chitosan, whilst the copper may be attributed to the copper grid. However, some carbon may also be attributed to the carbon film on the

copper grid. The silicon peak in the spectrum could be due to contamination, possibly from the silica oil used to heat up the suspensions.

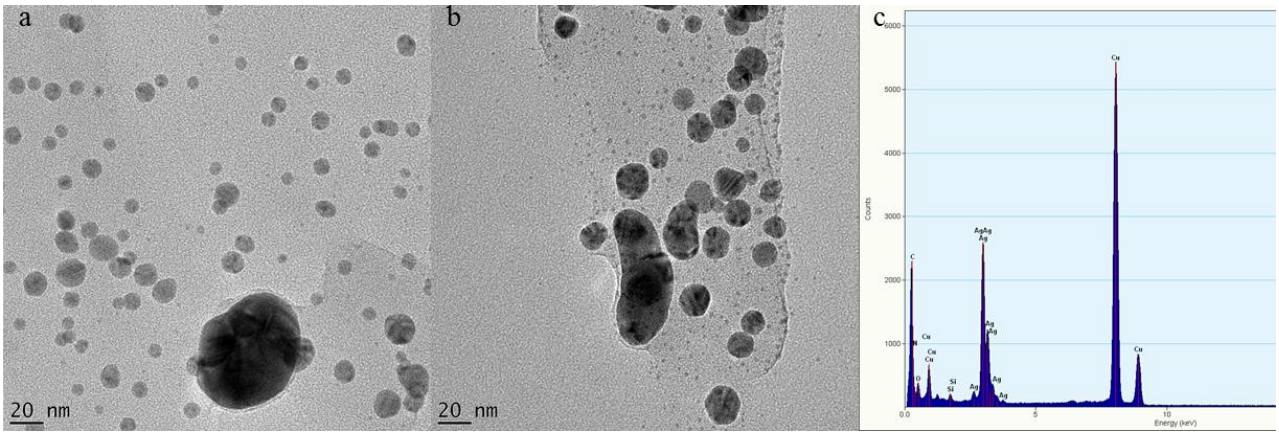

Figure 4.21: HRTEM micrographs of silver nanoparticles prepared in with chitosan as a stabilizer, (a) low magnification of the particles, (b) size variation of the silver nanoparticles, and (c) EDS spectrum of the silver nanoparticles.

Since the nanoparticles are not uniformly dispersed, it may be attributed to the capping ability of chitosan. Chitosan molecules protect the silver nanoparticles by the coordination between the amino groups present in chitosan, and silver atoms. The stabilization between the silver nanoparticles and the chitosan may be investigated by considering the FT-IR analysis of silver nanoparticles. FTIR analysis in this study was not successful due to instrument errors. However, Wei et al has reported the variation in the transmittance of the nitrogen bonds, and suggested that the shift revealed that the nitrogen atoms are the binding sites for silver atoms. In addition, it was suggested that the binding process occurs during the reduction of the $AgNO_3$ [4.45]. Their results also indicate the formation of a new band at 1760 cm^{-1} in the FT-IR spectrum, which corresponds to carbonyl stretch vibrations in ketones, aldehydes and carboxylic acids. The formation of the new band suggested that the reduction of the silver ions is coupled to the oxidation of the hydroxyl groups in chitosan [4.46]. Similar results have been obtained by Wichramarachchi et al [4.43].

The concentration of the chitosan and $AgNO_3$ affects the size and morphology of the silver nanoparticles. In order to obtain uniform morphology of silver nanoparticles a sufficient amount of chitosan should be provided so that it may protect the silver nanoparticles [44].

Further investigations into the effect of surfactant concentration, reducing agent and pH may be investigated in order to produce uniform silver nanoparticles using chitosan as a stabilizer.

Due to time constraints these investigations were not pursued, and will be continued in future, such that uniform morphology of silver nanoparticles, using the polyol synthesis may be obtained.

4.9 Conclusion

Silver nanoparticles has been successfully synthesized, using a simple cost effective, facile polyol synthesis technique.

XRD results of the silver nanoparticles displayed the highly crystalline nature of the prepared silver nanoparticles, these results were confirmed from the SAED patterns of the silver nanoparticles and the sheet like structures.

The TGA results of the silver nanoparticles prepared with PVP as a surfactant, revealed that PVP completely decomposes at 500 ^{0}C. The presence of a higher melting point material was still present at 600^0 C, which could be due to the presence of silver nanoparticles.

When reactions proceeded at room tempertaure, it was established that the reaction process would take several days (6 days) to complete. Since a reaction time of 6 days is a relatively long period to complete a reaction, temperature was incorporated to reduce the reaction time.

When the reaction was performed at reflux temperatures , UV-VIS spectroscopy showed that the optimum reaction time for the formation of silver nanoparticles was 6 hours. The increase

in temperature produced smaller silver nanoparticles that showed elevated uniformity of the particles.

The presence of sheet like structures were also produced, and was observed to grow along the (111) planes of the crystals.In addition, this study has shown that PVP may be incorporated as an an alternative to ammonia to produce sheet like structures.

A ratio of 1:50 (Ag:PVP) was found to be an optimal concentration to produce silver nanoparticles, although larger, but more uniformly dispersed.

UV-VIS analysis of the silver nanoparticles prepared in ethylene glycol, produced anisotropic silver nanoparticles that were larger in size. However, no sheets were produced as compared to the silver nanoparticles prepared in ethanol.

Chitosan was investigated as an alternative, environmetally benign surfactant to produce silver nanoparticles. The investigation was a preliminary study used to determine the possibility of employing chitosan as a surfactant. This surfactant produced silver nanoparticles that were spherical with a broad size distribution.

4.10 References

[4.1] Sau. T., Pal. A, Jana. N, Wang. Z, and Pal. T, *J. Nanopart. Res*, **3**, p 257 (2001)

[4.2] Jiang. H, Moon. K, Zhang. Z, Pothukuchi. S, and Wong. C ,*J. Nanopart. Res*, **8**, p 117 (2006)

[4.3] Yin. B, Ma. H, Wang. S, and Chen. S, *J. Phys. Chem. B,* **17**, p 8898 (2003)

[4.4] Mishra. Y, Mohapatra. S, Kabiraj. D, Mohanta. B, Lalla. N, Pivin. J, and Avasthi. D, *Scripta Materialia*, **56**, p 629 (2007)

[4.5] Zhao. T, Sun. R, Yu. S, Zhang. Z, Zhou. L, Huang. H, and Du. R, *Colloids Surf., A,* **366**, p 197 (2010)

[4.6] Carotenuto. G, Pepe. G. P, and Nicolais. L, *Eur. Phys. J. B*, 17, p 11 (2000)

[4.7] Slistan-Grijalva. A, Herrera-Urbina. R, Rivas-Silva. J, Ávalos-Borja. M, Castillón-Barraza. F and Posada-Amarillas. A, *Physica E*, **25**, p 438 (2005)

[4.8] Eduardo. C, Lin. Z and George. C, *J. Phys. Chem. B,* **107**, p 668 (2003)

[4.9] Dang. T, Le. T, Fribourg-Blanc. E, Dang. M, *Adv. Nat. Sci: Nanosci. Nanotechnol,* **3**, (2012)

[4.10] Šileikaitė. A, Prosyčevas. I, Puišo. J, Juraitis. A, and Guobienė. A, *Mater. Sci*., **12,** p 287 (2006)

[4.11] Kellner. R, *Weinheim: Wiley VCH.* (1998)

[4.12] Song. K, Lee. S, Park. T, and Lee. B, *Korean J. Chem. Eng*., **26**, p 153 (2009)

[4.13] Smitha. S, Nissamudeen. K, Philip. D, and Gopchandran. K, *Spectrochim. Acta,* **71**, p 186 (2008)

[4.14] Du. J, Han. B, Liu. Z, Liu. Y and Kang. D, *Cryst. Growth Des.*, **7**, p 900 (2007)

[4.15] Reda. S, Al-Ghannam. S, *AMPC*, **2**, p 75 (2012)

[4.16] Mani. U, Dhanasingh. S, Arunachalam. R, Paul. E, Shanmugam. P, Rose. C, Mandal. A, *Progress in Nanotechnology and Nanomaterials*, **2**, p 21 (2013)

[4.17] Kora. A, Beedu. S, Jayaraman. A, *Organic and Medicinal Chemistry Letters*, **2**, (2012)

[4.18] Piao. L, Lee. K, Min. B, Kim. W, Do. Y, and Yoon. S, *Bull. Korean Chem. Soc*,. **32**, (2011)

[4.19] Swarnavalli. G, Jospeh.V, Kannappan. V, and Roopsingh. D, *Journal of Nanomaterials* (2011)

[4.20] Wei. D, and Qian. W, *Colloids Surf., B*, **62**, p 136 (2008)

[4.21] Sun. L, Liu. A, Tao. X, Zhao. Y, J. Mater. Sci., 46, p 839 (2011)

[4.22] Gasameh. S, Radiman. S, Heng. L, Saion. E, and Saeed. G, *African Physical Review*, **4,** (2010)

[4.23] Slistan-Grijalva. A, Herrera-Urbina. R, Rivas-Silva. J, Ávalos-Borja. M, Castillón-Barraza. F and Posada-Amarillas. A, *Physica E*, **25**, p 438 (2005)

[4.24] Evanoff. D and Chumanov. G, *Chemphyschem*, **6**, p 1221 (2005)

[4.25] Zhao. T, Sun. R, Yu. S, Zhang. Z, Zhou. L, Huang. H and Du. R, *Colloids Surf., A*, **366**, p 197 (2010)

[4.26] Gentry. S, Kendra. S, and Bezpalko. M, *J. Phys. Chem*, **115**, p 12736 (2011)

[4.27] Dagtepe. P, and Chikan. V, *J. Phys. Chem*, **3701** ,p 16263 (2010)

[4.28] Nalwa. H Handbook of Thin Films Materials, Academic Press , Volume 5, p 61 (2002)

[4.29] Cao. G, *London: Imperial College Press*, **3**, p 53 (2004)

[4.30] Tao. A, Habas. S, and Yang. P, *Small*, 4, p 310 (2008)

[4.31] Zeng. J, Zheng. Y, Rycenga. M, Tao. J, Li. Z, Zang. Q, Zhu. Y, and Xia. Y, *J. Amer. Soc.*, **132**, p 8552 (2010)

[4.32] Zhang, Y, Yang. P, and Zhang. L, *J. Nanopart. Res.*, **15**,(2012)

[4.33] Nghia. N, Truong. N, Thong. N, and Hung. N, *J. Mater. Chem.*, **2**, p 75 (2012)

[4.34] Chai. K, Lu. Y, Lee. H, *Mater. Chem. Phys*., **94**, p 429 (2005)

[4.35] Khan. Z, Al Thabaiti. S, Obaid. A, Al-Youbi. A, *Colloids Surf., B*, **82**, p 513 (2011)

[4.36] Kim. D, Jeong. S, Moon. *J, Nanotechnology*, 17, p 4019 (2006)

[4.37] Siekkinen. A, Mc Lellan. J, Chen. J, Xia. Y, *Chem. Phys. Lett*,**432**, p 491 (2006)

[4.38] Larcher. D, and Patrice. R, *J. Solid State Chem.*,**154**, p 405 (2000)

[4.39] Komareni. S, Li. D, Newalker. B, Katsaki. H, Bhalla. A, *Langmuir*, **18**, p 5959 (2002)

[4.40] Cobley. C, and Skrabalak. S, *Plamonics*, **4**, p 171 (2009)

[4.41] JJS: Technical services, online: www.jjstech.com/ethanolc2h5oh.html, accessed: 21 October 2013

[4.42] Loctite European Group Technical Service: Produce information sheet, online: ww.akd-tools.gr/xmAssets/File/TDS/LOCTITE/loctite_thermoblu_pured.pdf, accessed 21 October 2013

[4.43] Wichramarachchi. P, Hettiarachchi. M, *J. Sci*, **6**, p 65 (2011)

[4.44] Shaji, J, Jain. V, Lodha. S, *International Journal of Parmaceutical and Applied Sciences*, **1**, p 11 (2010)

[4.45] Wei. D, and Qian. W, *Colloids Surf., B*, **62**, p 136 (2008)

[4.46] H.Z. Huang, and Yang. X, *Biomacromolecules*, **5**, p2340 (2004)

CHAPTER 5

Characterization of Thin Films

5.1 Introduction

Thin film solar cells technologies have received considerable attention since they are more cost effective than conventional thick crystalline silicon wafers, a condition that needs to be met in order to compete with fossil-fuel technologies. The thin film solar cells have thicknesses in the range of 1-2 μm and can be deposited on cheap substrates such as glass, whilst the crystalline silicon wafers have thicknesses in range of 180-300 μm [5.1]. The main limitation of the thin film technology is the ineffective absorption of light in the near-band gap region of the electromagnetic spectrum, as well as the limitations to using light trapping mechanisms such as texturing (which it etches away a large portion of the film) to enhance the path length in the solar cell. Silver nanoparticles exhibit plasmon resonance effects which may be incorporated into thin films in order to allow sufficient light trapping in the cell; this is obtained by scattering the incident electromagnetic radiation into the active region of the cell [5.2, 5.3]. Hence, the effect of the incorporation of silver nanoparticles on thin films were investigated, in order to determine whether the silver nanoparticles could be used to enhance the light trapping of thin films.

As mentioned in Section 3.3, silver nanoparticle suspensions were deposited onto bare Corning 7059 glass substrates by means of a spray technique. The excess solvent of the suspensions were evaporated by placing the glass substrates on a hot plate. Similarly, silver nanoparticle suspensions were deposited on amorphous silicon thin films (a-Si: H) which was

deposited on glass substrates by Hot Wire Chemical Vapour Deposition (HWCVD). HWCVD catalytically decomposes precursor gases across a tungsten filament, which breaks down the inlet gases, and in turn produces film forming precursors. The formed precursors then adhere to the surface of the substrate and results in the growth of a thin film [5.5].

Ethanol and ethylene glycol (EG) based silver nanoparticle suspensions were used for the deposition, in order to investigate the optical responses, which are expected to be different, due to the observed variation in the size and shapes of the nanoparticles (see Chapter 4).

The films prepared from the deposited silver nanoparticle suspensions were characterized by UV-VIS and HRSEM.

5.2 Optical Properties of the silver deposited thin films

The optical properties of the thin films will provide important information about how the incorporation of the silver nanoparticle suspensions on the thin films may be used to enhance the optical response of the thin films. The variation of the optical responses is mainly explained by the plasmon resonance effects of the silver nanoparticles (AgNP), which are governed by the size, shape and dielectric medium surrounding the nanoparticles. The primary role of the silver nanoparticles is to scatter the incident radiation into the active region of the solar cell; the deposited a-Si film. The absorption and scattering cross sections of noble metal nanoparticles are given by equations 2.10 and 2.11, (Section 2.2.2).

For larger particles the scattering cross section would be significantly larger than that of the absorption cross section. Therefore the size used for the particles are of great importance for the enhancements of the optical responses of the thin films. Absorption generally dominates for particles with diameters less than 50 nm, whilst for particles in the range of 100nm scattering will dominate.

Since the key purpose of the silver nanoparticles was to scatter the incident light into the a-Si film (active layer) it is relatively important that the reflection spectra of these nanoparticles are investigated. There are two components of reflection, namely specular and diffuse. Specular reflection refers to a mirror like reflection, off the surface of the thin film sample, whilst diffuse reflectance occurs when the surface of a sample reflects light in various directions. The phenomenon of specular and diffuse reflectance is illustrated in Figure 5.1.

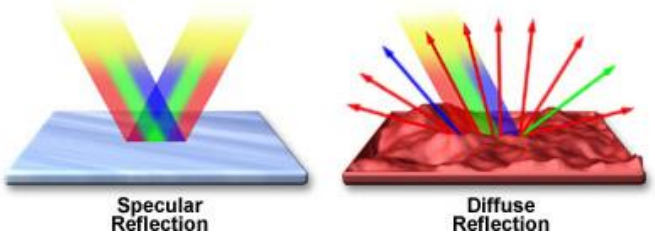

Figure 5.1: Illustration of the two components of reflection; specular and diffuse [5.5].

The transmission spectrum of silver nanoparticles on thin films will provide information about the absorption and scattering of the thin films, whereas specular reflectance will provide information about whether the silver nanoparticles increase the reflection of the thin films. Similarly, diffuse reflectance spectrum will be used to investigate whether the silver nanoparticles scatter the incident light into the absorbing a-Si:H semiconducting layer.

A list of the various substrates used for optical measurements is given in Table 5.1.

Table 5.1: List of substrates used to investigate the optical properties.

Substrate	Modified Substrate
Bare Corning 7059	AgNP in ethanol/bare Corning
	AgNP in EG/bare Corning
a-Si:H bare (on Corning 7059)	AgNP in ethanol/a-Si:H
	AgNP in EG/a-Si:H

Figure 5.2 illustrates the transmission (a), specular (b) and diffuse (c) reflection spectra

obtained for the list of substrates given in Table 5.1.

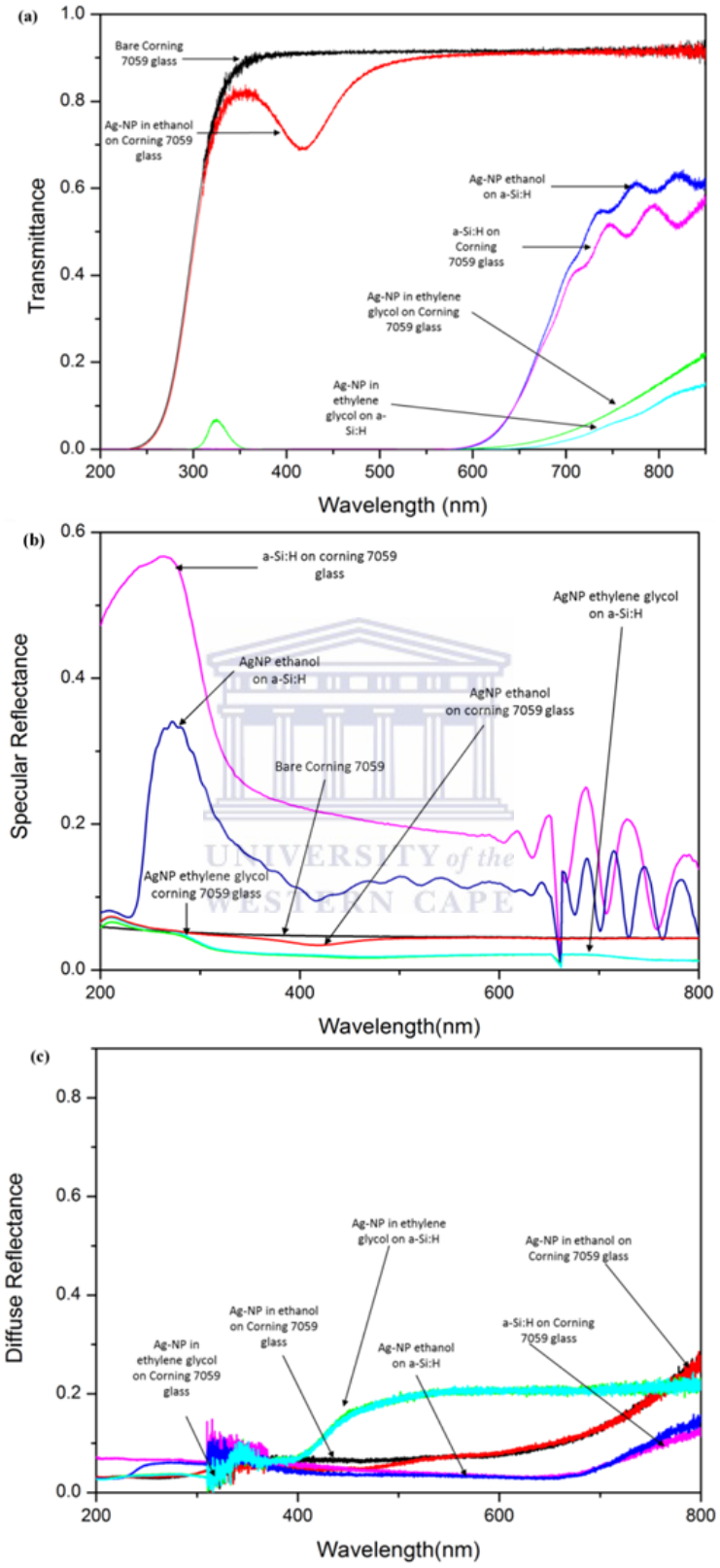

Figure 5.2: Transmission (a), specular (b) and diffuse (c) reflection spectrum showing the effect of Ag-NP on the optical responses of thin films.

From Figure 5.2 it is evident that the incorporation of the silver nanoparticles onto the thin film has a noticeable effect on the transmission, specular and diffuse reflection of the thin films. For the deposition of the silver nanoparticles in ethanol onto the bare Corning glass (AgNP in ethanol/bare Corning) a decrease in the transmission and reflectance is observed between 350 and 500 nm, suggesting that the nanoparticles absorb light in this region (Figure 5.2). This decrease may be attributed to the characteristic plasmon resonance peak at approximately 420 nm, observed in the UV-VIS spectrum of the silver nanoparticle suspension. The reduced reflectance in this range may also be due to the excitation of quadrupolar resonances and high radiative scattering efficiency, which scatters the light into the forward direction [5.6].

For the AgNP in ethylene glycol/Corning glass, an increase in the transmission is observed from 300 to 350 nm. This peak may be attributed to a small area on the corning glass substrate that was not covered by the suspension, hence allowing some photons to be transmitted.The wavelength region from 200 to 250 nm of the silver deposited films (AgNP on corning and a-Si:H thin films) show reduced reflectance, thus behaving as anti-reflective coatings. This behaviour may be attributed to the combined effects of interband transitions in the silver and reduced refractive index mismatch [5.6].

For wavelengths exceeding the plasmon resonance of the silver nanoparticles, an increase in transmission, accompanied by a decreased specular and diffuse reflectance of the incident photons is observed (Ag-NP in ethanol/ a-Si:H). This may be attributed to scattering of the light by the dipolar resonance of the particles, which will preferentially direct the light into the high refractive index a-Si:H rather than into air [5.6]. It may also suggest that high angle scattering (into the substrate) of the silver nanoparticle on the surface of the thin film occurs, since diffuse reflectance spectroscopy may only detect photons reflected at lower angles. The mechanism of this high angle scattering was presented in Figure 2.13 of Section 2.3.1.

An increased transmission of AgNP in ethanol/ a-Si:H was observed due to the presence of the silver nanoparticles. The UV-VIS absorbance spectrum of the silver nanoparticles suspension prepared in ethylene glycol (Figure 4.17) shows a relatively broad red shifted plasmon resonance peak in the range of 300 to 700 nm. This is relatively advantageous for thin film application, since light trapping should occur over a broad wavelength range [5.2].

The size of the silver nanoparticles prepared in ethylene glycol is also larger than those prepared in ethanol. The shapes of these nanoparticles are also significantly different as evident in Figures 4.18 and 4.120, respectively. From equations (2.10) and (2.11) it is therefore evident; that the larger particles produced in ethylene glycol has a greater scattering cross section, as opposed to the silver nanoparticles prepared in ethanol. The presence of the sheet like structures and agglomerates observed in the ethanol suspension may also increase the scattering cross sections. However, since the majority of the silver nanoparticles produced in the ethanol based suspension, were small spherical particles (~ 3 nm) the contribution from the sheet like structures were assumed to be negligible.

Higher modes of excitation occur with an increase in the size of the nanoparticles. The excitation modes determine whether or not the light trapping mechanism will increase or decrease the light trapping efficiency. All modes of excitation possess forward scattering, however alternating modes such as octupolar and dipolar modes possess backward scattering. For larger nanoparticles the forward scattering efficiency is enhanced due to the excitation of the quadruploar resonances [5.6].

For the silver nanoparticles in ethylene glycol, deposited onto both the bare Corning glass as well as the a-Si:H thin film, the transmission and specular reflection decreased significantly. The silver nanoparticles prepared in ethylene glycol are larger in size, hence they possess a greater forward scattering efficiency, and this may be the reason for the decreased specular reflectance. These samples also exhibit greater diffuse (although minimal) reflectance than

any of the other samples; which may be attributed to the enhanced scattering cross section of the particles, attributed to the increased size.

High Resolution Scanning Electron Microscopy will provide insight into the surface coverage of the silver nanoparticles across the surface of the substrate.

5.3 Morphological Properties of thin films

The morphological properties of the thin films were obtained by analysing High Resolution Scanning Electron Microscopy (HRSEM) micrographs of the thin films. The micrographs provide information about how well dispersed the silver nanoparticles are across the substrates. The micrograph of the amorphous silicon thin film with the absence of silver nanoparticles, with the corresponding EDS (Energy Dispersive Spectroscopy) spectrum is exhibited in Figure 5.3 a and b, respectively. The EDS spectrum shows the presence of silicon, which may be attributed to the amorphous silicon thin films and the Corning glass substrate, the presence of the aluminium and barium are attributed to the Corning glass substrate [5.7]

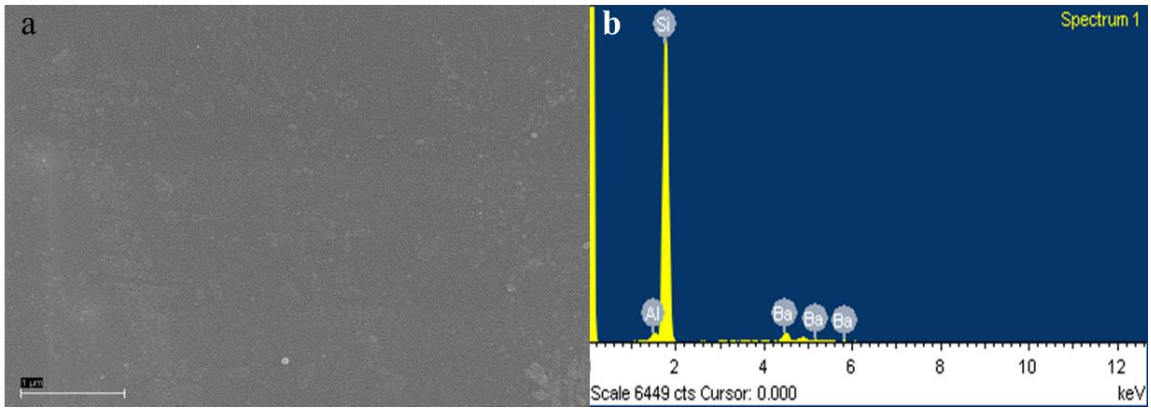

Figure 5.3: (a) HRSEM micrograph and (b) EDS spectra of the amorphous silicon thin film on a glass substrate

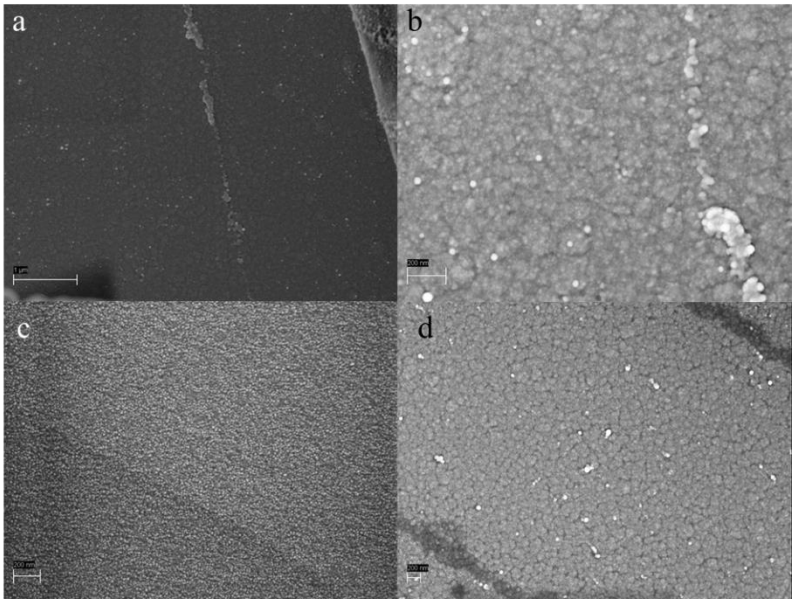

Figure 5.4: HRSEM micrographs of (a and b) silver nanoparticles in ethylene glycol on a-Si thin film, and (e and d) silver nanoparticles in ethanol on a-Si thin film.

Figure 5.4 (a and b) show that the nanoparticles in ethylene glycol on the a:Si-H are separated by distances larger than the size of the silver nanoparticles, whilst the silver nanoparticles prepared in ethanol have relatively small distances between consecutive particles as illustrated in Figure 5.4 (c). The separation between the silver nanoparticles has a significant effect on the way the nanoparticles interact with the incident radiation and the a:Si-H thin film. The EDS spectrum of the silver nanoparticle incorporated thin film is exhibited in Figure 5.5.

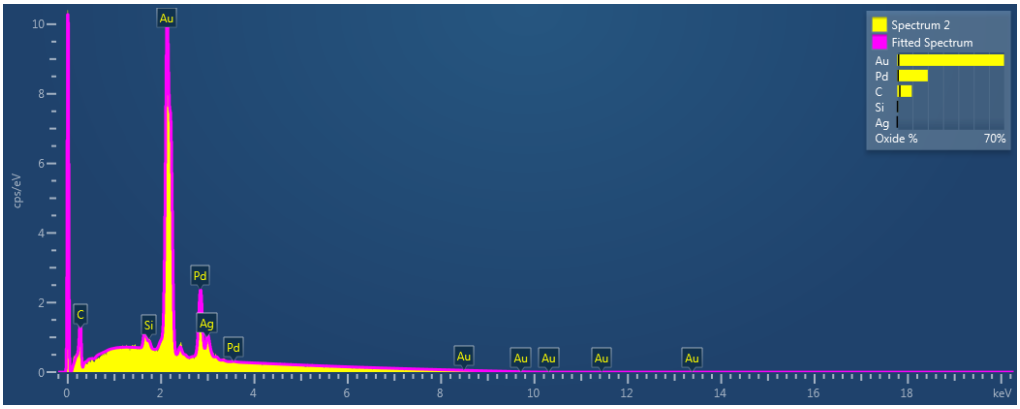

Figure 5.5: EDS spectrum of the silver nanoparticle incorporated thin film.

The EDS spectrum illustrated above (Figure 5.5), confirms the presence of the silver nanoparticles on the amorphous silicon thin films. The gold and the palladium observed in the spectrum may be attributed to the gold/palladium coating used during HRSEM sample preparation, whilst the silicon is attributed to the amorphous silicon thin film. The presence of the carbon may be attributed to the presence of the surfactant on the silver nanoparticles.

If the particles are close to one another, a reduced reflectance may be attributed to the near field interaction of the silver nanoparticles with a:Si-H thin film. When the separation between the particles is smaller than the wavelength of the incident photons, the silver nanoparticles interaction will be dominated by near field effects. Far field effects will take place when the spacing between the silver nanoparticles is larger than the incident photons. Near field effects absorb the incident radiation and couple the light to the high refractive index of the a-Si thin film, whilst far field effects result in the scattering of the radiation [5.6, 5.8].

For the thin films with the silver nanoparticles prepared in ethylene glycol the nanoparticles are spaced further apart than the silver nanoparticles in ethanol. This suggests that the thin films with the silver nanoparticles suspended in ethanol interact via near field scattering. The reduction in specular reflectance of the thin film (Figure 5.2 b) with the suspension prepared in ethanol may be attributed to the interaction of silver nanoparticles' surface plasmon resonances (near-field effects).

The silver nanoparticles suspended in ethylene glycol interacted via far field coupling since the nanoparticles were spaced further apart. This confirms the enhanced diffuse reflection (Figure 5.2 c) observed in the UV-VIS of the thin films.

5.4 Conclusion

Silver nanoparticles were deposited onto bare Corning glass substrates, as well as a:Si-H thin films, deposited by hot wire chemical vapour deposition (HWCVD). The silver nanoparticle suspensions were sprayed onto the substrates resulting in thin films containing silver nanoparticles.

Two types of suspensions were deposited onto the substrates, one prepared in ethylene glycol and the other in ethanol. UV-VIS analysis of the silver nanoparticles deposited on a:Si-H thin films, and bare glass reveal that the silver nanoparticles prepared in ethylene glycol was more suitable for thin film application.

HRSEM analysis of the thin films illustrated that the silver nanoparticles were succesfully deposited onto the substrates, and that it is possilbe for silver nanoparticles suspended in ethanol to interact via near field coupling, whilst the silver nanoparticles in ethylene glycol interacted via far field coupling.

5.5 References

[5.1] Atwater. H, and Polman. A, *Nature Materials*, **9**, p 205 (2010)

[5.2] Catchpole. K, and Polman. A, *Optics Express*, **16**, p 21793 (2008)

[5.3] Pillai. S, and Green. M., *Sol. Energy Mater. Sol. Cells* , **94**, p 1481 (2010)

[5.4] Microscopy Resource Centre, accessed 09 September 2013, [Online] http://www.olympusmicro.com/primer/java/reflection/specular/ accessed 21August 2013

[5.5] Verlaan. V, Verkerk. A, Arnoldbik. W, van der Werf. C, Bakker. R, Houwling. Z, Romijn. I, Borsa. D,Weeber. A, Luxembourg. S, Zeman. M, Dekkers. H and Schropp. R, *Thin Solid Films*, **517**, p 3499 (2009)

[5.6] Thouti. E, Chander. N, Dutta.V, and Komarala. V, *J.Opt.*, **15**, p 1 (2013)

[5.7] Oliphant. C, Muller. T, Adams. A, Msimanga. M, and Arendse. C, "Determination of nitrogen content in silicon nitride thin films fabricated by hot-wire CVD" Presented at: Test and Measurement Conference, Gauteng, South Africa (2013)

[5.8] Spinelli. P, Hebbink. M, Waele. R, Black. L, Lenzmann. F, Polman. A, *Nano Lett*., **11**, p 1760 (2011),

CHAPTER 6

Overall Conclusions and Recommendations

Silver nanoparticle synthesis and characterization

PVP-stabilized silver nanoparticles were successfully prepared using the polyol method, where ethanol acted as both the solvent and the reducing agent.

X-Ray Diffraction (XRD) analysis of the silver nanoparticles illustrated the crystalline nature of the synthesized silver nanoparticles. These results confirmed the characteristic face-centered (*fcc*) structure of the silver nanoparticles.

Thermogravimetric Analysis (TGA) of the silver nanoparticles with PVP showed that the PVP is completely decomposed at 500^0C. The presence of a material with a greater melting point than 600^0 C was also observed, which could be due to the silver nanoparticles.

In addition to the spherical particles, sheet like structures were also obtained and were observed to grow via Ostwald ripening, due to the preferential attachment to the more active (111) planes. This study has shown that PVP may be used as alternative to ammonia to produce the sheet like structures.

Reaction Time and Temperature

UV-VIS and HRTEM analysis of the silver nanoparticles suspensions showed that, although silver nanoparticles can be obtained at room temperature, the reaction times are prolonged.

Raising the temperature from room temperature to reflux temperature (80°C) therefore dramatically reduced the reaction time from 6 days, to a mere 6 hours at reflux temperature.

PVP concentration

The investigation of the concentration of surfactant (PVP) revealed that an optimum ratio of 1:50 (Ag:PVP) is required to produce silver nanoparticles with increased uniformity.

Different solvent/reducing agent

UV-VIS and HRTEM analysis of the silver nanoparticle suspensions prepared in ethylene glycol, as the solvent and reducing agent, also revealed that silver nanoparticles of various morphologies such as triangles, squares, rods and spheres could be produced. Sizes ranging between 30 – 80 nm were observed. This is beneficial for thin film application since larger particles exhibit greater scattering cross sections, and in turn enhance light trapping of the thin films.

Different surfactant

HRTEM results of chitosan-stabilized silver nanoparticles revealed spherical silver nanoparticles and could hence be used as a capping agent/stabilizer for silver nanoparticles. However, the nanoparticles are non-uniformly dispersed. Since this was a preliminary study, further investigations on the pH, concentration and solubility of this surfactant should be conducted. The environmentally benign nature of this surfactant warrants further investigations into the prospects of application in the production of silver nanoparticles by polyol synthesis.

Thin films

The synthesized silver nanoparticles were successfully deposited onto corning glass and amorphous silicon thin films using a spray technique.

Optical Properties

UV-VIS analysis of the films illustrated that the presence of the silver nanoparticles decrease the reflectance of the a-Si thin films, and may therefore be used as a light trapping mechanism in thin film solar cells.

Structural Properties

The presence of the silver nanoparticles particles on the thin films were confirmed by HRSEM and EDS. The HRSEM analysis also revealed that the silver nanoparticles were not evenly dispersed across the thin films/ substrates. Hence optimization of the spray technique is required, since the thickness of the silver nanoparticles cannot be obtained using this technique.

Recommendations

Parameters such as precursor injection, as well as the critical silver nitrate concentration required in order to produce uniform isotropic silver nanoparticles should also be investigated, such that control over the nucleation and growth process of the nanoparticles may be obtained.

Further investigations entail the construction of a complete solar cell, to investigate the effect that the silver nanoparticles have on the efficiency of the solar cell.